MICROSTRUCTURE DESIGN OF LOW ALLOY TRANSFORMATION-INDUCED PLASTICITY ASSISTED STEELS

A Dissertation

by

RUIXIAN ZHU

Submitted to the Office of Graduate Studies of
Texas A&M University
in partial fulfillment of the requirements for the degree of

DOCTOR OF PHILOSOPHY

Approved by:

Chair of Committee,	Ibrahim Karaman
Committee Members,	Raymundo Arroyave
	Ted Hartwig
	Amine Benzerga
Head of Department,	Andreas Polycarpou

May 2013

Major Subject: Mechanical Engineering

ABSTRACT

The microstructure of low alloy Transformation Induced Plasticity (TRIP) assisted steels has been systematically varied through the combination of computational and experimental methodologies in order to enhance the mechanical performance and to fulfill the requirement of the next generation Advanced High Strength Steels (AHSS). The roles of microstructural parameters, such as phase constitutions, phase stability, and volume fractions on the strength-ductility combination have been revealed.

Two model alloy compositions (i.e. Fe-1.5Mn-1.5Si-0.3C, and Fe-3Mn-1Si-0.3C in wt%, nominal composition) were studied. Multiphase microstructures including ferrite, bainite, retained austenite and martensite were obtained through conventional two step heat treatment (i.e. intercritical annealing-IA, and bainitic isothermal transformation-BIT). The effect of phase constitution on the mechanical properties was first characterized experimentally via systematically varying the volume fractions of these phases through computational thermodynamics. It was found that martensite was the main phase to deteriorate ductility, meanwhile the C/V_A ratio (i.e. carbon content over the volume fraction of austenite) could be another indicator for the ductility of the multiphase microstructure.

Following the microstructural characterization of the multiphase alloys, two microstructural design criteria (i.e. maximizing ferrite and austenite, suppressing athermal martensite) were proposed in order to optimize the corresponding mechanical performance. The volume fraction of ferrite was maximized during the IA with the help

of computational thermodyanmics. On the other hand, it turned out theoretically that the martensite suppression could not be avoided on the low Mn contained alloy (i.e. Fe-1.5Mn-1.5Si-0.3C). Nevertheless, the achieved combination of strength (~1300MPa true strength) and ductility (~23% uniform elongation) on the low Mn alloy following the proposed design criteria fulfilled the requirement of the next generation AHSS.

To further optimize the microstructure such that the designed criteria can be fully satisfied, further efforts have been made on two aspects: heat treatment and alloy addition. A multi-step BIT treatment was designed and successfully reduced the martensite content on the Fe-1.5Mn-1.5Si-0.3C alloy. Microstructure analysis showed a significant reduction on the volume fraction of martensite after the multi-step BIT as compared to the single BIT step. It was also found that, a slow cooling rate between the two BIT treatments resulted in a better combination of strength and ductility than rapid cooling or conventional one step BIT. Moreover, the athermal martensite formation can be fully suppressed by increasing the Mn content (Fe-3Mn-1Si-0.3C) and through carefully designed heat treatments. The athermal martensite-free alloy provided consistently better ductility than the martensite containing alloy.

Finally, a microstructure based semi-empirical constitutive model has been developed to predict the monotonic tensile behavior of the multiphase TRIP assisted steels. The stress rule of mixture and isowork assumption for individual phases was presumed. Mecking-Kocks model was utilized to simulate the flow behavior of ferrite, bainitic ferrite and untransformed retained austenite. The kinetics of strain induced martensitic transformation was modeled following the Olson-Cohen method. The

developed model has results in good agreements with the experimental results for both TRIP steels studied with same model parameters.

To my parents and Olivia

ACKNOWLEDGEMENTS

I would like to thank my committee chair, Dr. Karaman, and my committee members, Dr. Arroyave, Dr. Hartwig, and Dr. Benzerga, for their guidance and support throughout the course of this research. I would like to especially thank Dr. Karaman for the unselfish cultivation in the past five years. I also appreciate the guidance from Prof. Chumlyakov in my research. In addition, I would like to thank S.Li for the computational calculations, from which I benefited a lot during the research.

Thanks also go to my friends, particularly H.Qian, H.Zhu, J.Zheng, J.Zhang, P.Gao, M.Song, S.Cheng, Y.Chen, and colleagues, E.Dogan, J.Ma, S.Razavi, C.Atli, N.Ozdemir, J.Monroe, N.Barta, N.Bruno, C.Hayrettin, A.Evirgen, and the department faculty and staff for making my time at Texas A&M University a great experience. I also want to extend my gratitude to the National Science Foundation, which supported my study, and to all the instructors of the courses I attended.

Finally, thanks go to my mother and father for the endless and unselfish encouragement and support. I would not be able to achieve this work without them.

TABLE OF CONTENTS

Page

LIST OF FIGURES

Page

LIST OF TABLES

Page

CHAPTER I

INTRODUCTION

1.1 The Need of the Third Generation Advanced High Strength Steels

The quest for improved efficiency in energy use is motivated by economic driving forces as well as by environmental concerns. Recent congressional mandates for the improvement of the fuel economy of the U.S. vehicle fleet have made this quest even more pressing. One of the most cost-effective approaches is vehicle's weight reduction. Although low density materials such as composites, polymers, aluminum and magnesium alloys are being increasingly used, their high production costs and/or low recyclability limit their widespread usage. Fortunately, near-term and cost-effective solutions can be found through the use of Advanced High Strength Steels (AHSS). Figure 1 shows the estimation of AHSS mass fraction in auto parts by 2020. About 97.4% mass weight will be high strength steels (HSS) or AHSS [1], mainly including dual phase steels (DP), high strength low alloy steels (HSLA), transformation induced plasticity steels (TRIP), twining induced plasticity steels (TWIP) and martensitic steels (MS).

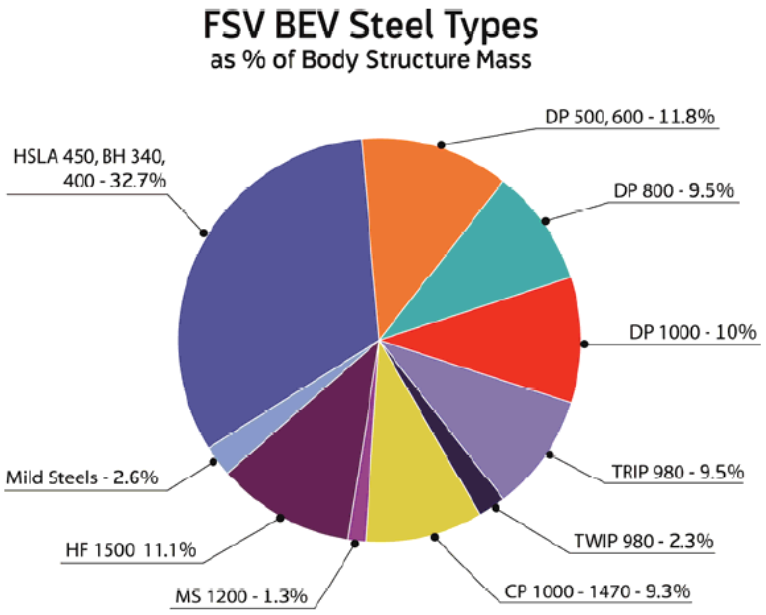

Figure 1. Estimation of mass fraction of steels used in commercial vehicles at the end of 2020 (FSV: future steel vehicle, BEV: battery electric vehicle) [1]

Existing AHSS technologies, however, are insufficient to meet the minimal requirements in terms of strength, formability, and cost. Figure 2 shows the current status of the AHSS development. Although the first generation AHSS exhibited strengths exceeding 1000 MPa in the case of martensitic steels (MS), their formability was not satisfactory, allowing only the most basic forming processes. Much better formability was obtained in the second generation AHSS through the use of a ductile austenitic matrix. However, this was achieved through the addition of substantial amounts of costly alloying elements, such as Ni. There is therefore a need for a new generation AHSS based on plain carbon and low alloy steels having very low production

costs and permitting to further increase the strength and ductility achieved with the first generation AHSS, which is expected to fill in the 'blank' region between the 'banana' shapes in Figure 2.

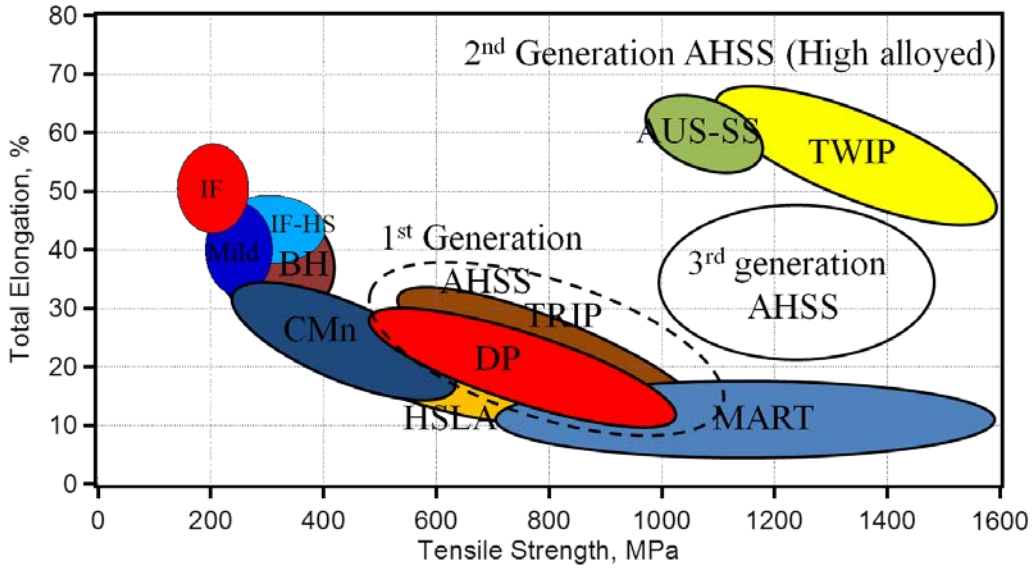

Figure 2. Summary of the strength and ductility of current AHSS and future opportunity of the 3rd generation AHSS [2]

1.2 Low Alloy Transformation Induced Plasticity (TRIP) Assisted Steels

First observed by Zackay *et al.* [3], Transformation Induced Plasticity (TRIP) assisted steels attracted a renewed interest from both industry and academia since the 1980s [4, 5]. The TRIP effect has been observed on austenitic steels (i.e. 304 grade stainless steels) and on low alloy multiphase steels which contain dispersed retained

austenite. The later one is of greater interest due to the combination of good performance and low cost. A common low alloy TRIP-assisted steels usually contains a small amount of Mn and Si (a few percent in wt) and low carbon levels (<0.4C). The microstructure of these steels include 50-55% ferrite, 30-35% bainite, and 7-15% retained austenite in volume. During deformation, they utilize strain-induced martensitic phase transformation as the subsidiary mechanism to enhance strain hardening capability, and thus, ductility, in addition to deformation by dislocation slip. Thanks to the complicated multiphase microstructure, a large freedom of designing strength and ductility exist in the TRIP-assisted steels, such as adjusting stability of retained austenite, changing phase constitution, grain size, texture and so on, which makes them a good candidate for the next generation AHSS.

As mentioned above, martensitic transformation is believed to be the key for the enhanced strain hardening in TRIP-assisted steel. In this scenario, martensite is formed through the stress or strain induced transformation of retained austenite. Throughout the transformation, additional dislocation is generated in the surrounding ferrite matrix which results in the enhanced strain hardening. Compared to the traditional thermal quenching, the energy required for the stress or strain induced martensitic transformation is provided by mechanical loading rather than overcooling. The difference between stress and strain induced martensitic transformation mainly lies in whether additional martensite nucleation site forms due to the plastic strain.

The pioneer works by Olson and Cohen [6-8] systematically discussed the mechanisms and conditions of stress- and strain-induced martensitic transformation. For

stress or strain martensitic transformation, mechanical energy functions as the additional driving force for the transformation subsidiary to the thermal energy. Thus, the M_s temperatures in these cases are raised as compared to the thermally induced transformation. In addition, depending on the deformation temperature, the transformation can be classified as stress- or strain- induced, as presented schematically in Figure 3. For the temperature between M_s and M_s^{σ}, the transformation mode is stress-induced, which occurs before the austenite yielding and follows the classical Clausius-Clapeyron relation as the temperature increases. The mechanical driving force fills the chemical energy gap between austenite and martensite due to the increase in deformation temperature. If the deformation temperature is between M_s^{σ} (the intersection of austenite yield stress and the line of Clausius-Clapeyron relation) and M_d, martensite transformation is strain-induced and it initiates after austenite yields. Above M_d, no stress- or strain- induced martensitic transformation is expected to occur since the mechanical driving force is no longer enough to make up the chemical energy difference between austenite and martensite.

To obtain the TRIP effect, stabilized austenite at the application temperature is a basic requirement. There are two major thermal processing methods to obtain austenite at and near ambient temperature in low alloying TRIP-assisted steels: two-stage heat treatment [9, 10], and quenching & partitioning (Q&P) [11-13]. The general idea of the two methods is to enrich carbon content in the austenite and thus suppress thermally induced martensite. Details of each processing method will be discussed in the following sections.

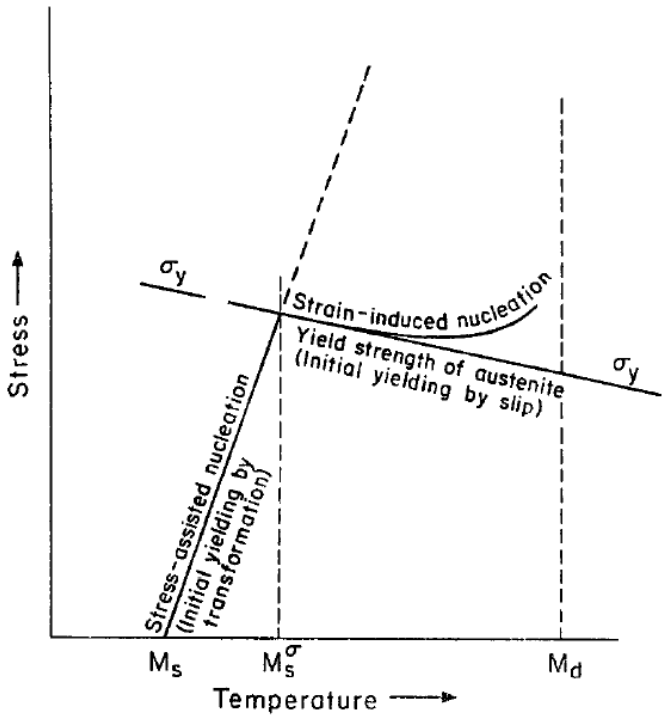

Figure 3. Schematic stress-temperature phase diagram showing the different conditions for stress- and strain-induced martensitic transformation, cited from [6]

1.2.1 Two-stage Heat Treatment

The two-stage heat treatment consists of intercritical annealing (IA) and bainitic isothermal transformation (BIT). A schematic diagram of the conventional two-stage heat treatment can be seen in Figure 4a. The IA is performed to form a ferrite/austenite mixture at temperature between Ac1 and Ac3 [14, 15], which are the temperatures for austenite start and finish in the phase diagram. At the end of IA, the material is rapidly quenched to a warm temperature for BIT. BIT utilizes the bainitic transformation at the warm temperature (usually between 200 and 500°C) and allows austenite to transform

into bainite. Bainite has a composite structure consisting thin layer ferrite (known as bainitic ferrite) and thin film austenite between the bainitic ferrite plates. Accompanied with the bainitic transformation, the carbon in bainite, is ejected to the surrounding untransformed bulky austenite or the thin film austenite layers of the bainite. With some cementite suppressing additions such as Si or Al in the alloy, the carbon-rich austenite can be prevented from the decomposition and stabilizes at ambient temperature after the heat treatment. As a result, a multiphase microstructure including ferrite, bainite, retained austenite and possibly some martensite is usually obtained after the two-stage heat treatment. The volume fraction of retained austenite can reach up to about 20% using this method. A good combination of strength and ductility can be obtained with the resulting multiphase microstructure, as some of the alloying systems have been commercialized such as TRIP450/800 and TRIP590/780.

Since the two-stage heat treatment is known to be capable of retaining austenite effectively, effort has been made to modify the two-stage heat treatment in the past two decades, in order to further improve the stability of retained austenite and the mechanical properties [5, 16, 17]. One example is to replace the rapid quenching from IA to BIT by a combination of slow cooling (e.g. 4-10°C/s) after IA to around Ac1 (the minimum temperature of forming austenite in the phase diagram) and a rapid quenching (e.g. in the order of 50°C/s~100°C) to BIT temperature (Figure 4b). During the slow cooling, some austenite is transformed to low carbon containing ferrite. Thus the carbon content in the remained austenite after IA is further enriched and stabilized. Such method has been

reported to result in better enhanced mechanical properties with monotonic tensile tests [5].

Another example of the heat treatment modification is so called the cyclic austempering [18, 19], which is applied at low BIT temperatures (e.g. 200°C-300°C). Instead of an isothermal heat treatment, the heat treatment temperature of BIT is cycled between B_s (bainitic transformation starting temperature, i.e. the maximum temperature at which bainitic transformation can occur) and M_s, as shown in Figure 4c. The motivation for such processing is to accelerate the bainitic transformation at low temperatures, which otherwise would take up to several weeks to finish the bainitic transformation. It is reported that the kinetics of bainitic transformation can be accelerated by up to 80% by this method than conventional BIT [18].

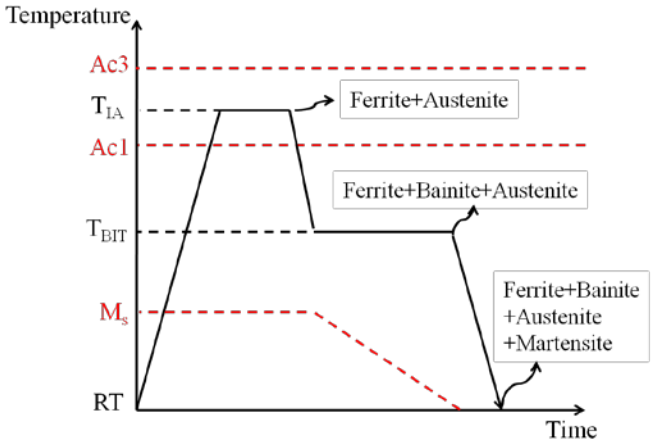

(a)

Figure 4. Schematics showing the thermal processing route for the conventional two-stage heat treatment (a), two-stage heat treatment with modified IA (b), and cyclic austempering to accelerate bainitic transformation (c). Ac1 and Ac3: Austenite start forming temperature and fully austenitic temperature, Bs: Bainite start forming temperature, Ms: Martensite start forming temperature, RT: Room temperature

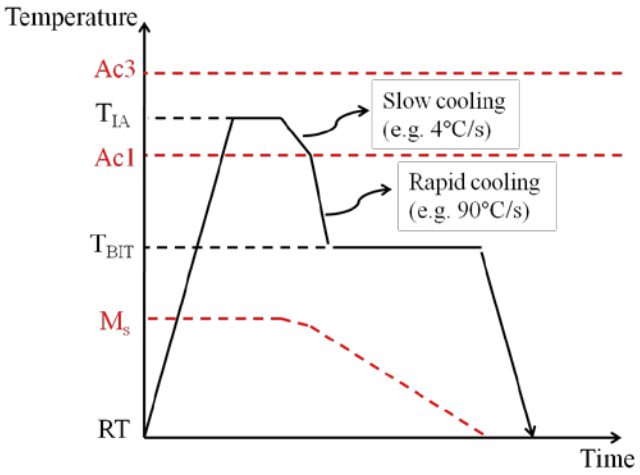

(b)

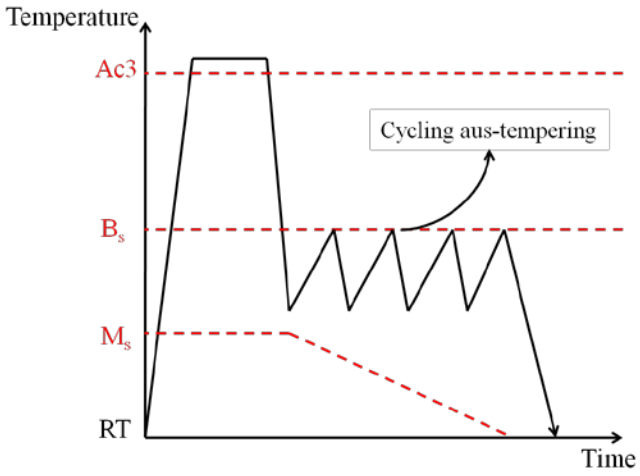

(c)

Figure 4. Continued

1.2.2 Quenching and Partitioning (Q&P)

The Q&P method was proposed more recently. A schematic processing route can be seen in Figure 5. This method consists of a quenching stage (i.e. to a temperature between the martensite start and finish temperatures) from solution heat treatment temperature above Ac3, an isothermal heat treating stage at either the same or a higher temperature (‘Partitioning’) than the quenching temperature, and eventually a cooling stage down to room temperature. By the first quenching stage, an austenite-based microstructure can be obtained with martensite as the second phase. During the ‘partitioning’ stage, the carbon in quenched martensite tends to transfer to the untransformed austenite and improves its stability. After the Q&P treatment, the resulting microstructure usually contains martensite with very low carbon content and certain amount of retained austenite.

The Q&P method has both advantages and disadvantages as compared with the two-stage heat treatment. First, the processing period is much shorter with Q&P (e.g. in tens of seconds) than the two-stage heat treatment (e.g. several minutes to hours). Second, the matrix is much stronger due to the presence of martensite. Moreover, the Q&P method can also be modified further, similar to the two-stage heat treatment. Several modifications on the Q&P method have been proposed in the literature. One is so called quenching-partitioning-tempering (QPT) process [20-22], which includes an additional tempering stage after the conventional Q&P. The purpose of the additional tempering stage is to form some nano size (a few nano meters [20]) precipitates (e.g. NbC, TiC) to strengthen the matrix. However, there are also drawbacks for Q&P. Less

amount of retained austenite (less than 15%) usually forms after Q&P, which is one of the drawbacks for low alloy TRIP-assisted steels. For QPT, the volume fraction of retained austenite for low carbon steels is even less and barely detectable due to the formation of carbides. Small amount of retained austenite leads to less strain hardening from martensitic transformation, and drives the mechanical properties (i.e. strength and ductility) closer to those of the martensitic steels. In order to increase the volume fraction of retained austenite, the carbon content has to increase in the alloy, which would, however, result in poor weldability.

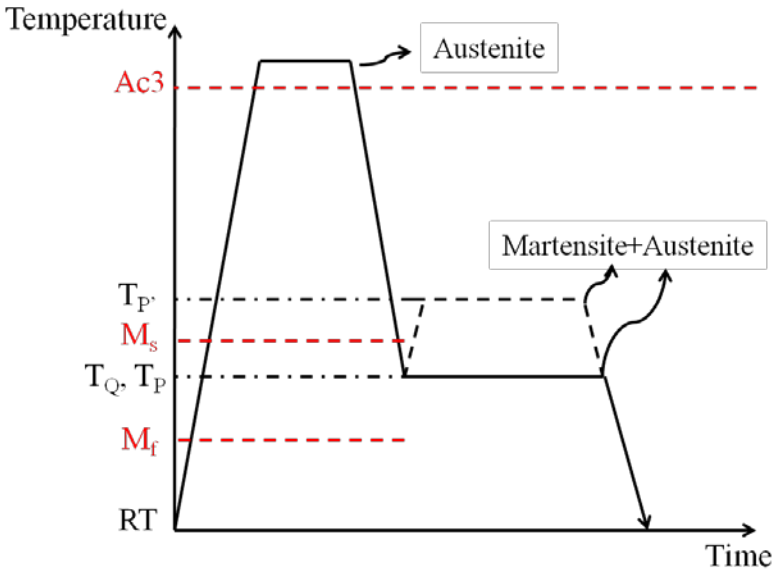

Figure 5. Schematic of the thermal processing route for the Q&P process. T_Q is the quenching temperature which is selected between M_s and M_f. After quenching, the partitioning stage can be performed either at the same temperature, T_p, or a higher temperature T_p' (following the dashed route). Ac3: fully austenitic temperature, M_s and M_f: Martensite start and finishing temperature

1.3 Austenite Stability

Since austenite is the source of stress/strain induced martensitic transformation, and thus the extra hardening source for TRIP-assisted steels, it is of great interest and importance to understand how to control the stability of retained austenite. Thus, many studies [16, 23-28] have been focused on the austenite stability. It is found that the austenite stability can usually be controlled by three factors: chemical composition, grain size, and mechanical stabilization [29].

1.3.1 The Effect of Chemical Composition

The chemical composition is regarded to be the most critical factor for the stability of retained austenite. For low-alloy steels, carbon is the main element to determine the martensite transformation temperature (M_s) of the retained austenite. Many empirical relations have been proposed using the results from the enormous kind of steels to predict the M_s temperature of austenite as a function of various elements such as C, Mn, Al [30-32]. After the characterization of 184 different kinds of steels, the Andrew's [30] empirical relation indicates that the addition of 1% (in wt%) carbon content could result in 423°C reduction in M_s temperature. Van Dijk *et al* [28] utilized in situ synchrotron X-ray diffraction to monitor the volume fraction of retained austenite for several low alloy TRIP-assisted steels (C-Mn-Si-Al-P) during cooling from 300K to 100K. It was found that no martensitic transformation occurs even at 100K if the austenite is sufficiently enriched in carbon through BIT. In addition to carbon, many

reports have also addressed on the effect of micro-alloying (i.e. Al, Nb, Ti, Ni, Cu, Mo) on the stability of austenite in recent years [33-40]. While theoretically most alloying elements are beneficial to reduce M_s temperature (except Al, Co), the addition of some elements (i.e. Nb, Ti, Mo) could easily result in carbide formation (NbC, TiC, MoC) during thermal processing, which consumes the carbon content in the matrix and increase M_s eventually.

1.3.2 The Effect of Grain Size

It is known that the retained austenite exists in two morphologies in TRIP-assisted steels: thin-film within bainite or blocky island. The thin-film retained austenite has been reported not to transform regardless of temperature variation or deformation [41]. Thus, most reports discussing the effect of grain size on the stability of retained austenite refer to the blocky austenite. Figure 6 shows a theoretical prediction by Wang *et al* [24] of the M_s temperature as a function of the grain size of austenite with two carbon contents (in the same material: 0.15C-1.5Mn-1.5Si-Fe), considering the extra interfacial energy due to the formation of martenstie. According to the predictions, carbon content only shifts the curve vertically. For both carbon contents, the M_s temperature rapidly decreases when the grain size is below 0.1μm. On the other hand, it saturates and does not change for grain sizes higher than 1μm. The reason for the decrease in M_s (better austenite stability) with small grain sizes was attributed to the insufficient nuclei density [24]. It was further suggested that the grain size of retained

austenite should be controlled in the range of 0.1 to 1μm. Too small grain sizes will result in untransformable retained austenite while large grain sizes are equally useless since it transforms too early and could not provide extra hardening. As far as experiments are concerned, Jimenez *et al* [42] characterized the stability of individual austenite grain of a low alloy TRIP-assisted steel through in-situ 3-D X-ray diffraction microscopy with synchrotron source. By mapping the individual grains with three parameters (M_s, 'Grain volume', and carbon content), it was found that the large 'grain volume' transforms at higher M_s, in order words, less stable than the small ones.

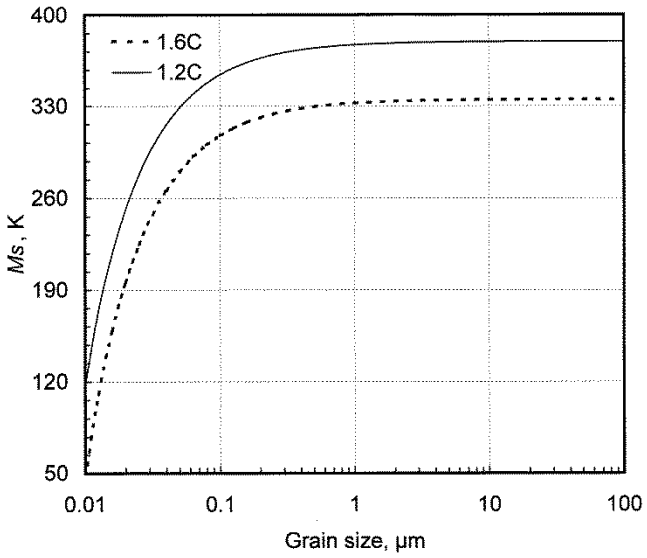

Figure 6. Theoretical prediction of the grain size effect on the M_s temperature for a low alloy TRIP-assisted steel. Solid and dashed lines correspond to two carbon concentrations [24]

1.3.3 Mechanical Stabilization

It is known that, for steels, it is impossible to reach fully martensitic structure through overcooling according to the well recognized Koistinen-Marburger equation [43]. Analogously, it has been widely observed that the retained austenite cannot be fully transformed through the stress- or strain-induced martensitic transformation in TRIP-assisted steels [25, 26, 44-46]. This is known as the mechanical stabilization of austenite. The mechanical stabilization is mostly related to the defect activity, particularly the dislocation density and transformation interface (between martensite and retained austenite) mobility. While the dislocation density in austenite increases with plastic deformation, the mobility of the interface between martensite and retained austenite decreases, and eventually leading to the complete suppression of transformation when the driving force is not enough to move the interface any longer.

Several factors have been reported to effect the mechanical stabilization of austenite in TRIP steels. Chemical composition is one of those, since the chemical driving force for martensitic transformation can be adjusted by alloying elements, such as C, Mn and Al [47]. Morphology (shape) of retained austenite is another factor. It has been reported that the thin film retained austenite (in bainite) is mechanically more stable than the blocky retained austenite due to the higher carbon content [48]. According to Garcia-Mateo's work [49] on bainitic steels containing retained austenite, the morphology (shape) of retained austenite is not as effective as the carbon content in terms of mechanical stabilization. In addition, dislocation density of retained austenite is also a possible factor of mechanical stabilization because it can affect the mobility of

martensite/austenite interface. Recently, Caballero *et al* [25] argued that none of the aforementioned factors is the main reason for mechanical stabilization after experimentally studying several different austenite containing bainitic steels. They suspected that the strength of the ferrite matrix (e.g. bainitic ferrite or ferrite), which can be evaluated from the grain size, volume fraction and dislocation density, might be a more important factor for the strain induced martensitic transformation.

Due to the mechanical stabilization of the austenite, the extra strain hardening due to the TRIP effect is limited at certain plastic deformation level. Chatterjee *et al* [26] calculated the critical plastic strain of reaching mechanical stabilization for various grade of stainless steels and bainitic steels using force balance between transformation interface and dislocation debris in retained austenite. It was found that the critical strain for mechanical stabilization decreases with deformation temperature due to the reduction of ΔG (driving force) between austenite and martensite. Yi *et al* [50] performed computational and experimental work on a customized TRIP-assisted steel (Fe–0.41C–0.26Si–1.53Mn–2.3Al–0.49Cu wt%). It turned out that mechanical stabilization could be triggered in the early stage of plastic deformation (around 15% plastic strain while the total elongation is about 38%). It was further indicated that the enhanced hardening due to the strain-induced martensite transformation occurred only in the early stage of plastic deformation while the further ductility came from the deformation of austenite which was ‘compatible’ with the overall microstructure [50].

1.4 Microstructural Design of TRIP Assisted Steels

The ultimate goal of the microstructure design is to improve both strength and ductility of the TRIP-assisted steels such that they can be eligible for the next generation AHSS. The requirement of such high strength and high ductility comes from the demand on the reduction of CO_2 emission. Recently, the tensile strength of TRIP-assisted steels used in the automobile industry has been in the range of 700 MPa to 900MPa, with an elongation at failure between 15% and 35%.

To further improve the mechanical response, studies on microstructure design of TRIP-assisted steel have been performed through both computational and experimental methodology [17, 51-56]. The design optimizations were performed experimentally in various areas such as phase constitution [5], austenite stability [57], grain size [24, 42], texture [58-60], phase morphology [61] and precipitation [17, 62]. Among these areas, the design of the phase constitution has been focused on adjusting the volume fraction of retained austenite through the heat treatments to reveal their effect on the mechanical response, such as in [5]. However, due to the complexity of the multiphase microstructure and the lack of computational tools in early time, the function of individual phase in the multiphase microstructure has not gained sufficient understanding. Some fundamental questions still remain, such as, what phase constitution is best for achieving highest strength or ducility.

As described in last section, the austenite stability has been found to be controlled by alloying additions, grain size of austenite and mechanical stabilization. Effort has been made to optimize the austenite stability in those aspects. After

characterizing two low alloy TRIP-assisted steel, Haidemenopoulos *et al* [63] revealed that lower BIT temperature (e.g. 400°C v.s.500°C) lead to better austenite stability due to the higher carbon content in the austenite and resulted in higher uniform strain. Interestingly, they also found coincidently that maximum volume fraction of retained austenite corresponded to the highest total elongation, which brought a question: whether the volume fraction or the stability of retained austenite was more critical to the uniform strain.

Computational aspect of the previous microstructural design studies has mainly focused on the bainitic transformation [5, 64]. As the nature of bainite and the bainitic transformation has been gradually elucidated [9, 65, 66] since the 1980s, several thermodynamic and kinetic models were proposed for the bainitic transformation [9]. In thermodynamics-based models [67, 68], the austenite-to-bainite transformation was assumed to progress as long as the maximum chemical driving force for the transformation was larger than the critical energy barriers to the transformation, namely the elastic stored energy and the nucleation energy. Caballero *et al.* [69] demonstrated that the thermodynamics-based approaches were able to predict bainite and martensite start temperatures more accurately as compared to some other empirical formulas [30, 70-73]. Through computational thermodynamics calculations, the phase fractions of the multiphase steels could also be roughly predicted, if the chemical composition and heat treatment conditions are known [74-76]. De Meyer *et al.* [74] have proposed an empirical method for evaluating the kinetics of IA and BIT through dilatometry and were able to predict the phase combination of CMnSi and CMnAlSi TRIP-assisted steels after two-stage heat treatment using ThermoCalc® software.

The microstructure optimization has resulted in good improvement in the mechanical response of TRIP-assisted steels in recent years. Lee *et al.* [51] achieved a tensile strength between 1000 MPa and 1350 MPa, with a total elongation at failure from 7% to 20% on cold rolled TRIP-assisted steels containing 6% Mn. Asoo *et al.* [77] reported 1326 MPa tensile strength with 23% elongation on hot rolled and cold rolled CMnSiNiNb TRIP-assisted steels with ultrafine grain size (0.4 μm). In these works, one way to achieve better strength and ductility has been to increase the weight fraction of alloying elements, e.g. Mn [51, 55], or introduce fine precipitates, e.g. NbC [17, 62], to increase the strength of ferrite, which can all be prohibitive due to cost increases.

1.5 Equal Channel Angular Processing (ECAP)

As mentioned in previous sections, the grain size of retained austenite can significantly affect the stability of retained austenite and thus the mechanical response. Intuitively and based on the other steels (e.g. IF steels), the grain size of ferrite should also increase the strength of the multiphase microstructure of TRIP-assisted steels. So far, the grain sizes of the multiphase TRIP-assisted steels have been controlled through either heat treatment or mechanical processing. The grain size (lath thickness) of bainitic ferrite and thin film retained austenite can be effectively adjusted by tuning the temperature of BIT treatment [9]. Unfortunately, for ferrite and blocky retained austenite, the grain size could not be effectively adjusted without changing the alloying addition. On the other hand, the mechanical processing has an advantage of reducing the

grain sizes of all phases effectively. To date, the mechanical processing on the TRIP-assisted steel has been limited in mainly rolling techniques. (i.e. hot rolling, warm rolling, cold rolling)

Equal Channel Angular Processing (ECAP) is one of the severe plastic deformation (SPD) techniques invented late in the last century. Figure 7 is a schematics illustrating a typical ECAP tool [78]. During processing, the sample billet is first forced into the vertical channel by the plunger. As the sample yields and initiates plastic deformation, the material experiences a severe plastic deformation and flows into the horizontal channel, and eventually ejected from the tool. The amount of plastic strain by each pass is mainly determined by the angle between the two ECAP channels, which is of equal cross sections with the intersecting angle of usually 90° or 120°C [78].

The rationale behind the selection of ECAP as the main processing technique in the present work is several fold. First, the possibility of repeated extrusions without changing cross-section allows more effective grain refinement in bulk materials than any other known technique. Secondly, the conservation of cross section make it possible to apply different rotation sequences after each ECAP pass leading to so-called ECAP routes. Such robustness enables a better microstructural control including the development of crystallographic texture and grain morphology [78-85]. Thirdly, it was shown that different ECAP routes can be able to randomize, convert and/or strengthen crystallographic texture [79]. It can also control, in a limited basis, the size and the distribution of phases or dispersions [85-92].

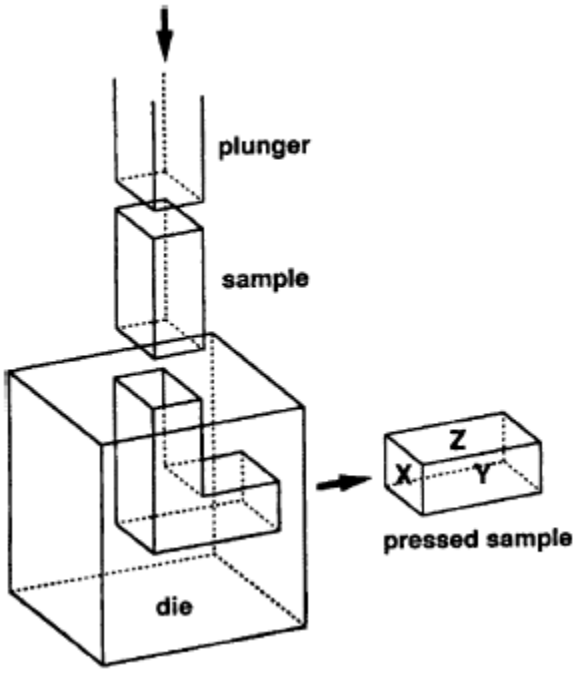

Figure 7. A schematic illustrating a typical ECAP tool, cited from [78]

1.5.1 Ultrafine Grained Steels via ECAP

ECAP has been utilized for the grain refinement and strengthening in many types of steels such as stainless steels, interstitial-free (IF) steels, dual phase (DP) steels and low carbon steels [93-103]. For bulk IF steels, ECAP has been shown to uniformly refine the grain size down to 200-300 nm level. Significant strengthening of the ferrite phase is possible using severe simple shear processing of bulk or plate forms, increasing the UTS from 300 to 800 MPa [93, 103-106]. Due to the grain refinement, drastic reduction of ductility is usually found after ECAP. This drawback, fortunately, can, to some extent, be eliminated by additional annealing after SPD [107, 108]. For IF steels, it

has been shown that annealing after ECAP near the recrystallization temperature can result in a bimodal distribution of grain size and recovers the ductility close to the level before ECAP without a considerable loss of strength as compared to the ECAPed condition [96].

For stainless steels, refinement of austenite is expected to increase strength and affect the evolution of stress/strain-induced martensitic transformation (and thus austenite stability and strain hardening). Yapici *et al* [109] suggested that austenite can be refined through the same ECAP process more readily than ferrite over a wider temperature range offering an important processing flexibility. The structure-property relations in the ECAP processed samples have been systematically studied on low alloy, low carbon ferritic-pearlitic steels [99, 100, 110] and DP steel [111]. For bainitic steels, only a few reports discussed the effect of ECAP on the austenite stability [23]. Even less reports have presented the ECAP on multiphase TRIP steels. Only one report so far, to the best of the author's knowledge, has addressed on the effect of ECAP on a high Si-contained TRIP-assisted steels (Fe-0.22C-2Si-3Mn in wt%) [23]. In this report, the mechanical stabilization of retained austenite after ECAP was evaluated through thermodynamic calculation and characterized experimentally. It was claimed that the retained austenite did not transform until the second pass of ECAP (equivalent strain: ~2) at room temperature. Unfortunately, no quantitative microstructure analysis or mechanical characterization was reported.

1.6 Modeling the Mechanical Response of Low Alloy TRIP Assisted Steels

The modeling of the mechanical flow response of TRIP-assisted steels in the presence of multiphase has attracted strong interest in the past few decades. Compared with other kinds of steels (e.g. martensitic or ferritic steels), the complexity of modeling low alloy TRIP steels lies in two major aspects: multiphase and phase transformation. Since the enhanced mechanical behavior of TRIP-assisted steels is a result of soft ferrite and transformable retained austenite, the microstructure of TRIP-assisted steels should at least contain two phases (i.e. ferrite and retained austenite). Moreover, in order to stabilize retained austenite, one way is to enrich the carbon content in austenite through bainitic transformation. Thus, bainite becomes another essential phase in the microstructure. The stress and strain partitioning among the three phases in the microstructure during deformation is very challenging for modeling. In addition, the stress-/strain-induced martensitic transformation is another feature of the TRIP-assisted steels that needs to be taken into account during modeling. Due to the multiphase structure and complicated stress states, the accurate prediction of the onset and evolution of the martensitic transformation is major challenge for the modeling of TRIP-assisted steels.

In recent years, majority of work on modeling the stress-strain behavior of TRIP-assisted steels has been performed under the framework of crystal plasticity using both numerical and analytical methods [45, 112-118]. Roters *et al* [119] has reviewed the constitutive laws, kinetics, homogenization and multiscale methods in modeling the mechanical behavior of steels (including TRIP steels) under the framework of crystal

plasticity using finite-element method. Choi *et al* [120] developed the representative volume element (RVE) based on experimentally determined microstructures of the commercial TRIP800 steel and obtained good agreement between the simulation results of tensile response using finite element analysis and the experiments. In their work, the mechanical response of each phase in the microstructure was assumed to follow elastic-plastic isotropic behavior during deformation. The Holloman-Ludwig type hardening was assumed for each phase.

Similarly, many analytical models for the flow behavior of TRIP steels have been reported accompanying with validation experiments. To simulate the austenite deformation, Olson-Cohen modeled the kinetics of stress/strain-induced martensitic transformation as a function of plastic strain [7]. The constants in the model were a function of deformation temperature. The model showed good agreement with the experimental results in 304 grade stainless steels at various temperatures. Such Olson-Cohen model, since reported, has been the main method to model the TRIP effect till now. Stringfellow *et al* [121] further included the effect of stress state on the martensitic transformation in the Olson-Cohen model. Samek *et al* [122] discussed the influence of composition on the stability of retained austenite and included the effect (i.e. Al, Mn, Si, C) in the Olson-Cohen model. For non-transforming phases, a number of models have been proposed based on Holloman-ludwig method [112, 120, 123, 124]. Besides that, some physical-based semi-empirical models were also proposed [113, 117, 118]. One well-accepted model was developed by Mecking and Kocks [125, 126]. They provided a unified phenomenological description of work hardening in metals. Dislocation density

was regarded as the only parameter which determined the hardening behavior assuming the deformation temperature and strain rate were constant during deformation.

One typical example of modeling the tensile behavior of multiphase TRIP-assisted steels considering both transforming retained austenite and untransformable phases (e.g. ferrite, bainite) is by Bouquerel *et al* [118]. The model is microstructure-based in which some experimental results were taken as the inputs (e.g. grain size, compositions). First, ferrite, bainite, and retained austenite are modeled individually. Mecking-Kocks model is applied for plastic deformation for all the phases and Olson-Cohen model is utilized for simulating the evolution of martensitic transformation. The fitting parameters in the model are obtained from the experimental results. Microstructures with fully ferrite or bainite are prepared through selected heat treatments in the same composition material as in the multiphase microstructure samples. The fitting parameters for retained austenite are obtained by simulating the 304 and 301LN stainless steels. After the modeling of individual phases, the macroscopic behavior of the multiphase microstructure is obtained by stress rule of mixtures between the individual phases. Retained austenite is first mixed with the strain induced martensite. The two-phase mixture is further mixed with bainitic ferrite and eventually mixed with polygonal ferrite. The results of the mixture show good agreement with the experimental results on two low alloy TRIP-assisted steels. However, various fitting parameters have to be selected for each simulation, which impaired the predictive capability of the model. Moreover, the strain/stress partitioning is not clearly clarified during the development of

the model, which brought difficulty to duplicate and apply on other microstructures with more phases (e.g. thermally induced martensite).

CHAPTER II

MOTIVATION AND OBJECTIVES

The ultimate goal of the current study is to develop the cost-effective 3rd generation AHSS. More specifically, the main task is to optimize the microstructure of TRIP-assisted steels with maximum of 4% alloying addition through the careful selection of thermo-mechanical processing techniques and parameters.

To achieve high mechanical performance, one feasible way is to optimize the phase constitution of the multiphase microstructure in TRIP-assisted steels, since some phases in the microstructure are usually ductile (i.e. ferrite, austenite), while some are very strong (i.e. martensite) but brittle. Also, with the help of computational thermodynamic tools, it is much easier to adjust the phase constitution than to control other microstructural factors such as grain size or texture. Although many efforts have been devoted to the structure-property relations in TRIP assisted steels with various chemical compositions [17, 35, 36, 52, 62, 127], no definitive conclusion has been drawn on what the optimized fractions for each phase should be for a desired combination of strength and ductility. Kuziak et al. [128] reported that the optimum phase content for common low-alloy TRIP-assisted steels contains 50–55% ferrite, 30–35% bainite and 7–15% retained austenite, by volume. Kliber et al. reported that 60% ferrite, 5–20% retained austenite and the balance being bainite [129] is used in the Japanese auto industry to obtain high-strength and high-ductility steels. Unfortunately, none of these studies have rationalized why these fractions were chosen.

In addition, retained austenite and its stability have received notable attention so far in the literature due to its ability of enhance work hardening capability of steels through stress-/strain-induced martensitic transformation. The stability of austenite is related with mechanical properties such as hardening behavior and ductility in previous reports [5, 25, 45, 55, 63, 64]. Retained austenite with good stability could result in better ductility or higher toughness due to the TRIP effect. Similarly, a large volume fraction of retained austenite is believed to be beneficial to the ductility of TRIP-assisted steels or bainitic steels [49, 63]. While these arguments seem to be supported by experimental observations or computations, there has been limited effort on understanding and quantifying the combined effects of austenite stability and volume fraction on the mechanical properties of TRIP-assisted steels for a given chemical composition. More specifically, it is hard to answer the following question: how much austenite with what level of stability is optimum for TRIP-assisted steels in terms of properties such as ductility or toughness? Since the two factors, austenite stability and volume fraction, are not independent from each other due to the conventional thermal-processing routes (i.e. two-stage heat treatment) for achieving TRIP effect (e.g. high carbon content in austenite results in good stability but small volume fraction), it is necessary to perform an in-depth study on the combined effect of these two factors on the mechanical properties of TRIP assisted steels.

At the same time, ferrite usually constitutes the major part (around 50%) of typical TRIP-steel microstructures. Ferrite is a soft phase with good formability and responsible for good ductility in interstitial-free steels (IF steels) and dual phase (DP)

steels [130]. To the best of the authors' knowledge, however, only few reports have particularly addressed the effect of ferrite on the ductility of the multiphase TRIP-assisted steels [5, 45, 53]. Jacques *et al.* [53] demonstrated the strain partitioning in different phases under tension by neutron diffraction and indicated that ferrite deforms more severely than other phases. In other words, ferrite also functions as a 'soft phase' in TRIP assisted steels. Realizing that both retained austenite and ferrite could be beneficial to the ductility, a further question lies in whether the change of ferrite or austenite volume fractions is more influential for the improvement of the ductility in TRIP-assisted steels. In addition, the role of martensite volume fraction on the ductility in the presence of ferrite, bainite, and retained austenite is not very much discussed although it might be in small volume fractions. Thus, a clear understanding on these issues would be beneficial to the optimization of the phase constitution in TRIP-assisted steels for practical applications.

Considering the aforementioned facts, the work of current dissertation begins from the characterization of phase constitution effect on the mechanical behavior of the multiphase low alloy TRIP-assisted steels. With a deeper understanding of that, microstructure optimization criteria will then be proposed. Both experimental and computational methodology will be utilized to achieve the microstructures which fulfill these criteria. For alloys on which the criteria cannot be easily satisfied, efforts will be made to modify the existing heat treatment methods or to change the alloying addition. Finally, a microstructure-based model will be developed to computationally linking the

microstructure and mechanical behavior of the multiphase low alloy TRIP-assisted steels.

The contribution of the present work to the field of TRIP-assisted steel research is several fold. First, the deeper understanding of the function of individual phase in the multiphase microstructure is very beneficial for the understanding of structure-properties relation for the material, which in terms can be utilized for microstructural optimization meeting various requirements (i.e. maximum strength or maximum ductility). Second, the modeling of flow behavior will provide a useful tool to easily map the structure-property relations without complicated experiments. Third, the modification of existing heat treatment method strengthens the link between thermal processing and microstructure: a more variety of microstructure could be obtained without changing the compositions. Last but not least, all the aforementioned aspects are paving the way for further computational optimization (i.e. the integration of thermal processing-microstructure-mechanical property) on TRIP-assisted steels. Ultimately, the thermal processing method (e.g. route, parameters) for a given alloy are expected to be easily determined according to the requirement of mechanical performance in the future.

CHAPTER III

EXPERIMENTAL METHODOLOGY

3.1 Material Selection

Billets of the model TRIP-assisted steels with nominal compositions of Fe-1.5Mn-1.5Si-0.3C (in wt%) and Fe-3Mn-1Si-0.3C (in wt%) were cast with dimensions of 25.4 mm x 25.4 mm x 177.8 mm. Inductively coupled plasma atomic emission spectroscopy (ICP-AES) or spectrographic analysis were conducted on the as-cast materials to determine the actual composition. The actual compositions were listed in Table 1. Only two alloying additions (Mn and Si) other than C were selected in order to reduce the complexity of microstructure, note that a very slight amount of other elements such as S or P may also exist in the material due to the casting. The selection of Si is to suppress cementite formation [5, 131] while the function of Mn is to stabilize retained austenite and as a solid solution strengthener.

Table 1. The actual chemical compositions of the casted material used in present study determined by ICP-AES or spectrographic analysis (only main elements are listed)

	Actual composition in wt%			
Nominal Composition	C	Mn	Si	Fe
Fe-1.5Mn-1.5Si-0.3C	0.32	1.42	1.56	Balance
Fe-3Mn-1Si-0.3C	0.32	2.65	0.95	Balance

3.2 Thermo-Mechanical Treatments

The as-cast billets were first heated up to 950 °C for 1hr to austenitize the microstructure, then quickly ECAP processed at a rate of 25.4 mm/s non-isothermally while the billets were at 950 °C and the ECAP die was at 300 °C. After ECAP, the billets were air cooled to room temperature. The fast extrusion rate was selected to maintain the temperature of the billets as close to 950 °C as possible such that no phase transformation occurred during extrusion. Two passes or four passes were conducted using route C (180° rotation between the passes along the longitudinal axis of the billet), and E (90°C rotation between the first and second pass, 180°C rotation between the second and third pass, and 90°C rotation between the third and fourth pass) with the same extrusion conditions. Dog-bone shaped samples with gauge dimension of 8 mm x 3 mm x 1 mm were cut from the ECAP-processed billets using wire-EDM, with the long axis parallel to the longitudinal axis of the billet and the surface along the normal direction of the billet after ECAP. Samples were sealed in quartz tube with partial pressure of Argon, and heat treated using the two-stage heat treatment (IA+BIT) to obtain a multiphase microstructure including ferrite, bainite, retained austenite and martensite. The details of the heat treatment parameters will be further discussed in the following chapters.

3.3 Microstructural Characterization

The microstructures of the heat treated samples were characterized using Scanning Electron Microscopy (SEM), X-ray Diffraction (XRD), Superconducting Quantum Interference Device (SQUID) magnetometer, and Electron Microprobe equipped with energy dispersive spectrometers (EDS) and wave dispersive spectrometers (WDS). SEM samples were mechanically polished and etched using 2% Nital before examine. XRD samples were chemically polished in a solution of 14ml of 40% HF, 100ml of 30% H_2O_2, and 100ml distilled water before experiments. A Bruker-AXS D8 XRD with Cu K_α radiation (wavelength λ = 0.15406 nm) was utilized in the present study. SQUID samples were cut from the heat treated dog-bone shaped samples using diamond blade with weight less than 40 mg. The samples for microprobe were mechanical polished without etching.

The determination of the accurate volume fractions of multiple phases existing in these steels is still a very challenging problem to date. To distinguish the four phases in these steels, i.e. ferrite, bainite, martensite and retained austenite, tint etching can be used after mechanical polishing [132, 133]. However, it is very hard to quantify the phases through optical images even with good tint etching and the repeatability is not good enough. XRD measurement is main technique for determining the volume fraction of austenite. However, the results could be affected by crystallographic textures. Also, in XRD measurements, it is very hard, if not impossible, to differentiate ferrite, bainite and martensite. In the present study, a set of experiments were performed to obtain the

volume fractions of the phase constitutions using the combination of SEM, XRD, and SQUID.

Ferrite volume fraction was determined through point counting on low magnification SEM images, which were captured on samples with only IA. Theoretically, the ferrite formed during IA should remain unchanged after the second stage BIT heat treatment. Also, no more ferrite was supposed to form during the second stage heat treatment assuming the cooling rate between IA and BIT is fast enough. The point counting was performed using image analysis software (i.e. JMicrovision®) with 500 points on each image. An average of 5 images was calculated for each condition. The advantage of monitoring the sample after IA was the simplification of the microstructure from a triple phase structure to a dual phase one. Figure 8 shows an example for sample after IA at 750°C for 2hrs. After mechanical polishing and etching, the sample was monitored under SEM. The dark area is ferrite and bright one is martenstie. Through image analysis, the volume fraction of ferrite was determined to be about 34%.

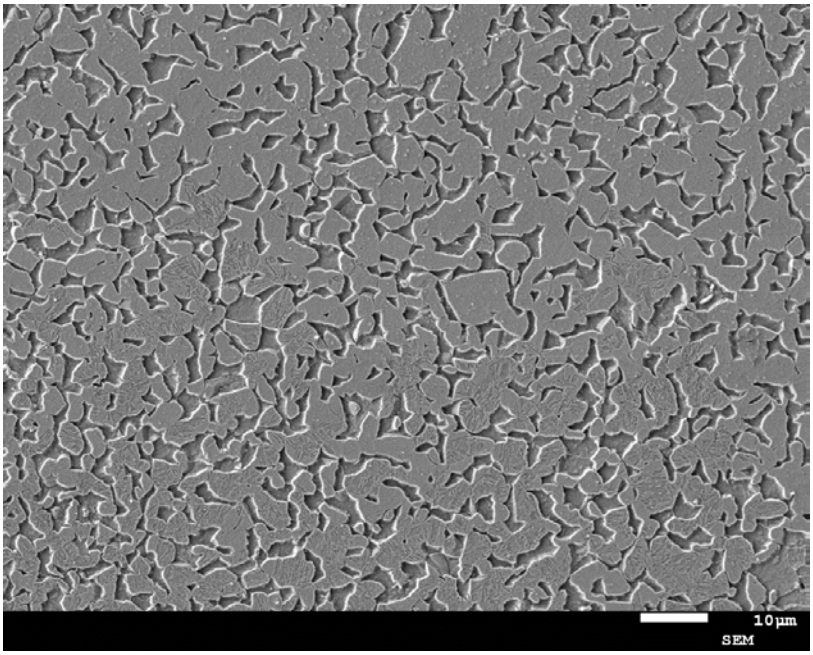

Figure 8. Dual phase microstructure of the Fe-1.42Mn-1.56Si-0.32C sample containing ferrite and martensite. The sample was heat treated at 750°C for 2hr followed by water quenching

The volume fraction of retained austenite was calculated based the XRD pattern following SAE SP-453 [134] on samples after the two-stage heat treatment. In order to validate the calculated results, SQUID was utilized using the reported method [135]. Here, it is assumed that the saturation magnetization of ferrite, bainitic ferrite and martensite is the same while that of retained austenite is negligible. An example can be shown in Figure 9, where the red curve is from the sample after solutionizing at 1000°C for 1hr and quenching to room temperature (assuming full martensitic), while the black curve is the from sample after two-stage heat treatment (IA: 700°C 10min and BIT: 340°C 20min). If the saturation magnetizations of the black curve and the red curve are

designated as M_1 and M_2, the estimated volume fraction of retained austenite in the sample can be calculated as,

$$V_A = 1 - \frac{M_1}{M_2} \quad (1)$$

which is about 19% in the case. Here, it is worth noting that since the retained austenite exists in the form of blocky and thin films in bainite, the measured retained austenite should contains both. At the same time, bainite (upper bainite in the present study) consists of bainitic ferrite and thin filmed austenite. As the thin filmed austenite has been included in the calculation of retained austenite, only the volume fraction of bainitic ferrite will be estimated instead of bainite in the following.

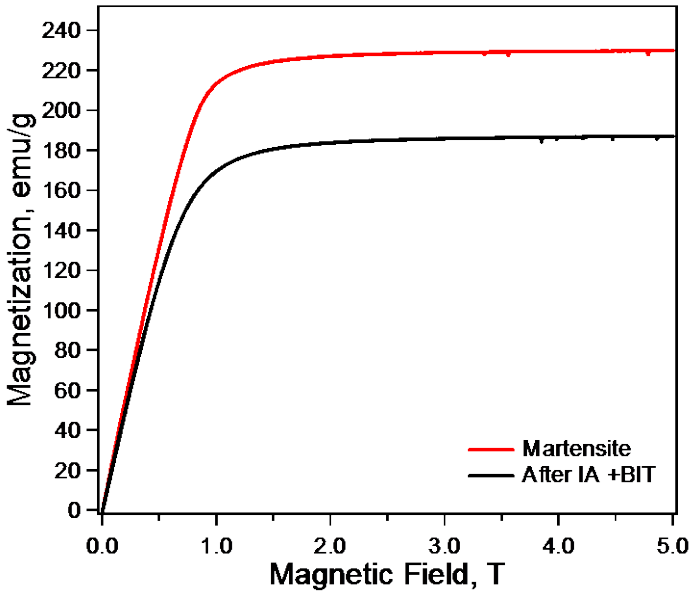

Figure 9. Room temperature magnetization curves of 700°C for 10 min (IA)+ 340°C for 20 min (BIT, black curve), and 1000°C 1hr followed by water quenching (red curve). The chemical composition of the sample is Fe-2.65Mn-0.95Si-0.32C

It has been reported that the martensite can be distinguished from bainite by an additional annealing at low temperature (e.g. 200°C for 1hr) after the two-stage heat treatment [53, 132]. Although this method is beneficial to determine whether martensite exists or not in the microstructure, it is very challenging when utilized to quantify the volume fraction of martensite due to the determination of boundary between bainite, martensite and austenite. In the present study, the method in [25] was utilized. The volume fraction of martensite/austenite islands was first calculated using point counting on the SEM images of samples after two-stage heat treatment. Since the volume fraction of retained austenite could be obtained from previous measurements, the volume fraction of martensite could be calculated as,

$$V_M = V_{M/A} - V_A \tag{2}$$

and the volume fraction of bainitic ferrite could then be estimated as,

$$V_B = 1 - V_F - V_A - V_M \tag{3}$$

3.4 Mechanical Testing

Tensile tests were performed at room temperature using an MTS servo-hydraulic testing system. The strain rate was kept at 10^{-4} s^{-1}. Strain was measured using an Epsilon® extensometer with 8 mm gauge length directly attached on the samples. At least two companion samples were tested for each condition to check the repeatability of the results.

CHAPTER IV

EFFECT OF PHASE CONSTITUTION ON THE MECHANICAL BEHAVIOR OF LOW ALLOY LOW CARBON STEELS

4.1 Optimization of Starting Microstructure through High Temperature Equal Channel Angular Processing

Figure 10 shows an optical microscopy image on the sample with the chemical composition of Fe-1.42Mn-1.56Si-0.32C in the as-cast condition. The dark area is pearlite while the white area is ferrite. Dendritic structure appears throughout the sample, which is not ideal for successive cold deformation due to elemental segregations. Additional thermo-mechanical processing is thus required to eliminate the dendritic structure.

To obtain an initial uniform and refined microstructure such that we can better process and control the processing variables afterwards, the material was thermo-mechanically processed at high temperatures in two different ways using ECAP. The aim was to have a fully homogenized microstructure with relatively small grain size and phase distribution. First, we tried to heat treat a billet at 950°C for 1hr followed by ECAP at a speed of 1 in/sec and air cooled. Two passes were repeated with route C. Second, the same ECAP procedures were performed on another billet for four times with route E. The microstructures with different processes are shown in Figure 11-12.

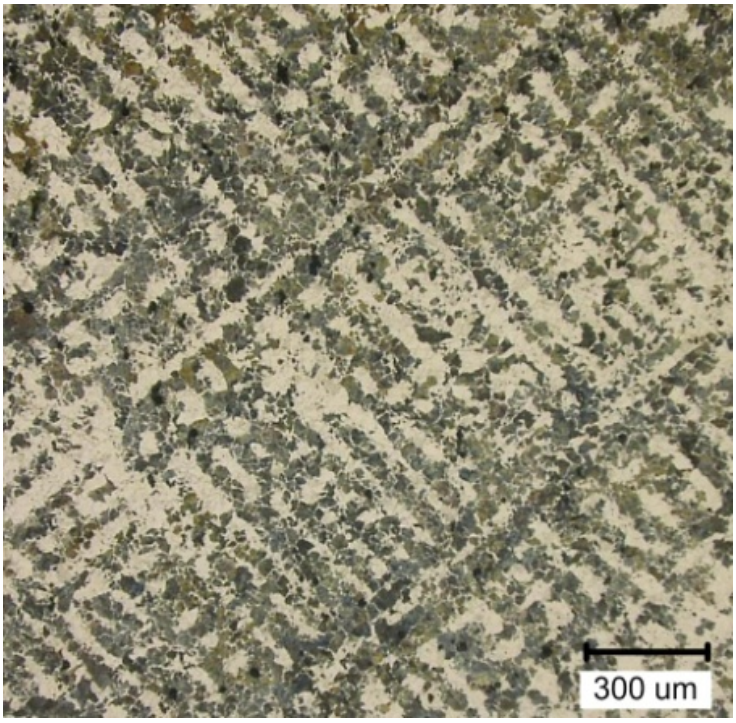

Figure 10. Optical microscopy images of the Fe-1.42Mn-1.56Si-0.32C samples in the as-cast condition. Sample was etched with 2% Nital

Figure 11 shows OM and SEM images recorded after initial ECAP processing with route 2C. It can be seen that the initial dendritic structure is eliminated by the high temperature ECAP processing. In addition, the material has a fairly uniform and homogenized ferrite (bright)-pearlite (black) microstructure according to Figure 11a. Moreover, comparing with the as-cast condition under the same magnification, the grain size of ferrite and pearlite are notably refined. From the SEM image in Figure 11b, the pearlite phase size is estimated to be around 8 μm and the grain size of ferrite is refined down to about 4 μm after ECAP. The volume fraction of ferrite is about 37±3% and that of pearlite is around 63±3%.

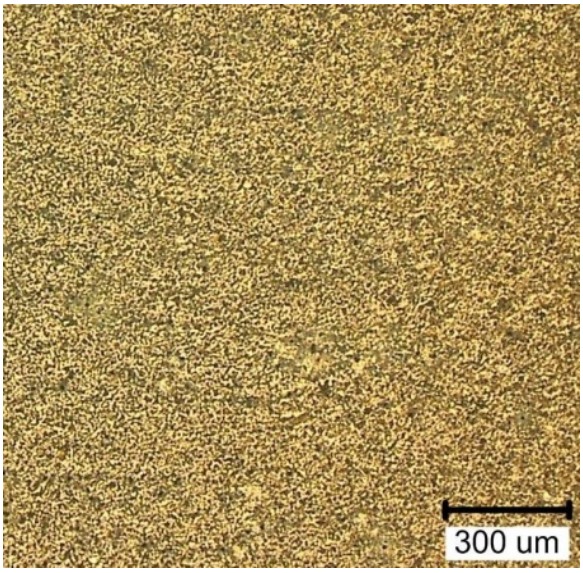

(a)

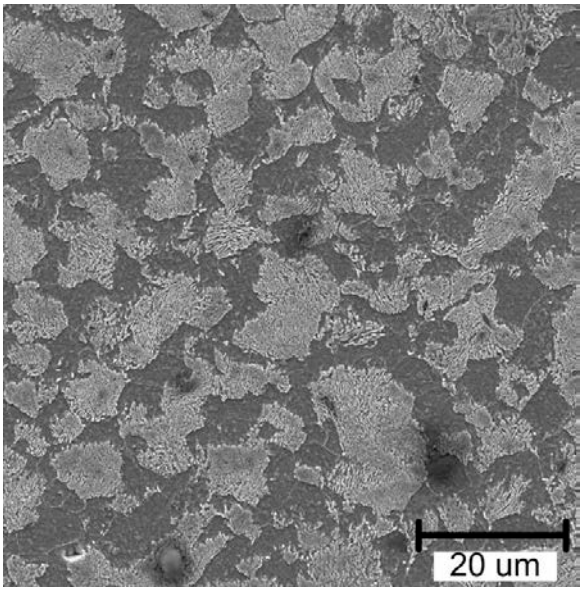

(b)

Figure 11. Optical microscopy images of the Fe-1.42Mn-1.56Si-0.32C samples after 950 °C 1hr + ECAP 2C processing (a). The scanning electron microscopy image in (b) shows the microstructure at a larger magnification. The darker phase is pearlite and ferrite is the white phase in (a). By contrast, ferrite is the dark phase in (b) and pearlite is the brighter phase

Figure 12 shows the optical microscopy image for sample after ECAP with route 4E. Similar as in Figure 11, the dendritic structure is eliminated accompanied with a relatively refined grain sizes. Not much difference can be found between the ECAP with 2C and 4E cases. Thus it can be concluded that two passes of non-isothermal ECAP at high temperature is sufficient for the microstructural homogenization.

Figure 12. Optical microscopy images of the Fe-1.42Mn-1.56Si-0.32C samples after 950°C 1hr + ECAE 4E processing

4.2 Design of Heat Treatment Parameters

To examine the effect of phase constitutions on the mechanical behavior of the material, conventional two-stage heat treatment (IA+BIT) was applied. The parameters of the two-stage heat treatments were designed to systematically vary the volume

fractions of ferrite, bainite, retained austenite and martensite. Detailed list of the heat treatment conditions is summarized in Table 2. Figure 13 shows the calculated equilibrium phase diagram for the present alloy using the Thermo-Calc software and the Fe-based thermodynamic database TCFE6 (V6.2) [136]. The computational calculations are performed by our collaborators (S.Li and Dr.Arroyave) in Texas A&M University. Three temperatures (i.e. 772°C, 780°C and 810°C) between Ac1 (696°C) and Ac3 (816°C) and different times (e.g. 10 mins, 2hrs) were selected in the ferrite-austenite coexisting region for the IA treatment in order to vary the volume fraction of ferrite. Among the three selected temperatures, 772°C was expected to provide the maximum ferrite fraction since it is very close to the eutectoid point [137], while 810°C should result in a low ferrite content since it is close to Ac3. Moreover, it was also expected that short IA treatment durations should lead to more ferrite than longer times at same temperature since the longer heat treatments bring the microstructure closer to the equilibrium state [14]. Note that the grain sizes of ferrite, according to the previous study [137], were expected to be between 3μm to 10μm, thus the grain size differences should not cause significant differences in strength and ductility.

In order to control the morphology of bainite, the BIT temperature was kept the same (340°C) for all treatments. The volume fractions of bainite, retained austenite and martensite were adjusted by varying the holding time at BIT. (i.e. 10 min, 15 min, and 1hr). In addition, due to the same processing route on the same initial microstructure for all examined conditions (e.g. IA at the ferrite+austenite region of the equilibrium phase diagram followed by BIT at the same temperature), the texture differences between

different cases are not expected to be significant. Through the combination of image analysis, XRD, SQUID, and uniaxial tensile testing, the phase constitutions, average carbon content in austenite, as well as the mechanical properties are collected and they are summarized in Table 2. The deviation of the volume fractions of ferrite and martensite were estimated from SEM images from multiple locations of the samples, while the deviation for the retained austenite and carbon content were calculated from multiple companion samples.

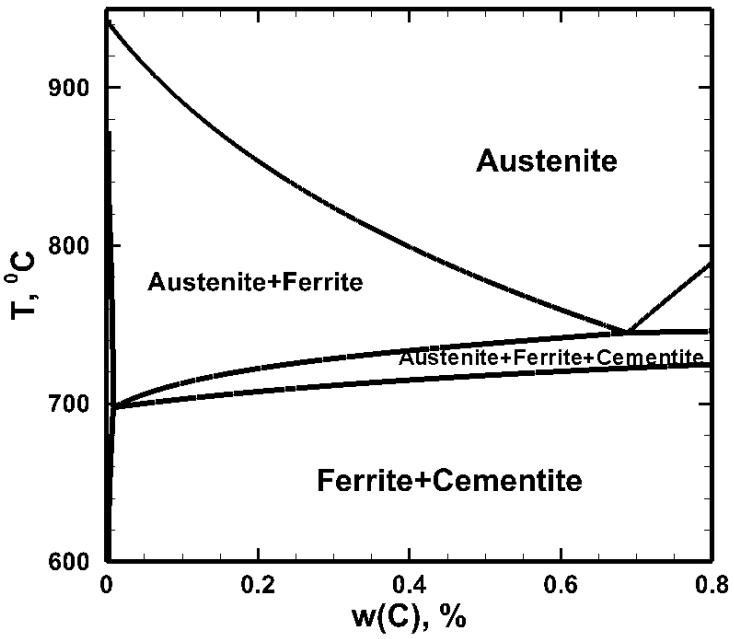

Figure 13. Equilibrium phase diagram of Fe-1.42Mn-1.56Si-0.32C alloy calculated based on thermodynamic database TCFE6 (V6.2)

Table 2. The results of the phase constitution analysis and mechanical characterization after various heat treatments on the model TRIP-assisted steel composition. V_A: Volume fraction of retained austenite, IA: Intercritical Annealing, BIT: Bainitic Isothermal Transformation

Condition	Intercritial annealing (IA)	Bainitic isothermal transformation (BIT)	Volume Fraction, %				Average Carbon in RA from XRD, wt%	Av.Car/ Av.V_A from XRD	True Uniform Strain, %	True Tensile strength, MPa	Yield stress, MPa	Toughness, MPa
			Ferrite	Bainitic ferrite	Martensite	Retained Austenite (RA)						
1	772°C 10min	340°C 10min	52.7±3.0	14.4	24.0±3.1	8.9±1.0	1.03±0.01	11.6±0.3	12.7±0.2	1289±51	650±35	138.8±3.7
2	772°C 10min	340°C 15min	52.7±3.0	24.9	10.9±1.4	11.5±3.3	1.09±0.06	9.1±0.7	20.9±1.4	1294±15	668±21	248.1±3.6
3	772°C 10min	340°C 1hr	52.7±3.0	27.3	6.6±3.7	13.4±2.8	1.18±0.05	8.8±1.7	19.1±1.1	1161±5	654±11	206.4±9.6
4	772°C 2hr	340°C 10min	41.2±0.8	18.1	30.3±2.6	10.4±1.0	1.07±0.06	10.3±0.5	9.7±1.5	1385±42	840±29	118.2±15.2
5	772°C 2hr	340°C 15min	41.2±0.8	29.5	17.5±2.6	11.8±3.0	1.12±0.05	9.5±1.4	17.4±0.9	1275±6	678±5	202.9±9.7
6	772°C 2hr	340°C 1hr	41.2±0.8	32.5	13.7±3.7	12.6±1.2	1.30±0.02	10.3±0.9	17.1±1.3	1210±36	728±3	188.7±9.2
7	780°C 2hr	340°C 15min	29.1±1.5	29.2	28.1±3.7	13.6±0.4	1.44±0.02	10.6±0.4	10.2±1.1	1334±38	820±33	117.5±13.9
8	810°C 2hr	340°C 6min	15.1±0.5	34.9	41.2±4.9	8.8±0.8	1.45±0.05	16.4±0.1	7.7±0.1	1388±9	864±10	96.8±0.3
9	810°C 2hr	340°C 15min	15.1±0.5	35.5	41.8±2.3	7.6±1.0	1.50±0.11	19.7±1.8	7.4±1.4	1524±15	1104±4	95.7±6.4

4.3 Microstructure Evolution

Figure 14 shows the SEM images after each step of heat treatments on few selected heat treatment conditions from Table 2. The lamellar structure (pearlite) observed in Figure 11 is dissolved and a ferrite-martensite structure, as indicated with arrows in Figure 14a, is obtained after the IA. A clear difference in terms of ferrite content can be seen in Figure 14a-14c for different IA conditions (772°C 10min, 772°C 2hr, and 810°C 2hr, respectively). The 10 min (Figure 14a) case shows more ferrite than the 2hr (Figure 14b) one with the same IA temperature. At the same time, the 810°C case (Figure 14c) has less ferrite than the 772°C one (Figure 14b) with the same IA time. The grain size of ferrite is estimated to be in the range of 3~10μm. The volume fraction of ferrite right after the IA is considered the same as the volume fraction of the ferrite in the final microstructure after two step heat treatment, assuming the quenching rate from IA to BIT is fast enough to restrict further ferrite formation. The volume fractions of ferrite for all conditions considered in the present work are listed in Table 2. Figure 14d shows an example of multiphase microstructure after the IA+BIT treatment (780°C 2hr+340°C 15min) with the arrows indicating different phases.

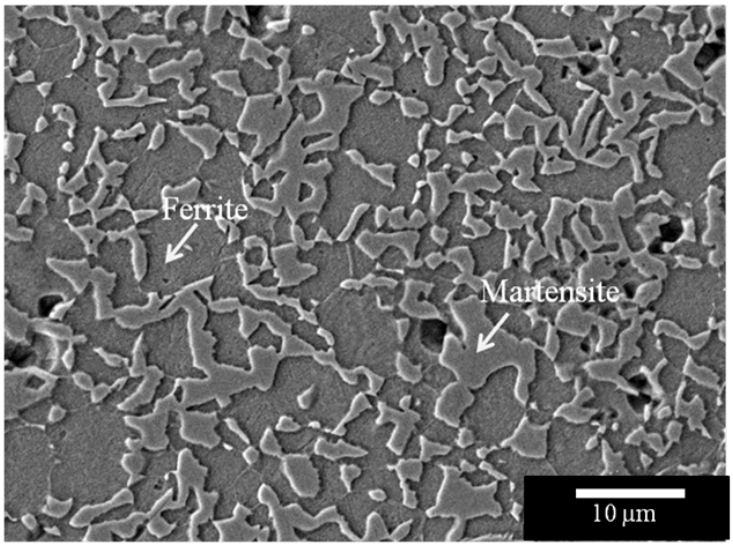

(a)

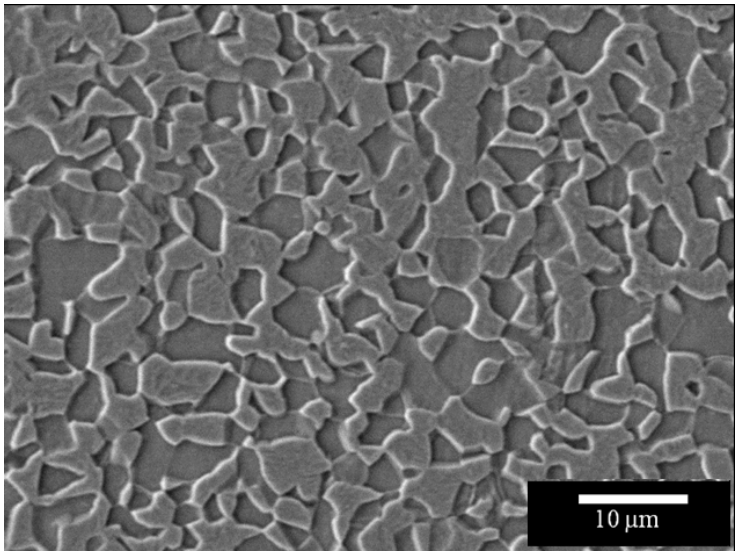

(b)

Figure 14. Scanning electron microscopy images showing the ferrite-martensite microstructure after the IA treatment at 772°C 10min (a), 772°C 2hr (b), 810°C 2hr (c) and the multiphase microstructure after the IA at 780°C 2hr followed by 340°C 15min heat treatment (d). The samples were etched using 2% Nital. The volume fractions of ferrite are summarized in Table 2

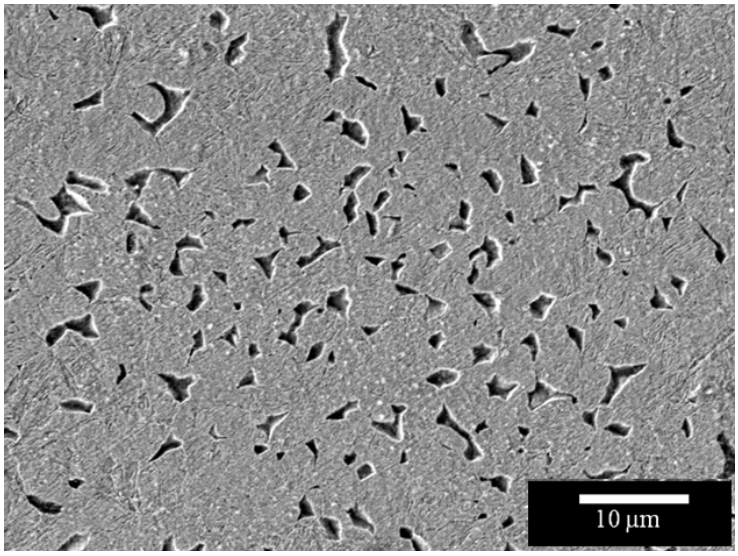

(c)

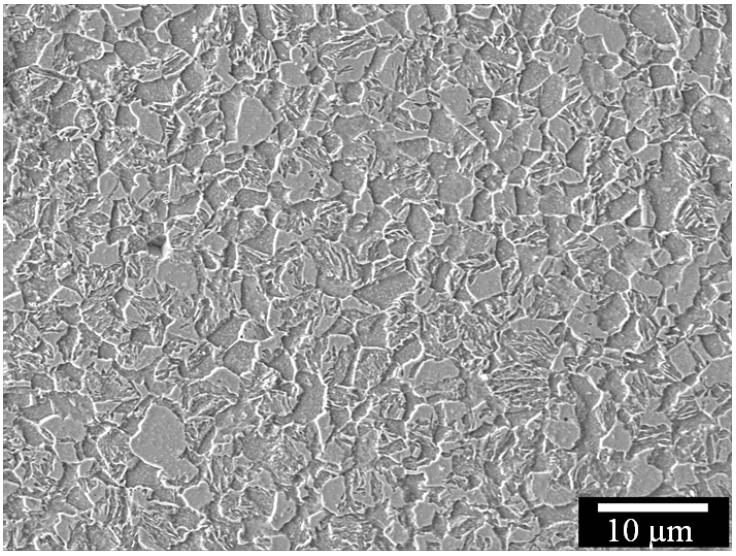

(d)

Figure 14. Continued

4.4 Mechanical Behavior vs. Phase Constitutions

Figure 15 shows the mechanical response of several cases in Table 2. It is observed that the ductility could vary from about 8% to 20% by simply adjusting the heat treatment parameters and thus, the phase constitutions. At the same time, clear differences could also be seen for yield stress and tensile strength. In order to further reveal the effect of each phase on these mechanical properties, the volume fractions of the phases and carbon content in retained austenite in Table 2 are plotted as a function of uniform strain, tensile strength and yield stress in Figure 16-18.

Figure 16a and 16b shows the relation between true uniform strain and carbon content, and volume fraction retained austenite of retained austenite, respectively. The uniform strain does not seem to be correlated to the carbon content in Figure 16a. In Figure 16b, the uniform strain in general increases with the volume fraction of retained austenite (V_A), but there are large variations in this general trend. Thus, no clear trend could be concluded from either of the two figures.

By contrast, Figure 16c shows the relation between the true uniform strain and the volume fraction of martensite. A linear curve fitting is possible through the data points. Clearly, the uniform strain decreases with the increase in the martensite fraction from 5% to about 40%. The observed trend is similar to that for DP steels [130].

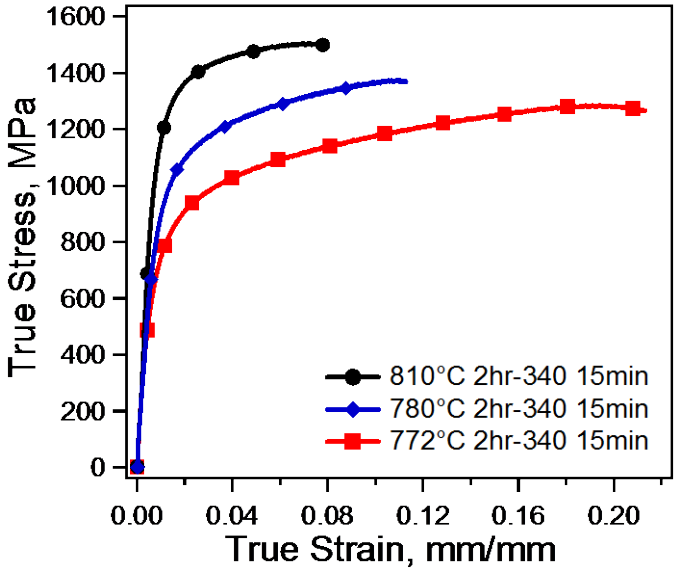

Figure 15. Mechanical responses of selected cases with different heat treatments in Table 2 (e.g. IA at 810°C, 780°C, 772°C for 2hrs and BIT at 340°C for 15 mins)

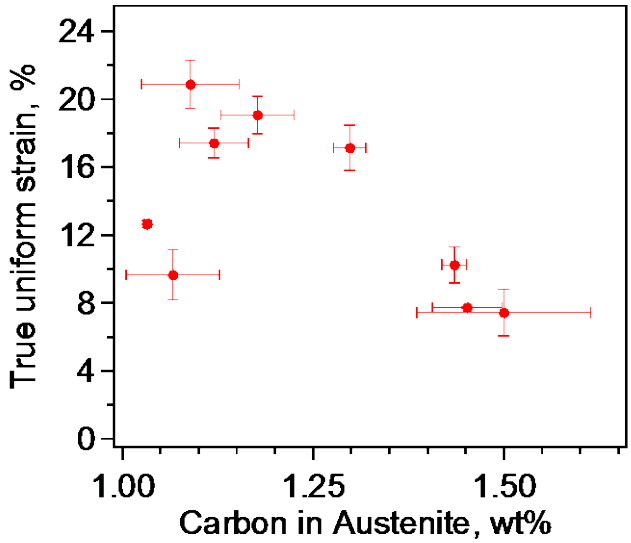

(a)

Figure 16. True uniform strain as a function of (a) carbon content in the retained austenite, (b) retained austenite volume fraction, and volume fraction of martensite (c). A linear curve fitting was possible in (c) indicating the strong effect of martensite on the uniform strain

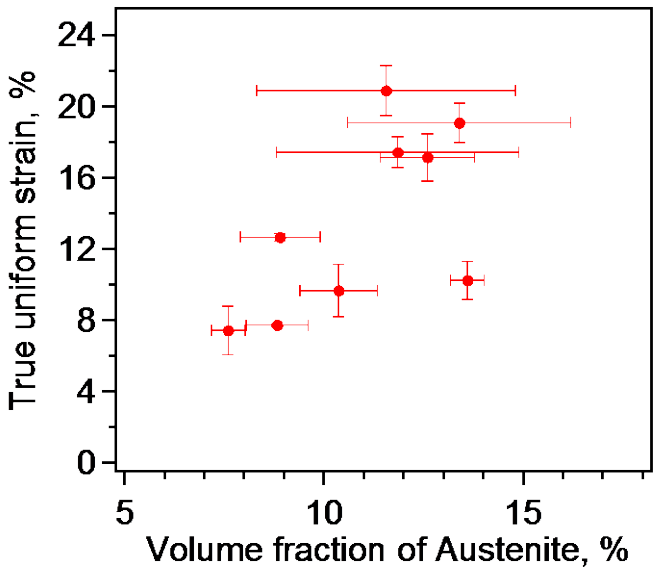

(b)

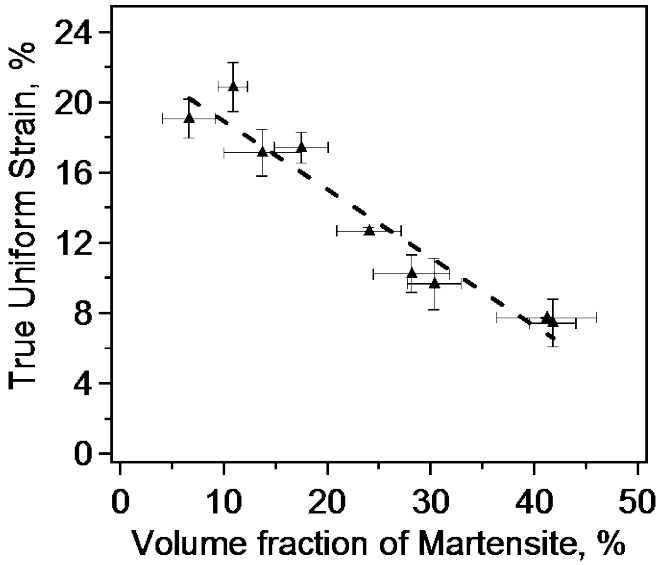

(c)

Figure 16. Continued

Figure 17a shows the uniform strain as a function of ferrite. A general trend could be found as the uniform strain increases with the ferrite volume fraction from about 15% to 55%. At the same time, the volume fraction of ferrite shows an inverse correlation with the volume fraction of martensite in Figure 17b, which indicates that the increase in volume fraction of ferrite is to some extent at the expense of the reduction of martensite content and moreover, the replacement of martensite with ferrite is beneficial to better ductility.

Figure 18 summarizes the yield strength and true tensile strength as a function of austenite (Figure 18a), and martensite (Figure 18b) volume fraction. For the austenite volume fraction, there does not seem to be a clear trend with either yield strength or tensile strength. On the other hand, both the tensile and yield strength increase proportionally with the increasing martensite volume fraction. Approximately 400MPa are gained for both yield and tensile strengths with 35% increase in the martenite volume fraction. A similar trend between the martensite volume fraction and yield and tensile strengths has also been reported for dual phase steels [130, 138].

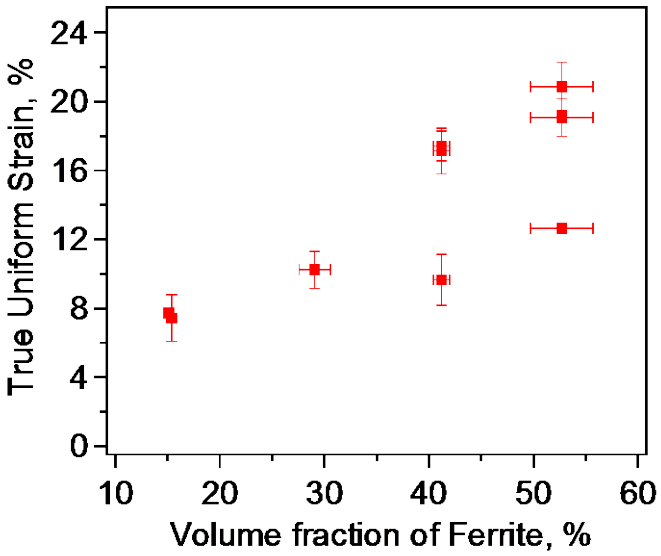

(a)

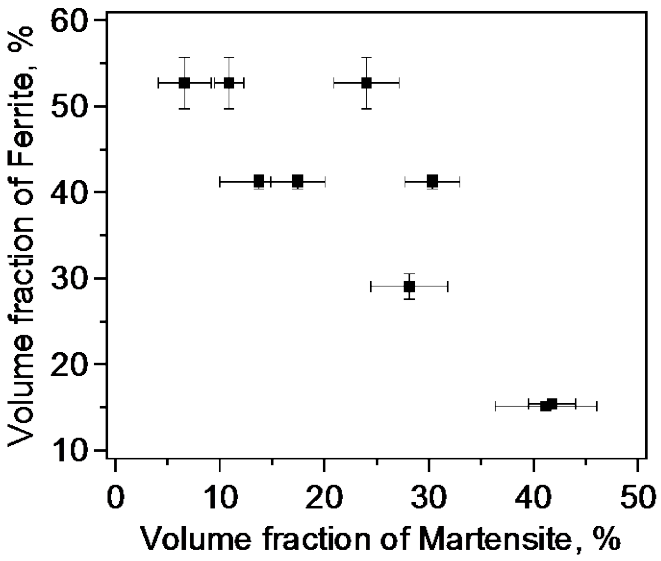

(b)

Figure 17. The uniform strain as a function of the volume fraction of ferrite (a), and the correlation between the volume fraction of ferrite and martensite volume fraction (b)

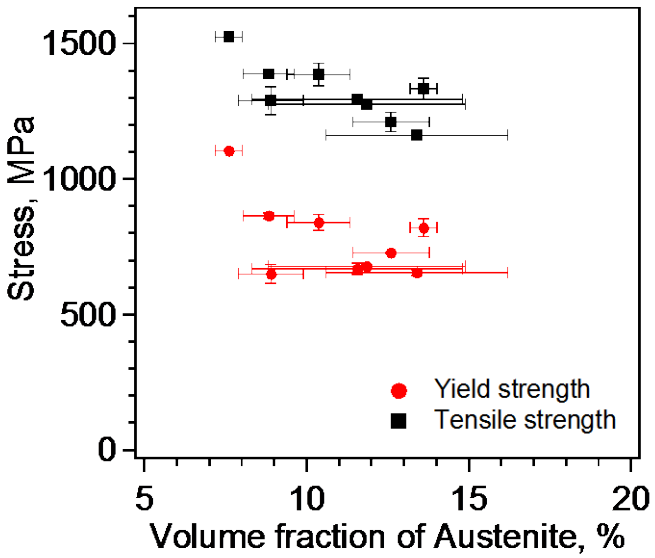

(a)

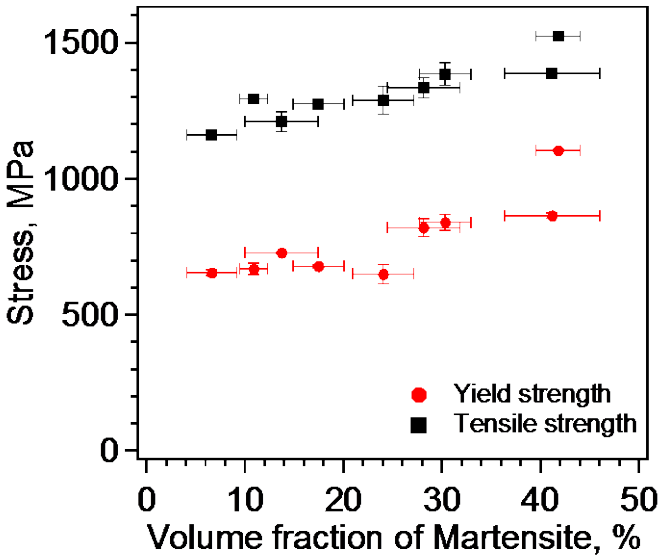

(b)

Figure 18. Yield strength and true tensile strength as a function of volume fraction of austenite (a) and martensite volume fractions (b)

Austenite stability is considered to be one of the most important factors influencing the ductility of TRIP steels. Three factors have so far been proposed as the controlling parameters for the stability of austenite: chemical composition, grain size and mechanical stabilization [29]. Carbon content in retained austenite is regarded as the controlling chemical element for the stability of austenite and thus, ductility, especially for low alloyed steels. However, Figure 16a shows no correlation between the carbon content and the uniform strain, which indicates that austenite stability alone may not control the ductility of the present material. At the same time, the volume fraction of martensite shows a strong correlation with the uniform strain than the volume fraction of austenite, which means that the martensite volume fraction is the main factor controlling the ductility of the multiphase microstructures in the present case. Therefore, the present results indicate that in multiphase TRIP-assisted steels where both martensite and retained austenite exist, the volume fraction of martensite can be used as a better qualitative indicator of uniform strain than the retained austenite stability or volume fraction. However, the volume fraction of martensite can only be measured indirectly and is relatively complicated to calculate. Moreover, for the case in which no martensite exists, it is difficult to predict the ductility of the material if martensite volume fraction is the only criteria to evaluate the ductility. Thus, based on the literature [5, 63, 139] and the present results, it can be argued that if the martensite is absent in the initial TRIP-assisted steel microstructure, the stability and volume fraction of retained austenite can be one of the controlling factors for uniform strain.

4.5 The Role of Retained Austenite on the Flow Behavior

Since neither the carbon content in austenite nor the volume fraction of austenite show a promising correlation with ductility with the present results, the remaining question, then, is the relative importance of stability and volume fraction of retained austenite indicating ductility. It is clear in Figure 16a and 16b that the correlation between retained austenite stability, volume fraction of austenite and uniform strain is weak, if exists at all. As an alternative parameter, Figure 19a shows the true uniform strain as a function of the carbon content divided by the volume fraction of retained austenite (C/V_A) for all the studied cases. The uniform strain shows a much clearer trend with the C/V_A ratio than either carbon content or volume fraction of retained austenite. An exponential curve fitting is performed to indicate a trend between uniform strain and the C/V_A ratio. With the increase in the C/V_A ratio up to 12, the uniform strain first drops drastically from 22% to around 10%, and then further decreases to 8% with a slower pace for the C/V_A ratios up to about 20. The error bar in the figure represents the sample variation.

Such trend is probably related to two underlying mechanisms. First, carbon content determines the stability of retained austenite (not considering the other factors such as grain size and mechanical stabilization), in other words, the percentage of retained austenite that can be transformed into martensite during deformation. High carbon content leads to the over-stabilized retained austenite which is hard to transform to martensite during deformation at room temperature. If the carbon content is combined

with the volume fraction of austenite, the C/V_A ratio could then to some extent be understood as an indicator of the amount of transformable retained austenite.

Secondly, the slower decrease of uniform strain with C/V_A ratio (>12) is probably due to the present of high martensite volume fraction (condition 4, 7-9 in Table 2). The martensite volume fraction are all higher than 28% when the uniform strain shows a much slower decrease with increasing C/V_A ratio in Figure 19a. In other words, although the C/V_A ratio of retained austenite is a better indicator for the uniform strain than carbon content or volume fraction of retained austenite, it is still a second order factor as compared with the martensite volume fraction for the qualitative prediction of ductility. In addition, it needs to be emphasized that the proposed C/V_A ratio is only a simplified parameter to predict the uniform strain since other factors, such as the grain size of austenite and ferrite, could also be important for the ductility. Nevertheless, the C/V_A ratio is much easier and accurate to determine using XRD measurements than determine martensite volume fraction.

In addition, a similar trend could be observed between the toughness and C/V_A ratio of austenite in Figure 19b. The toughness in the present work is taken as the area under the true stress-strain curves up to the maximum uniform strain. The error bar is estimated from the measurements of different samples. Based on Figures 19a and 19b, if the C/V_a ratio of the austenite is considered as design criteria for optimizing phase constitution in TRIP-assisted steels, one is able to obtain a good uniform strain together with a good combination of strength and ductility, which could be another advantage of this new parameter.

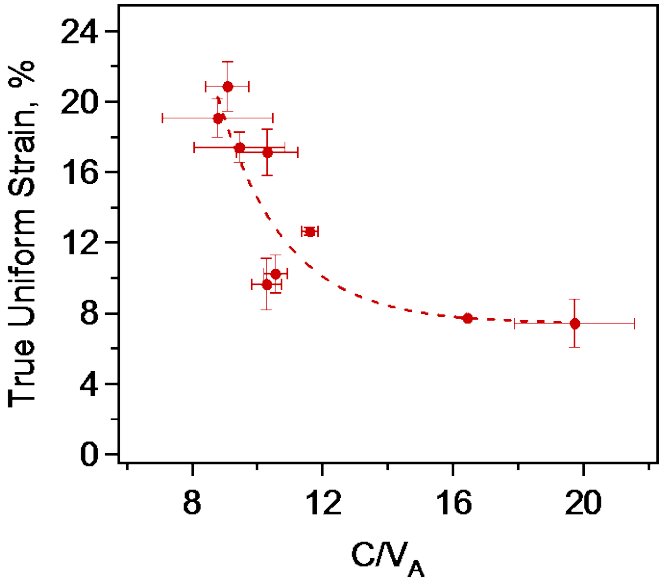

(a)

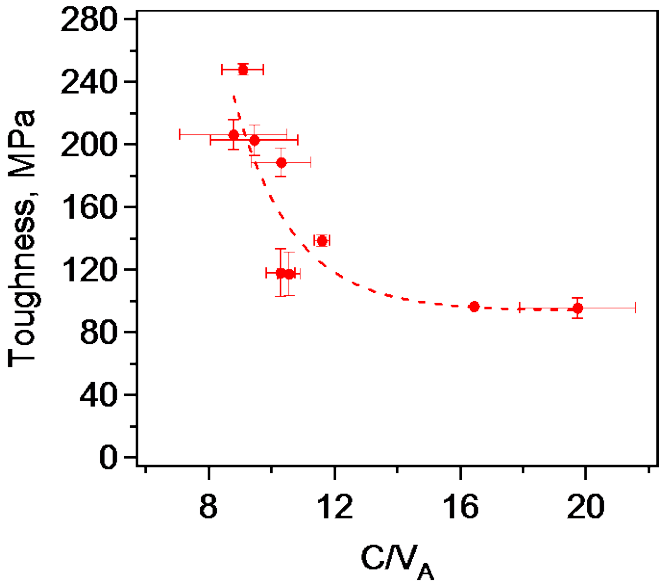

(b)

Figure 19. True uniform strain (a) and toughness (b) as a function of the C/V_A ratio (carbon content divided by the volume fraction of retained austenite). Exponential curve fitting was performed in both figures, indirectly pointing out the effect of martensite on uniform strain and toughness, especially when the volume fraction of martensite is large (the flat region)

CHAPTER V

DESIGN OF HEAT TREATMENT PARAMETERS FOR THE THIRD GENERATION ADVANCED HIGH STRENGTH STEELS

5.1 Microstructure Design Criteria

In this section, the generic microstructural design strategy is explained through the selection of the time and temperatures for the two-stage heat treatment utilizing computational analysis. Specifically, the target was to maximize first the ferrite, and then the retained austenite contents. Although the chemical composition of the model alloy is for Fe-1.42Mn-1.56Si-0.32C, the framework introduced here, however, can be used for any given TRIP steel composition.

Referring to the conventional two stage heat treatment [5, 57, 64], the volume fraction of ferrite is only dependent on the IA, assuming that the quenching rate from the IA to the BIT is sufficiently fast. On the other hand, the volume fractions of bainite and retained austenite are determined by both heat treatments. Thus, the strategy for the present microstructural design is, firstly to find out the IA temperature and time to maximize the volume fraction of ferrite and secondly, determine the temperature and time of the BIT to maximize the retained austenite content. Determination of the IA temperature is straightforward through the application of the lever rule on the predicted thermodynamic phase diagram for maximizing the ferrite content. The time for the IA is predicted using kinetics analysis of pearlite-austenite and ferrite-austenite phase transformations.

The martensite formation needs to be suppressed during the BIT and during quenching to room temperature after the BIT in order to maximize the retained austenite fraction. Figure 20 shows a generic schematic for the para-equilibrium phase diagram of a low-alloy TRIP-assisted steel that will help describe the present methodology. The Ac_3 line in the figure indicates the maximum carbon enrichment in the intercritical austenite for a given IA temperature. For a given IA treatment, the intercritical austenite will have a certain degree of carbon enrichment (C_{IA}) after the IA, dictated by Ac_3, which in turn results in a specific martensitic start temperature after the IA (M_S^{IA}). To completely avoid martensite during quenching right after the IA, the BIT temperature must be above this line. Moreover, for a given C_{IA}, bainite transformation can only happen below the bainite start temperature (B_s), as shown in Figure 1.

Further restriction on the selection of the proper BIT temperature arises from the consideration that the retained austenite during the BIT should undergo maximum carbon enrichment in order to maximize its stability against martensite formation. The locus of this maximum enrichment is given by T_0', which corresponds to the temperature—for a given carbon concentration—at which the Gibbs free energies of the austenite and ferrite are equal, taking into account nucleation and strain energy barriers to the formation of bainitic ferrite (~400 $Jmol^{-1}$) [9, 67, 68]. As noted above, beyond this carbon concentration the driving force for the bainitic transformation vanishes. In order to completely suppress the formation of martensite above room temperature, the carbon enrichment during the BIT should be higher than a critical concentration ($C_{Ms=RT}$) shown with a vertical line in the figure. The interception of the $C_{Ms=RT}$ line with T_0' yields the

maximum BIT temperature ($B_{Ms=RT}$) necessary to suppress Ms below room temperature. All these thermodynamic considerations yield a window of allowable BIT temperatures, which is indicated by the yellow region in Figure 20.

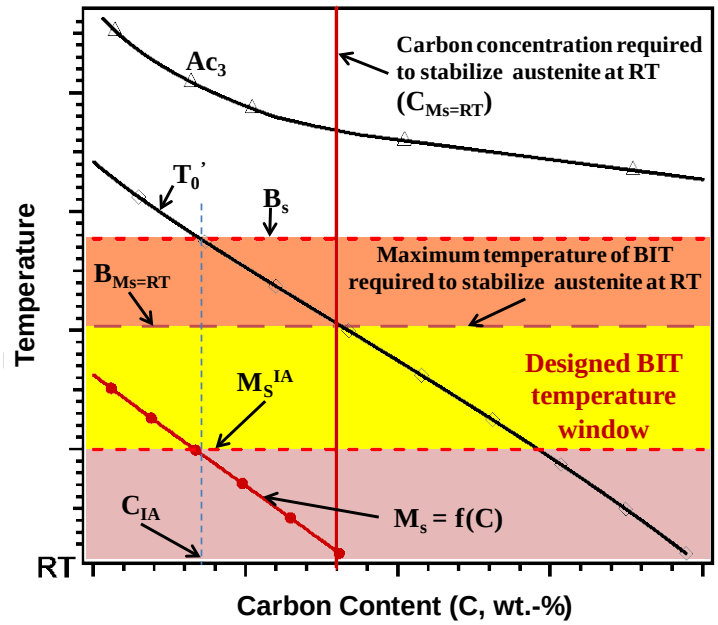

Figure 20. Schematic phase diagram showing the selectable temperature window for the BIT (yellow region) to suppress the formation of martensite after the BIT during quenching to room temperature. See main text for the definition of the abbreviations

5.2 Design of Intercritical Annealing

Figure 13 has shown the predicted phase diagram with Ac_3 and Ac_1 as 816°C and 696 °C. Applying the lever rule on the phase diagram, the holding temperature for the IA (T_{IA}) should be around 772°C to obtain the maximum volume fraction for ferrite. It has been suggested by Emadoddin *et al.* [58] that the IA temperature for maximizing the retained austenite content would be $(Ac_3+Ac_1)/2+20$°C, which is in fact fairly close to

the IA temperature calculated in this study. At this temperature, the volume fraction of austenite (FCC) should be around 67% and that of ferrite (BCC) should be 33% at the equilibrium state. Note that the current approach also aims at completely avoiding cementite formation during the IA.

To further predict the IA holding time, kinetics analysis was performed to evaluate the change of the austenite volume fraction as a function of holding time using DICTRA®, with the mobility database MOBFE1 (version 1.0), as shown in Figure 21a. A very long holding time (about $3x10^7$ s) is required to reach the equilibrium state during the IA. Katsamas *et al.* [140] observed a similar trend between thermodynamic equilibrium and kinetics analysis for IA up to 10^8 s on a low-alloy TRIP-assisted steel (Fe-0.146C-1.28Si-1.33Mn). However, such a long predicted time for the IA ($3x10^7$ s) is not practical to utilize. Thus, experiments were necessary to determine more practical holding times for the IA.

Samples from the ECAP processed billets were IA treated at 772°C for different holding times. According to the metallographic results in Figure 21b, the volume fraction of austenite first decreases gradually with the IA time until around 900 s, then increases gradually, and tends to saturate at around 70% for times longer than 2×10^4 s. The saturation volume fraction of austenite is in good agreement with the earlier thermodynamic prediction of the equilibrium value (≈ 67.5%).

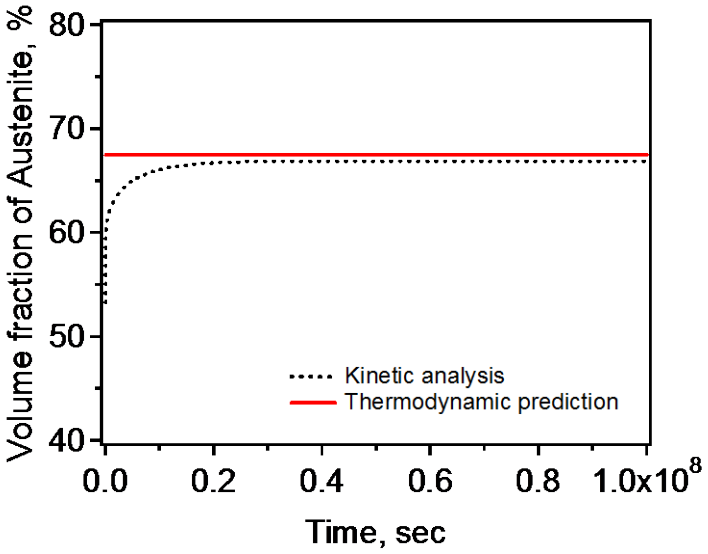

(a)

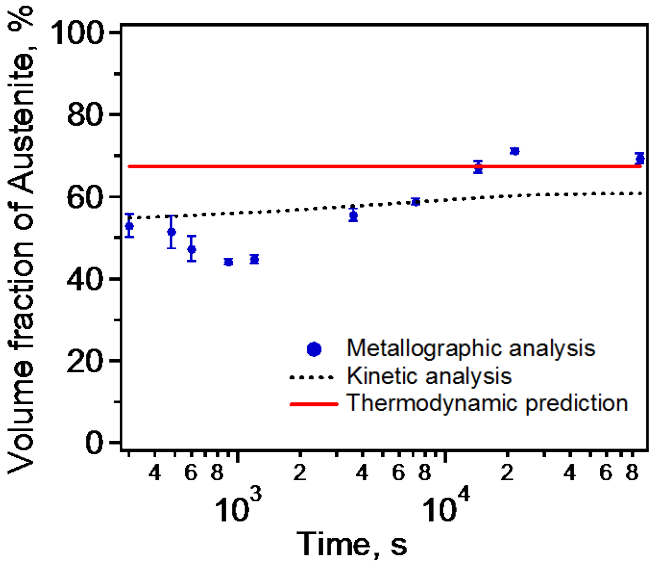

(b)

Figure 21. Austenite volume fraction as a function of the IA holding time predicted using thermodynamic and kinetic analysis (a). Comparison of the austenite volume fraction from metallographic analysis with the theoretical calculations as a function of IA time (b) in the present TRIP steel composition

The initial decrease followed by the increase in the austenite volume fraction during the IA is not expected from either the present thermodynamics or kinetics analysis. The reason for the difference between the experiments and the predictions is not fully clear at the moment. One possibility for such unexpected trend could be due to the heavily dislocated microstructure after initial ECAP processing. With short term IA, carbon atoms tend to diffuse to dislocations which lead to the 'anomaly' phase propagation. With further IA, the heavily dislocated microstructure disappeared and the carbon migrates back to the energy favorable phase (austenite). Moreover, according to Speich *et al*. [14], the austenite formation during the IA can be divided into three stages: pearlite dissolution, austenite growth with carbon diffusion, and elemental partitioning between austenite and ferrite. Pearlite dissolution finishes fairly fast, and thus, cannot be the reason for the observed trend in austenite volume change. Hence, the effect should originate from the way austenite growth and elemental partitioning occurs during the IA. Figure 22a summarizes the diffusion coefficients for C, Si and Mn in both austenite and ferrite as a function of temperature. At 772°C, carbon diffuses much faster than Si and Mn, both in ferrite and austenite, indicating that carbon diffusion is dominant in the early stages of the IA process. Meanwhile, it can be observed in Figure 22b that the chemical potential of carbon in ferrite is lower than that in austenite at 772°C. This in turn suggests that carbon tends to diffuse into ferrite first, leading to the volume shrink of austenite. At longer IA times, Si and Mn partitioning becomes more significant. It can also be observed in Figures 22a and 22b that Si has a higher diffusion coefficient and lower chemical potential in ferrite at 772°C, and thus, tends to diffuse into ferrite. At the

same time, Mn tends to become enriched in austenite for its higher diffusion coefficient and lower chemical potential in austenite. Such elemental partitioning might lead to a redistribution of carbon with the increase of the IA time, and thus, to the subsequent increase in the volume fraction of austenite. Referring to the thermodynamic prediction, the equilibrium volume fraction of austenite is about 67.5%, which is much larger than the minimum value observed in the experiment at 900s (44%). To reach the actual thermodynamic equilibrium condition, the volume fraction of austenite has to increase with IA time for IA times longer than 900s.

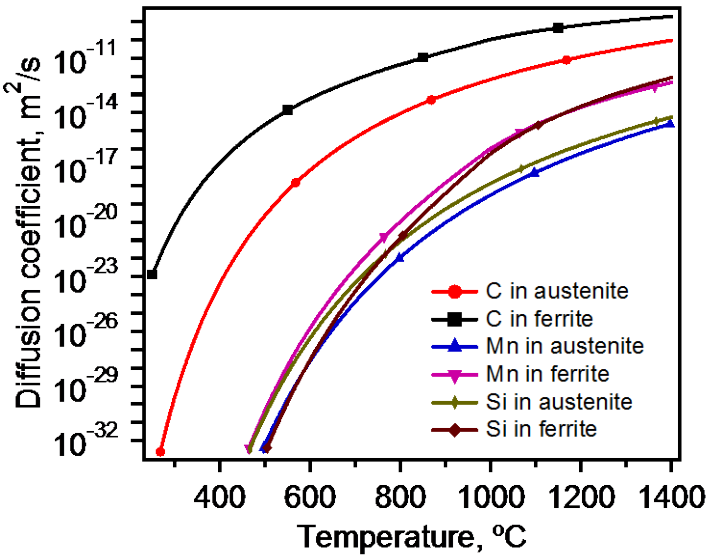

(a)

Figure 22. Diffusion coefficient (a) and chemical potential (b) of carbon, silicon and manganese in austenite and ferrite as a function of temperature as obtained from thermodynamic and kinetic databases

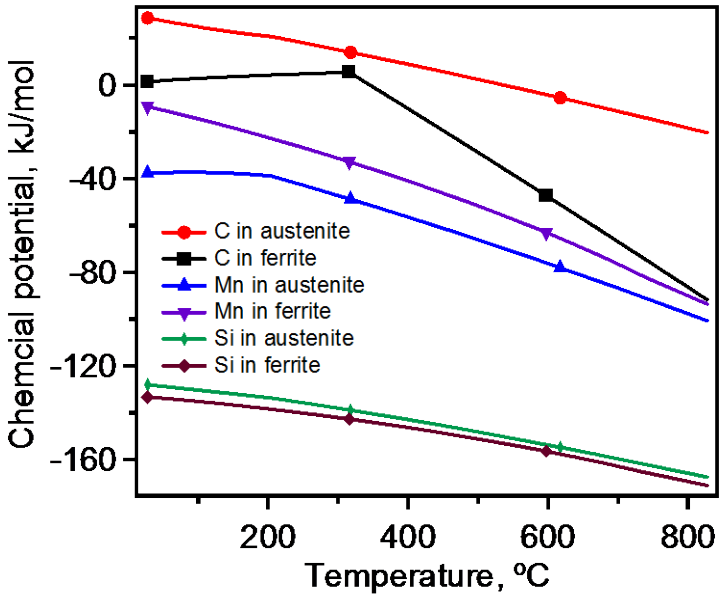

(b)

Figure 22. Continued

To experimentally validate this rationale, Si and Mn concentrations were determined experimentally using WDS and results are reported in Figure 23. The Si concentration in ferrite decreases from about 1.6 wt.-% to around 1.4 wt.-% in 1.2 ks and gradually increases up to about 1.9 wt.-% when annealed for 85 ks and longer. Since Si has a low solubility with carbon, the 'net' direction of carbon diffusion should be opposite to that of Si. As a result, carbon tends to diffuse into ferrite first and then back to austenite with IA time, which agrees with the observed trend for the volume fraction of austenite. In addition, the WDS results show a noticeable fluctuation of the Mn content in austenite as the IA time increases. It is worth mentioning that the WDS

measurement may not reflect the real Mn content in austenite since the Mn has a much lower diffusivity in austenite than in ferrite (see Fig. 22a) and Mn tends to accumulate at the austenite/ferrite interfaces [29, 141]. This segregation of Mn introduces significant spatial variation in the WDS measurements.

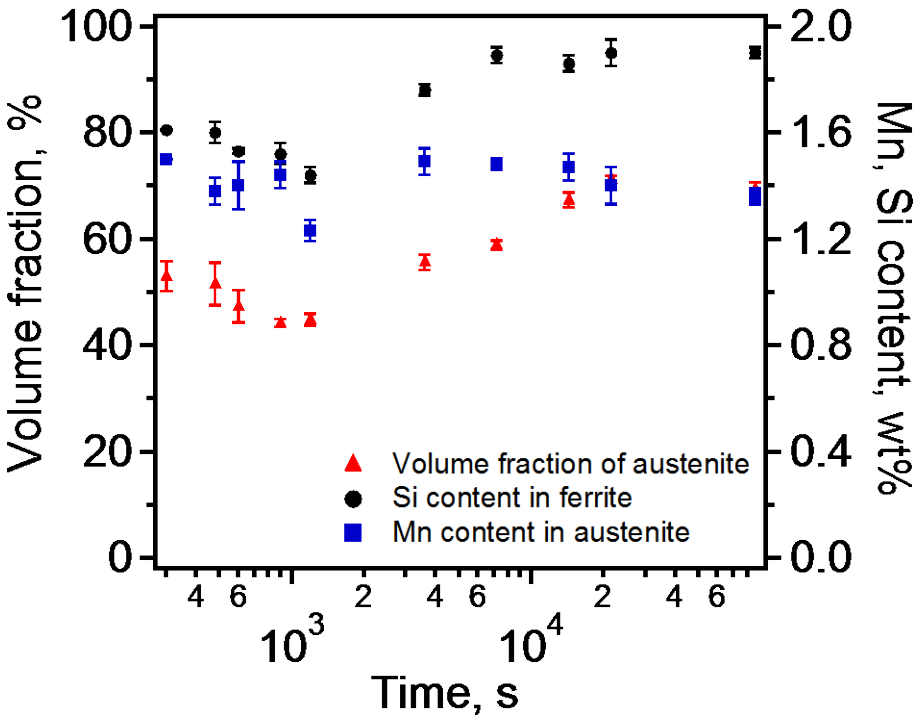

Figure 23. Si content in ferrite (black dots) and Mn in austenite (blue squares) determined using WDS as a function of IA time

Comparing the experimental and computational results in Figure 21b, it is possible to achieve the ferrite volume fraction predicted from the thermodynamic

calculations. However, due to the observed reduction of the austenite content during the early stages of the IA treatment (Fig. 21b and 23), it is also possible to achieve higher ferrite content than under equilibrium condition. To follow the hypothesized criterion of maximizing the ferrite fraction, a reasonable selection for the IA time is between 600s and 1200s. Although the maximum ferrite could be obtained by an IA for around 900s, the IA time was selected as 600s at 772°C to balance the effects of grain growth and ferrite volume fraction on the resulting mechanical properties.

5.3 Design of Bainitic Isothermal Transformation

The second step of thermodynamic analysis consists of the calculation of the thermodynamic state at the end of the BIT. Since the ferrite is stable between the IA and the BIT (assuming sufficiently fast quenching), it is not included in this calculation. The composition of the austenite after the IA with the designed heat treatment parameters was taken as the initial state for the BIT. However, since it is hard to calculate the composition while it is in non-equilibrium condition, the chemical composition of austenite was calculated assuming the equilibrium condition is reached, as shown in Table 3.

Table 3. Predicted chemical composition (in wt.-%) of austenite after the IA treatment used to calculate the phase diagram and TTT diagram for the BIT

C	Mn	Si	Fe
0.545	1.4	1.7	Balance

Figure 24 shows the phase diagram of the alloy with the composition listed in Table 2. M_s and M_f were calculated using the approach given in Refs. [142, 143]. The line marked T_0' indicates the limitation of the bainitic transformation assuming the strain energy barriers of bainite as 400 $Jmol^{-1}$ [9]. As the bainitic transformation progresses, formation of new bainite induces further carbon enrichment of the remaining austenite. When the carbon concentration in austenite reaches the T_0' line, the driving force for the transformation from austenite to bainite vanishes. In other words, T_0' indicates the local maximum carbon enrichment of the austenite after the BIT (Figs. 20 and 24).

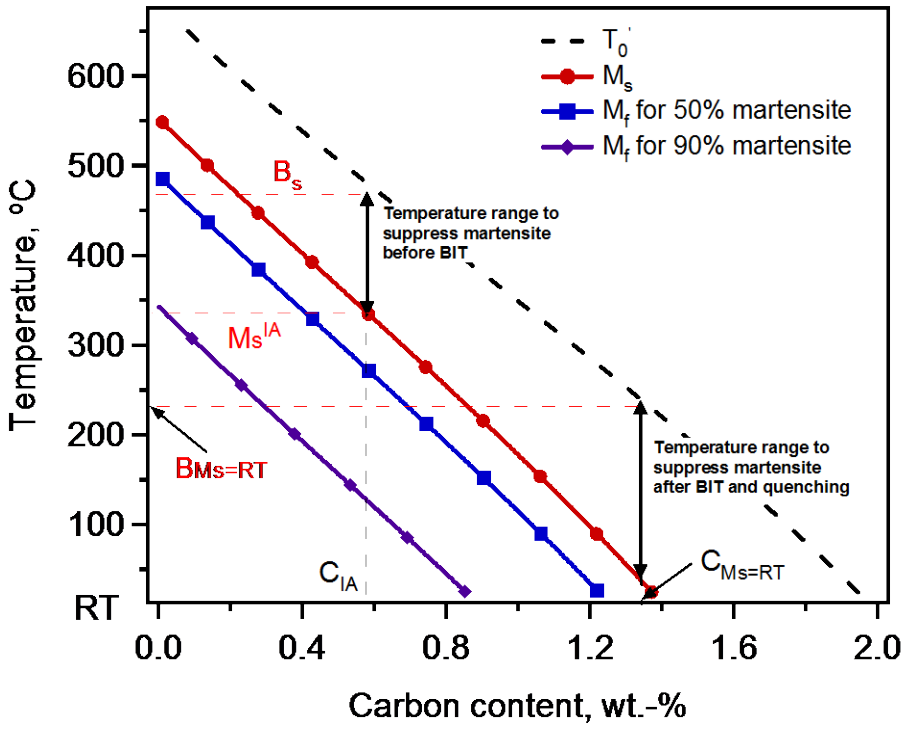

Figure 24. The phase diagram of the austenite after IA, with the chemical composition given in Table 3, calculated based on TCFE6 (V6.2) database. M_s and M_f are shown as a function of carbon concentration. T_0' (black dashed line) shows the maximum carbon enrichment in retained austenite as a function of the BIT temperature. C_{IA} is the carbon concentration of austenite after the specific IA treatment (772°C 600s), B_s is the corresponding maximum BIT temperature and M_s^{IA} is the corresponding M_s temperature. $C_{Ms=RT}$ is the carbon concentration of austenite required to fully suppress martensite during quenching after the BIT and $B_{Ms=RT}$ is the BIT temperature to reach that carbon enrichment

Figure 25 shows the TTT-diagram calculated based on the austenite composition (Table 3) after the IA treatment. In this work, a Rusell-type theory, which is based on effective diffusivity and maximum driving force available for nucleation, is employed to estimate the incubation time [144-146]. The bainitic transformation is assumed to be diffusion controlled and the bainite plates grow in length rather than in width, resulting

in a quasi-one dimensional growth. The model developed by Quidort *et al.* [145, 147, 148] was implemented assuming that the bainitic transformation can be described using the Johnson-Mehl-Avrami model. The original implemented model considers that austenite transforms into bainite without carbon enrichment in austenite, i.e. excess carbon precipitates as cementite. However, the relatively high Si content (1.56 wt.-%) is believed to be sufficient to suppress the formation of cementite and carbon should thus be enriched in the retained austenite. The BIT stops when the carbon content in the retained austenite reaches T_0'. To account for this in the model, the maximum volume fraction of bainite was calculated by applying the lever rule in the phase diagram. In Figure 25, solid lines indicate how much austenite has been transformed to bainite at various time and temperatures after the IA. The dashed line corresponds to the maximum achievable bainite according to the thermodynamic calculation. It can be concluded that a higher BIT temperature results in a lower completion rate for the bainitic transformation, which is in accordance with the experimental results from Bhadeshia *et al.* [144, 149].

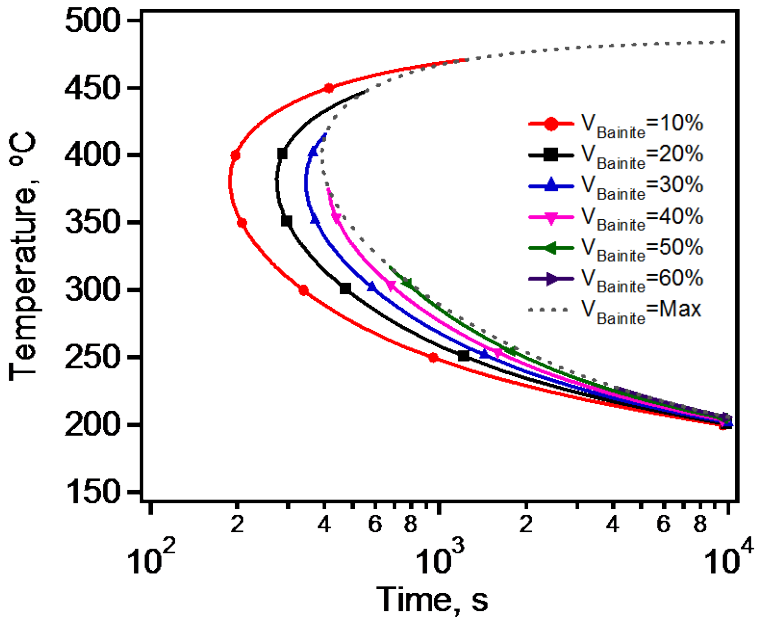

Figure 25. TTT diagram of the austenite with the chemical composition from Table 2 calculated by diffusion controlled model. $V_{Bainite}$=Max (dashed line) indicates the maximum bainite that can form at a given BIT temperature

To satisfy the second microstructure design criteria, i.e. to maximize the retained austenite content, the formation of martensite needs to be suppressed before and after the BIT. It was mentioned that the BIT temperature needs to be within the temperature range marked yellow in Figure 20, where the M_s temperature of the alloy after the IA (M_S^{IA}) is lower than the BIT temperature, while the M_s temperature of the alloy after the BIT should be lower than room temperature. As highlighted by the vertical arrows in Figure 24, the carbon concentration of austenite after the BIT ($C_{Ms=RT}$) should be at least 1.4% to fully suppress the martensite formation. According to the T_0' curve, the corresponding BIT temperature ($B_{Ms=RT}$) should not be higher than 220°C. On the other hand, to suppress the formation of the martensite before the BIT, the BIT temperature must be in

the range between 320°C (=M_S^{IA}) and 460°C (=B_s). In other words, the M_S^{IA} temperature is higher than the $B_{Ms=RT}$ temperature shown in Figure 20. Thus, it is impossible to find a BIT temperature to fully suppress martensite for the present model TRIP steel and the microstructure at room temperature after the BIT will always contain some martensite. However, it is worth noting that a possibly more sophisticated thermal path-i.e. a non-isothermal bainitic treatment - could in principle be used to induce a maximum carbon enrichment of the austenite while preventing martensite formation during this enrichment process after cooling down to room temperature, which will be discussed in the next chapter.

To find out the BIT temperature that results in the maximum retained austenite content in the present steel composition, theoretical calculations for the retained austenite volume fractions at various BIT temperatures were performed based on the equilibrium phase diagram and the TTT diagram shown in Figures 24 and 25, respectively, assuming that the bainitic transformation is completed at each temperature, i.e. T_0' is always reached. Figure 26 shows the volume fraction of retained austenite as a function of the BIT temperature for the microstructure at room temperature after quenching from the BIT. A plateau-like region can be observed from about 230°C to around 340°C, which indicates that the volume fraction of retained austenite is probably insensitive to the BIT temperature in this temperature range due to the inevitable formation of martensite. Here, the BIT temperature was selected to be 340°C as a model temperature for a relatively fast transformation kinetics as this temperature is close to the nose of the TTT diagram.

As it can be seen in Figure 26, the calculated volume fractions of retained austenite are relatively small (< 10%). This value may be an underestimation for two reasons. Firstly, the empirical equations used have uncertainties. Secondly, an initially lower austentite content was observed in the experimental results and predicted using thermodynamics (Fig. 21b). This indicates that the carbon content of austenite should be higher before the BIT than predicted, leading to more efficient suppression of martensite. As a result, the actual retained austenite content is expected to be higher than the calculated one in Figure 26.

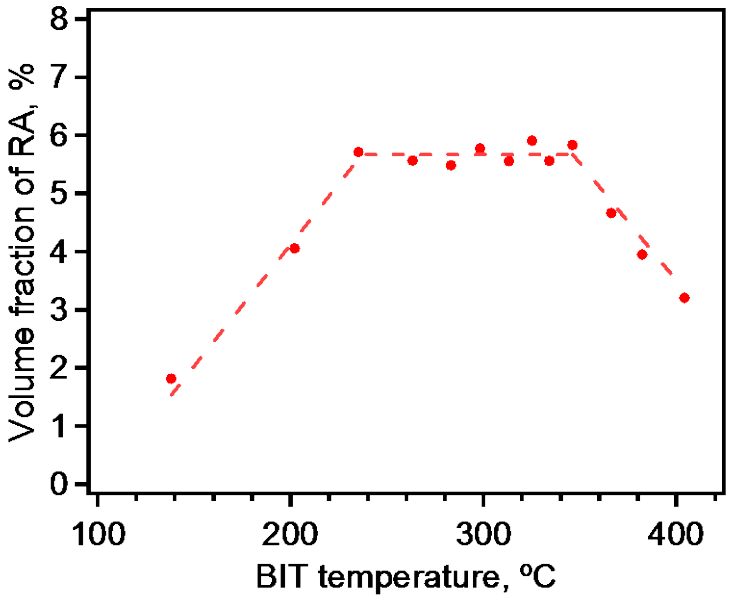

Figure 26. Theoretical calculation of the volume fraction of retained austenite (RA) as a function of BIT temperature

Provided that the BIT temperature is 340°C, the predicted time for the BIT is about 600s according to the TTT diagram in Figure 25. However, considering the fact that the actual Mn content is expected to be a bit higher than the one used to calculate the present TTT diagram due to the partitioning during the IA, the TTT diagram should be shifted to the right to some extent. Thus, the designed BIT time needs to be longer than the predicted value and therefore, selected as 900s in the present work.

5.4 Resulting Microstructures and Mechanical Response

Following the selected heat treatment parameters for the IA and the BIT, the samples were intercritically annealed at 772°C for 600s, fast quenched into a salt bath at 340°C, and then isothermally heat treated for 900s followed by water quenching to room temperature. Figure 27 shows the microstructure after the two-stage heat treatment with the designed parameters. Ferrite, bainite, martensite and retained austenite coexist and are labeled in the figure. With the aforementioned methods, the volume fractions for all phases are determined for the designed condition (IA at 772°C for 600s and BIT 340°C for 900s) and they are listed in Table 4.

Table 4. Measured and calculated volume fractions of the phases in the microstructure after the designed heat treatment. The standard deviations of ferrite and retained austenite fractions are from multiple measurements on the same sample and different samples

Heat treatment	Phase Volume Fractions
772°C 600s + 340°C 900s + Water quenched to RT	53±3% ferrite + 25% bainitic ferrite+ 12±1% martensite + 10±4% retained austenite

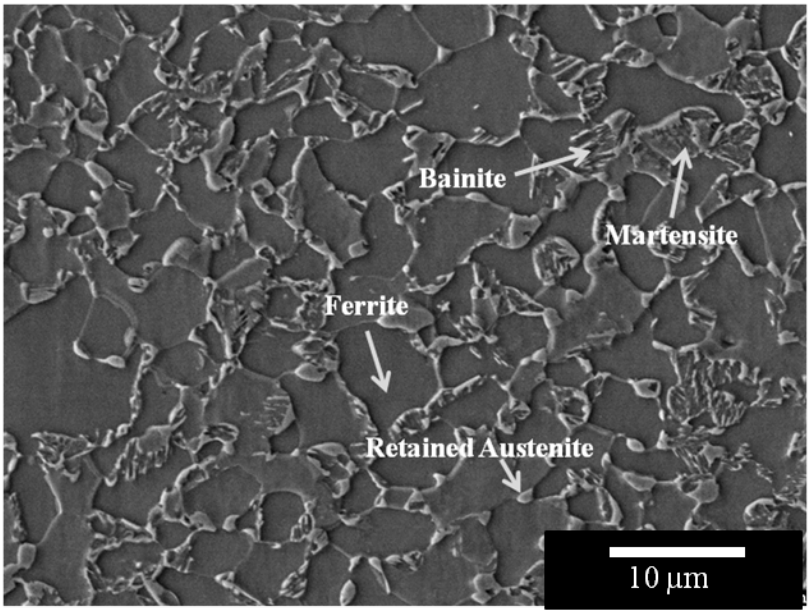

Figure 27. SEM image showing the microstructure at room temperature after the BIT. (772 °C 600 s + fast quenching + 340 °C 900 s + water quenching)

Figure 28a summarizes the true stress vs. true strain responses of the current steel with different thermo-mechanical processing conditions. The green curve shows the

response of the as-cast sample. The red curve stands for the condition after the high temperature ECAP initial processing resulting in a fine ferrite-pearlite structure. The yellow curve is the mechanical response of the material with the designed heat treatment (772°C/600s+340°C/900s). The yield stress, true tensile strength, and true uniform strain of each case are listed in Table 5. All of these properties are improved after the initial processing with high temperature ECAP as compared to those of the as-cast condition. It has been reported that the microstructure banding is intrinsically detrimental to the ductility of dual phase (DP) steel and TRIP steels [150-153]. Therefore, the reason of the improvements could be the absence of banding microstructure and the refinement of grain size. After the IA and the BIT using the designed heat treatment parameters, a further improvement in both tensile strength and uniform strain was obtained. An improved strain-hardening can be clearly seen in comparison with the non-heat treated condition (the red curve) due to the TRIP effect.

To clearly demonstrate the advantage of using the current microstructure design strategy, another heat treatment condition was selected (780 °C/600 s+ 420 °C/900 s) for mechanical testing. Comparing this condition with the designed one, both grain size and texture are expected to be similar. The main difference should lie in the phase fractions. Both ferrite and retained austenite volume fractions were expected to be less than those in the designed condition according to the previous analysis. While the uniform strain and hardening rate seem to be fairly close in the two conditions, the yield strength is higher with the designed heat treatment (Figure 28b), leading to a higher true tensile strength.

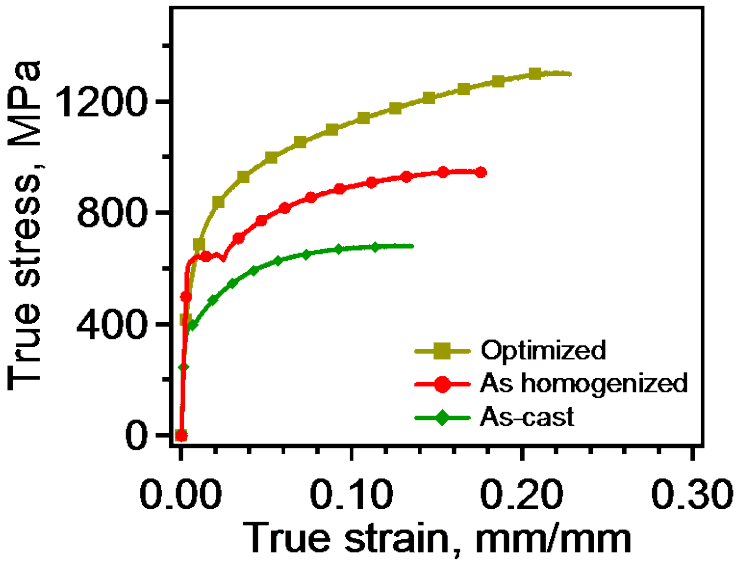

(a)

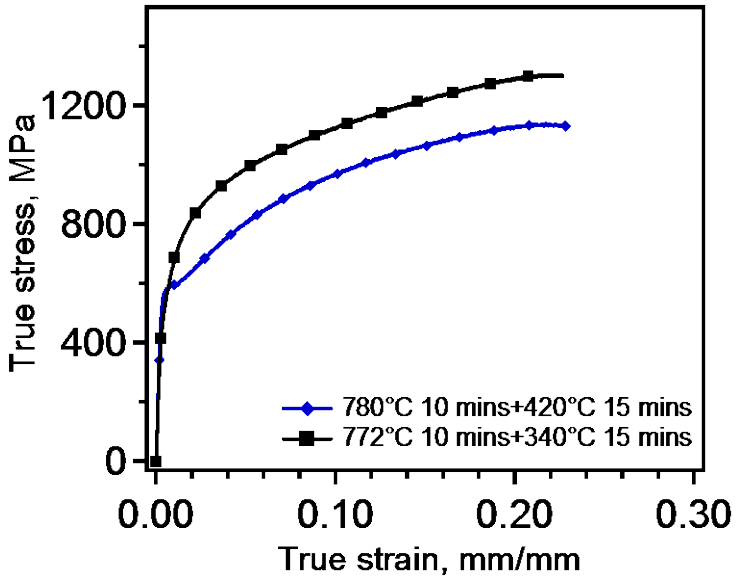

(b)

Figure 28. True stress vs. true strain response of the model TRIP-assisted steel before and after the designed thermo-mechancal processing (a). Comparison of the mechanical performance of samples with the different two-stage heat treatment conditions (b)

Table 5. Summary of the mechanical response of the Fe-1.42Mn-1.56Si-0.32C samples with different mechanical/thermal conditions. The standard deviations are from three to five different experiments

	Yield Strengh (MPa)	True tensile strength (MPa)	True Uniform Strain (%)
As-cast	396±6	786±3	13±1
950 °C ECAE 2 passes	631±3	950±5	18±1
950 °C ECAE 2 passes+780 °C 600 s +420 °C 900 s	585±19	1137±6	23±1
950 °C ECAE 2 passes+772 °C 600 s +340 °C 900 s	567±24	1300±17	23±1

One can argue that the initial hypothesis of maximizing the ferrite content first and then the retained austenite will really lead to a promising mechanical performance for the TRIP-assisted steels. However, it is not conclusive based on current results to validate that the proposed hypothesis could lead to a best phase constitution of TRIP-assisted steel in terms of mechanical performance. In fact, to the best of the authors' knowledge, the contribution of the individual coexisting phases (ferrite, austenite, bainite, and martensite) on the mechanical performance is not clearly known yet. Nevertheless, we aimed at establishing a simple but systematic predictive microstructure design framework through proper selection of process parameters for any given target for the phase fractions that could eventually result in enhanced mechanical performances in TRIP-assisted steels. To validate this, one can refer to the tensile strength-elongation failure data for most popular AHSS [2, 127] shown in Figure 2. The 1st generation AHSS are marked by dashed circle. The 2nd generation AHSS mainly include Twinning-

Induced Plasticity (TWIP) steels, which exhibit excellent strength and ductility combination but are relatively expensive. With the designed heat treatment, the mechanical performance of the model low-alloy TRIP-assisted steel has been successfully improved into a region in the middle of 1st and 2nd generation AHSS, which is rather remarkable for such a low-alloy steel. Further improvement could in principle be achieved by optimizing the alloy composition in the low alloying region as well as the thermo-mechanical treatments, for instance for further refinement of ferrite and increased volume fraction of retained austenite.

CHAPTER VI

DESIGN OF NEW BAINITIC ISOTHERMAL TRANSFORMATION TREATMENT FOR MICROSTRUCTURAL OPTIMIZATION IN CONVENTIONAL TRIP-ASSISTED STEELS

6.1 Multi-step Bainitic Isothermal Transformation

According to the analysis from the Chapter IV, it was found that martensite needs to be suppressed if one wants to maintain a good ductility. However, in Chapter V, it was found that martensite formation is unavoidable through the conventional two-step heat treatment (IA+BIT) based on the equilibrium thermodynamic analysis for the studied alloy with the chemical composition of Fe-1.42Mn-1.56Si-0.32C in wt%. To fully suppress martensite formation, one has to either change the chemical composition of the alloy, or the thermo-mechanical processing method. Without changing the composition of alloy, however, it seems to be not possible to achieve the goal by applying other existing method such as Q&P, because martensite is required for the following carbon partitioning during the Q&P process. Thus, a new thermo-mechanical processing method/route is necessary for the sake of martensite suppression with the current alloy which is otherwise very difficult with conventional methods. Also, this new method should be able to apply for any low alloy steels which cannot suppress martensite with conventional two stage heat treatment.

It was mentioned in Chapter V that a possibly more sophisticate non-isothermal BIT could be the solution to fully suppress martensite. Among non-isothermal treatment, one possibility could be adding another BIT step. If the second BIT temperature is

designed between Ms and Bs (bainite starting temperature) of the austenite obtained from the first BIT, it is expected that carbon could be enriched more sufficiently such that fully suppressing martensite would become possible after the heat treatment. To the authors' knowledge, only few reports have addressed on stepped BIT processing. Papadimitriou *et al* [154] investigated the microstructure (Fe-3.9Si-0.9C in wt%) after two BITs under TEM and demonstrated bainitic ferrite with various thickness due to the stepped BIT at two different temperatures. Hase *et al* [46] applied stepped BIT on bainitic steel (Fe-1.98Mn-1.56Si-1.01Al-1.01Cr-1.51Co-0.79C in wt %) and obtained a bimodal distribution of bainitic ferrite accompanied with enhanced the mechanical property comparing with conventional single BIT.

In this chapter, dual BIT treatment will be applied on a low alloy TRIP-assisted steel (Fe-1.42Mn-1.56Si-0.32C). The purpose is to extend the conventional easy-to-follow two-step treatment in order to suppress martensite formation without additional alloying. In addition, cooling rate between the two BITs was adjusted to reveal its effect on the resulting microstructure and mechanical performance.

6.2 Parameter Design for the Dual Step Baintic Isothermal Transformation Treatment

The intercritical annealing was performed at 772°C for 2hrs for all conditions in this work. The thermodynamic calculation of austenite after IA using ThermoCalc equipped with TCFE6 (version2) database has been performed to design BIT temperatures, shown in Figure 29. The Ms temperature (in red) and the T0 (in blue),

which indicates the theoretical maximum carbon enrichment in austenite due to the bainitic transformation, are plotted as a function of carbon content. The carbon content in austenite after IA is indicated as C_{IA}. The Bs of austenite after IA is indicated by the upper dashed horizontal line. In order to suppression martensite formation, the first BIT temperature should be selected between the M_s and B_s after IA, indicated by the arrows. In this work, 420°C is selected as a model temperature of first BIT and heat treated for 4mins. Assuming the first BIT performed sufficiently (i.e. the carbon content of retained austenite is equal to the value from T0, indicated by C_{1stBIT}), the B_s temperature of retained austenite after first BIT can be further calculated and shown as the dashed horizontal line in the middle of Figure 29. Again, to suppress the martensite formation, the minimum temperature of the second BIT must be higher than Ms, indicated by the dashed horizontal line in the bottom of the figure. Considering that the minimum carbon content required to stabilize austenite at room temperature is $C_{Ms=RT}$, the temperature window of the second BIT is smaller than the gap between B_s and M_s, which is shown by the shaded region. According to the prediction, 250°C was selected to be the model temperature of second BIT and held for 24 hrs considering the slow transformation kinetics.

In addition, two cooling rates were applied between the two BITs (i.e. by furnace cooled or quenching into the molten salt at 250°C). For comparison, additional samples with only first BIT (420°C for 4min) were also prepared.

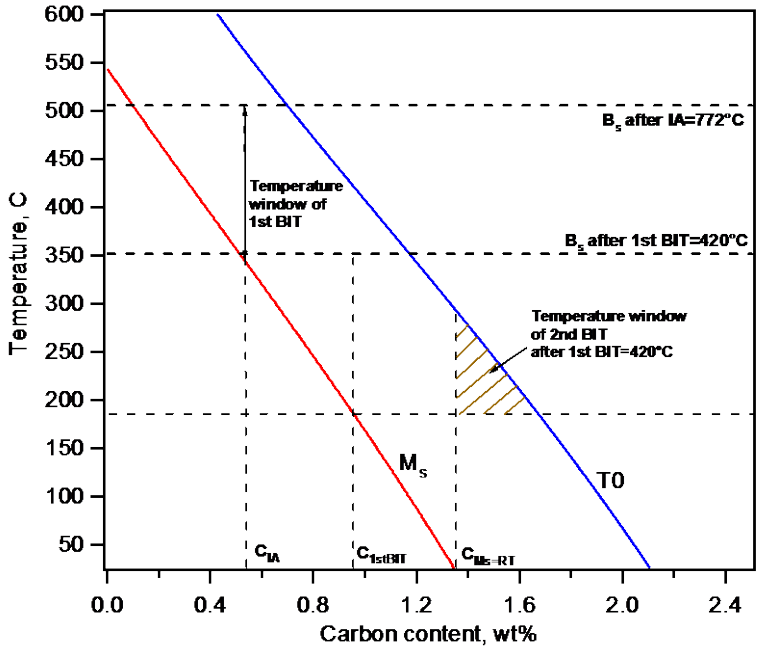

Figure 29. Thermodynamic prediction for BIT using ThemoCalc with TCFE6 (version2) database. The M_s temperature (in red) and T0 (in blue) are presented as a function of BIT temperature. C_{IA} is the carbon content in austenite after IA treatment and $C_{Ms=RT}$ is the carbon content required to stabilize the retained austenite at room temperature. The Bs temperature of austenite after IA and after first BIT (assuming the T_{1stBIT}=420°C) are indicated by horizontal dashed lines. The temperature window of first BIT is shown by the arrows and the second one is indicated by the shaded region (assuming the T_{1stBIT}=420°C)

6.3 Microstructure Evolution with Dual Bainitic Isothermal Transformation Treatment

Figure 30 shows the microstructure evolution at the end of each BIT treatment. After first BIT (420°C, 4min), a multiphase microstructure including ferrite, bainite, austenite and martensite could be obtained at ambient temperature, as pointed out by the arrows in Figure 30a. Austenite exists in the form of both bulky island and thin film which separates the bainitic ferrite. Martensite in this case could not be clearly

distinguished from austenite and coexists with bulky austenite. With two-step BIT treatment, both number and size of the bulky austenite/martensite plates are significantly reduced regardless of cooling rate as shown in Figure 30b and 30c, which indicates the further bainitic transformation during the second BIT treatment. Moreover, the slow cooling between two BITs (Figure 30b) results in more dense ridged bainite than the bainite after one BIT treatment in Figure 30a. Also, the bainite plates are shorter in length and distributed more homogeneously. By contrast, rapid cooling between the two BIT treatments (Figure 30c) leads to longer and neat bainite plates.

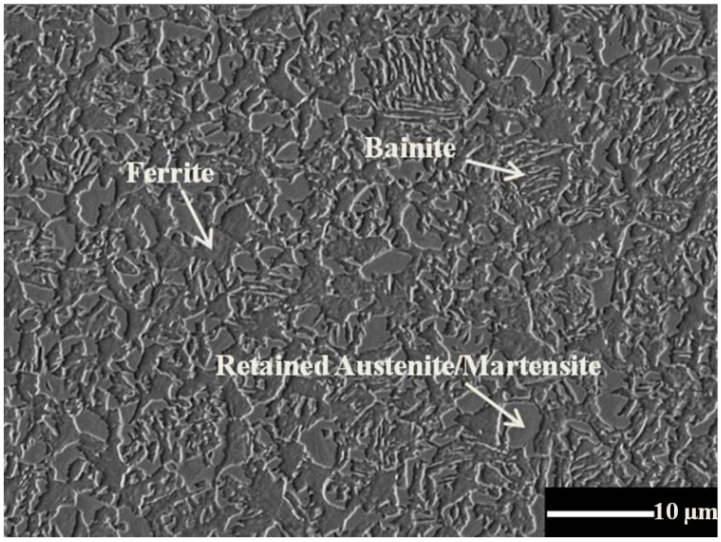

(a)

Figure 30. Scanning electron microscopy image showing the microstructure of the model composition after (a) IA (772°C-2hr)+1 BIT (420°C-4min), (b) IA(772°C-2hr)+2 BIT (420°C-4min+250°C-24hr) with furnace cooling between the two BITs, and (c) IA(772°C-2hr)+2 BIT (420°C-4min+250°C-24hr) with salt quenching between the two BITs. The arrows indicate the coexisting phases

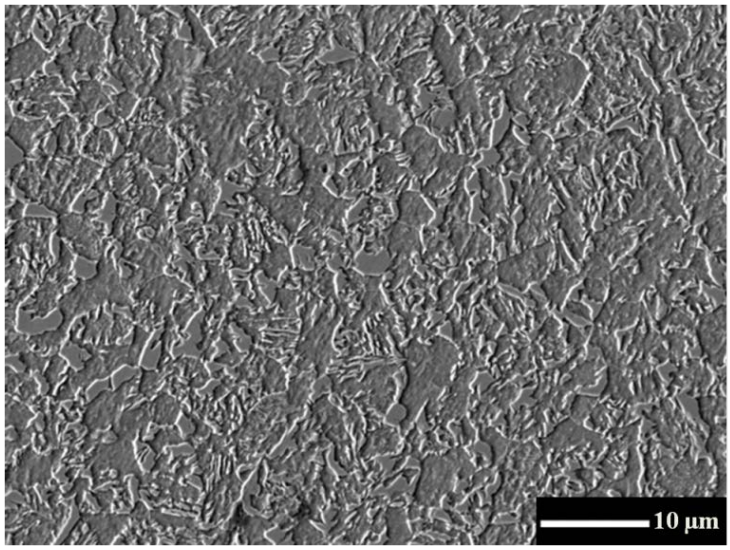

(b)

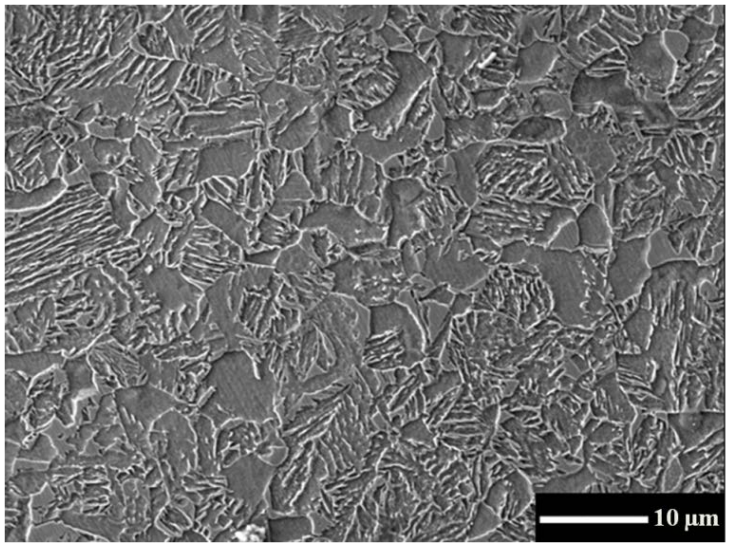

(c)

Figure 30. Continued

Table 6 summarizes the phase constitutions of the microstructures after different heat treatments. With the same intercritical annealing (IA) treatment (i.e.772°C for 2hrs), the ferrite content is expected to be the same (around 42%) assuming the quenching to BIT temperature is fast enough to restrict the formation of additional ferrite. About 18% martensite remains if quenching to ambient temperature right after the first BIT. This number drastically reduced about 6% due to the improved stability of austenite through an additional BIT. Correspondently, the volume fraction of bainitic ferrite of dual BIT treatments is much higher than the single BIT case. Although a clear decrease in the martensite volume fraction has been achieved, it is yet fully suppressed. One reason might be the inhomogeneous distribution of carbon in thin film austenite and blocky austenite [136]. In addition, the volume fraction of retained austenite also decreases with the additional step of BIT due to the reduction of the total volume fraction of austenite at the end of second BIT and before cooling to the room temperature. Moreover, it could be observed that the fast cooling between the two BITs leads to a relatively higher average carbon content and less amount of austenite, which indicates a more sufficient bainitic transformation than the slow cooling condition.

Table 6. The results of the phase constitutions and mechanical response with various heat treatments on the model TRIP-assisted steel composition. Transformed volume fraction of retained austenite until fracture is also summarized. V_A: Volume fraction of austenite

Condition		Volume Fraction, %				Average Carbon in RA from XRD, wt%	Av.Car/ Av.V_A from XRD	Transformed V_A until fracture, %	True uniform strain, %	True tensile strength, MPa	Yield stress, MPa
Intercritial annealing (IA)	Bainitic isothermal transformation (BIT)	Ferrite	Bainite (Bainitic ferrite)	Martensite	Retained Austenite (RA)						
772°C-2hr	420°C-4min	41.2±0.8	22	17.6±3.1	19.2±0.9	1.147	5.98	10.7±2.3	17.7±0.1	1208±7	646±32
772°C-2hr	420°C-4min+250°C-24hr (slow cooling)	41.2±0.8	37.5	6±2.1	15.3±1.2	1.532	9.99	8.7±1.4	24.6±0.3	1150±9	701±41
772°C-2hr	420°C-4min+250°C-24hr (rapid cooling)	41.2±0.8	40.4	5.6±1.8	12.8±0.6	1.565	12.19	6.3±1.4	19.4±3.1	1128±53	750±27

6.4 Mechanical Characterization

The reduction of thermal induced martensite is expected to improve ductility referring to previous studies [155]. The current results find the similar trend as both dual BIT cases (low martensite volume fraction) show better uniform strain than the single BIT one (Table 6). Although the reduction of martensite volume fraction is very similar for the two dual BIT cases, it is observed that various cooling rate between the two BITs leads to different uniform strain. Around 5% difference exists between rapid cooling and slow cooling between two BITs. The austenite volume fraction and stability could be one reason behind. The rapid cooling case has less volume fraction but more stabilized austenite (higher carbon content) than the slow cooling case, which results in a smaller improvement of uniform strain as compared to the slow cooling one. Another reason can be the homogeneity of microstructures after heat treatment, as the slow cooling results in more homogenized distribution of bainite and martensite/austenite islands than the rapid cooling one in Figure 30.

The present author proposed C/V_A (carbon content over the volume fraction of austenite) ratio as a new parameter to evaluate the combined effect of the volume fraction and stability of austenite on uniform strain for the same model composition [155]. It was found that the C/V_A ratio decreases with increasing uniform strain, which is further evidenced in the present study. Comparing the two dual BIT cases with similar volume fraction of martensite and ferrite in Table 6, the higher C/V_A ratio corresponds to worse ductility. The single BIT condition has the minimum C/V_A ratio. However, since the martensite content is much higher, it prevents the material from better ductility. In

addition, the volume fraction of retained austenite after failure has been measured and summarized in Table 6. It can be observed that higher C/V_A ratio results in smaller amount of transformed retained austenite. This indicates that the proposed C/V_A ratio could also be an estimation parameter of transformable retained austenite during plastic deformation.

Figure 31 shows the evolution of strain hardening rate ($d\sigma/d\varepsilon$) as a function of true strain. The single BIT case exhibits an overall higher hardening rate than two dual BIT cases. At the same time, the rapid cooling case shows the lowest hardening rate. Moreover, the single BIT case fails before reaching the plastic instability criteria ($d\sigma/d\varepsilon=\sigma$) due to the large amount of thermal induced martensite in the initial microstructure. For the two dual BIT conditions, by suppressing thermal induced martensite, the fractures were retarded after reaching the plastic instability criterion as indicated by the dash lines. Furthermore, the fact that slow cooling case (black curve) reached the plastic instability at a higher strain level than rapid cooling one can also indicate the later finishing of strain-induced martensitic transformation.

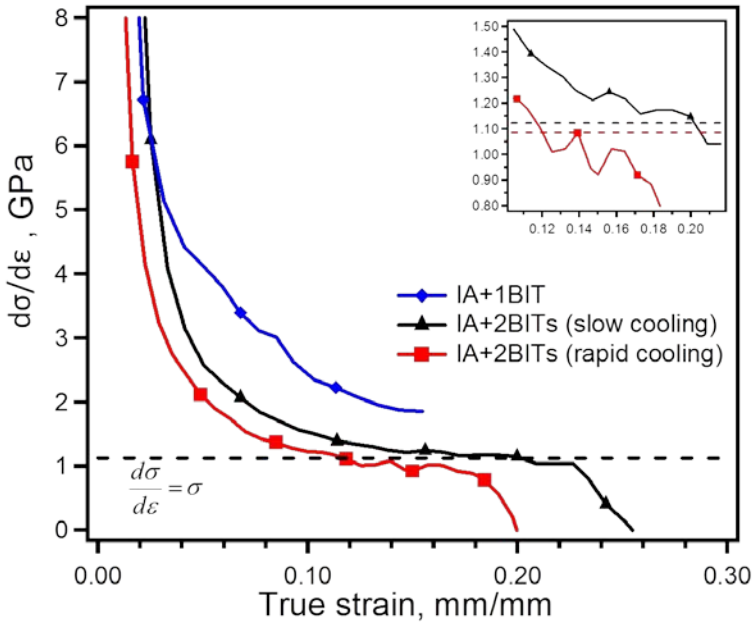

Figure 31. Strain hardening (dσ/dε) as a function of true strain after various heat treatments. The details of the heat treatment conditions can be found in Table 1. The dash line represent the flow stress of plastic instability (dσ/dε=σ) of IA+2BIT cases. The ingot is the magnification of the figure showing the difference of flow stresses at dσ/dε=σ for the two dual BIT cases

CHAPTER VII

MICROSTRUCTURE OPTIMIZATION THROUGH ALLOYING ADDITIONS

7.1 The Modification of Alloy Composition

In Chapter IV and V, it has been shown that, although some phases (i.e. ferrite, austenite) are flavored for a good combination of strength and ductility, the phase constitutions (i.e. the volume fractions of ferrite, bainite, martensite and retained austenite) cannot be arbitrary assigned. For example, one cannot obtain fully ferritic or austenitic microstructure at room temperature for the material discussed in previous chapters by any means. Moreover, the achievable combinations of phase constitutions are constrained for a specific composition. In Chapter VI, we focused on the modification of conventional two-stage heat treatment. With an additional BIT treatment, the achievable combinations of phase constitutions can be expanded. However, the expansion by the modification is also limited. One evidence is that it is not easy to fully suppress the martensite formation, even with the dual BIT treatment. In this chapter, effort will be made on designing and characterizing a new alloy. Considering the design criteria proposed in Chapter V (i.e. maximizing ferrite, and maximizing retained austenite/fully suppressing martensite), the new alloy should in principle be able to easily result in a martensite free microstructure after the conventional two stage heat treatment. (i.e. only ferrite, bainite and retained austenite are coexisting after the heat treatment)

In previous chapters, Fe-1.42Mn-1.56Si-0.32C alloy (nominal composition: Fe-1.5Mn-1.5Si-0.3C in wt%) has been systematically studied. The thermodynamic

calculation (Figure 24) shows that the ideal BIT temperature window for martensite suppression and thus the austenite maximization (yellow region in Figure 20) does not exist for the alloy. In order to have this yellow region, either the Ms curve needs to shift downwards or the T_0' needs to shift to the right. Comparing the two options, it is much easier to change Ms curve as both empirical relations or theoretical calculations have already been reported in the past [30, 32, 73, 156-159]. Thus, we will focus on the adjustment of Ms curve here through alloying addition. Note that it is entirely possible that the T_0' also moves as the chemical composition changes. Such effect is, however, is beyond the scope of the discussion here.

According to the empirical relations in the past [30, 32, 159], most alloying elements are beneficial to reduce Ms temperature expect Al and Co. Among these, C, Mn, Ni and Mo are very effective for decreasing Ms temperature. In order to further adjust the alloying addition on the base alloy (i.e. Fe-1.5Mn-1.5Si-0.3C), several criteria were proposed: weldability, galvanization, cost, and no carbide formation.

Weldability has been one of the main challenges for the application of TRIP steels. The problem originates from the high carbon content in the retained austenite in the TRIP steels. Although the retained austenite can provide extra strain hardening upon deformation, it tends to decompose at warm or high temperature into ferrite and carbides, which results in very different mechanical properties in the heat affected zone (HAZ) or fusion zone (FZ) or in the matrix [160]. More importantly, high carbon content (i.e. higher than 0.4% in wt% [159]) tends to form martensite in the FZ after welding, thus reduces the capability of energy absorption under high strain rate deformation and

can possibly leads to interfacial fracture [160]. As a result, although C is the most effective element to reduce Ms temperature, the C content will not be adjusted here.

Galvanization is another constrain of the material design, considering that the main application of the TRIP steel is in the automotive industry. Si is known to effectively prevent cementite formation during thermo processing, and thus beneficial for austenite stabilization [9, 159]. On the other hand, Si is undesired element for galvanization [127]. Although Al and P have been proposed as the substitutions [33, 35, 161], Al can cause casting problem and improves the kinetics for martensite formation, while P is known to cause grain boundary segregation [162, 163]. In the present case, the Al and P will not be added. At the same time, the base alloy contains 1.5% Si, which is too high for good galvanization and requires to be reduced.

Cost is always an issue for material design or selection. The future AHSS requires both cost effective and high performance (i.e. strength and ductility). For the sake of that, low alloying addition is usually required. (i.e. the total alloying addition should be controlled below 4%). In addition, some expensive alloying additions need to be avoided, such as Ni and Cr.

Finally, carbide formation is another concern in the current alloying design. Although Si has been included in the base alloy to prevent cementite formation, other alloying carbides would form during IA treatment if some strong carbide-forming elements (i.e. Ti, Nb, V, Mo, W, Ta, Hf, Zr, Cr) are present in the alloy. Several reports have addressed on the effect of some strong carbide-forming elements on the microstructure and mechanical performance of advanced high strength steels [22, 34, 62,

164]. It has been revealed that only a slight amount of the alloying addition (e.g. 0.035% in wt% for Nb) is required to form carbide precipitates after the conventional two-stage heat treatment. These alloying precipitates (e.g. NbC, TiC, MoC) are with the size of nano-scale (tens of nm) and can result in precipitation hardening during plastic deformation. However, since these carbides can consume carbon as well, the maximum carbon enrichment in retained austenite will thus be reduced and less austenite can be retained. In the present work, our goal is to reduce the Ms temperature and to suppress martensite formation. Thus, we would like to avoid these strong carbide-forming elements and reduce the complexity of the microstructure although they might be beneficial for the mechanical properties.

Considering all the aforementioned constrains, the most straightforward method which can stabilize more austenite while suppressing martensite is, to increase the Mn content. Mn is known as austenite stabilizer and solution strengthener. At the same time, it does not form carbide easily and cheaper than Cr or Ni. Although it contributes to a higher carbon equivalent (negative for weldability), the effect is much slighter than carbon. In recent years, medium Mn contained alloying steels (3~9% in wt%) have attracted some effort [29, 51, 165-168]. The increase of Mn content is reported to provide better austenite stability, together with a much refined grain size. In this study, we doubled the Mn content to 3% in wt%, and reduced the Si content to 1% in wt% to improve the galvanization property as compared with the base alloy (Fe-1.5Mn-1.5Si-0.3C). The carbon was remained to be 0.3% in wt%. The actually chemical composition of the as-cast has shown in Table 1.

7.2 Design of Intercritical Annealing

The design criteria for the new alloy are the same as those in Chapter 5: maximizing ferrite and maximizing austenite (suppressing martensite). For intercritical annealing, the goal is to maximize the volume fraction of ferrite and avoid cementite formation. After the same initial processing through ECAP (i.e route 2C, 950°C), the samples were cut in dog-bone shape with the dimension of 25mm x 8mm x 1mm. To determine the best condition of the intercritical annealing, samples were heat treated at various temperatures (i.e. 660°C to 740°C) for 10 min, 30 min and 2hrs. These temperatures were selected based on the phase diagram calculated using Thermo-Calc®, equipped with TCFE database, version 6.2. The calculated volume fraction of ferrite and cementite as a function of temperature, together with the volume fractions of ferrite after different heat treatment, is shown in Figure 32.

The predicted volume fraction of ferrite decreases with increasing IA temperature. Two segments appear in the prediction (red curve). The inflection point is the indicator of the disappearance of cementite. The experimental results show the same trend as the prediction, decreasing from about 45% (660°C) to 15% (740°C). With same IA temperature, the volume fraction of ferrite decreases as the holding time is longer due to the propagation of austenite. However, discrepancy can be observed between the prediction and experimental results. First, the predicted volume fractions of ferrite are much higher than the determined ones. Second, no cementite can be found for all examined cases, although it is suggested from the prediction that cementite should show up if the IA temperature is lower than 700°C.

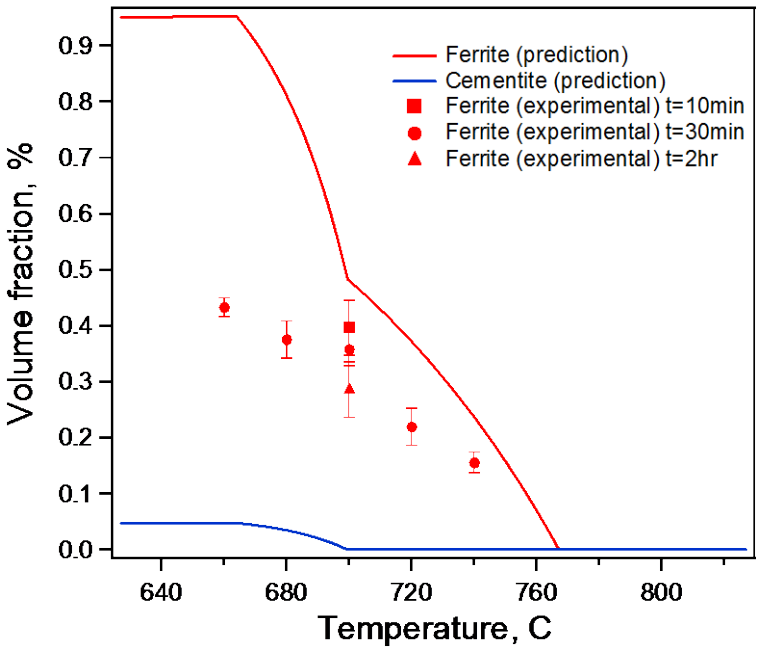

Figure 32. Calculated volume fraction of ferrite and cementite as a function of temperature (solid lines) and the experimentally determined volume fractions of ferrite (markers)

The reason of the above discrepencies can possibly be explained by the microstructure evolution. Figure 33 shows the SEM images for samples after different IA treatments. Ferrite (dark)-martensite (bright) dual phase can be distinguished from each other after etching. Figure 33a and 33b have the IA time (30 min), but different IA temperatures (660°C, 720°C, respectively). Figure 33c was heat treated at 700°C for 10min. Regardless of the temperature and time for IA, a common feature for the microstructures is the segregation of austenite phase. Clusters of martensite (prior

austenite) can be seen in all these microstructures, which is not observed for the previous base alloy (Figure 14).

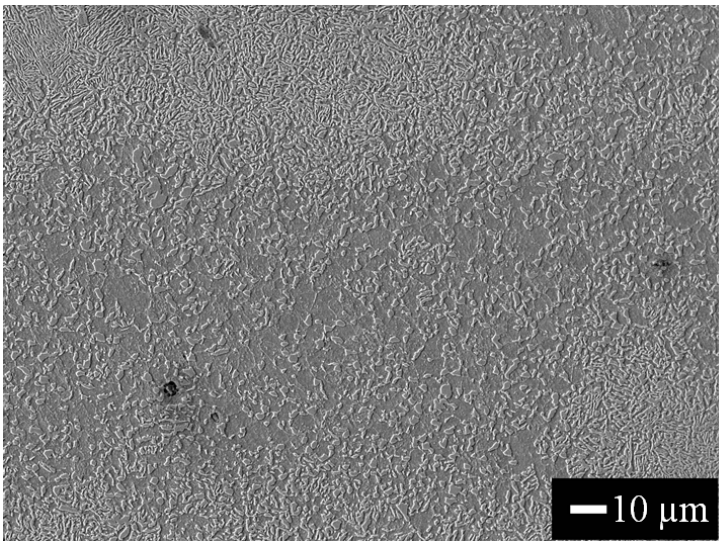

(a)

Figure 33. Scanning electron microscopy images showing the ferrite-martensite microstructure after IA treatment at (a) 660°C 30min, (b) 720°C 30min, and (c) 700°C 10min for Fe-2.65Mn-0.95Si-0.32C. The samples were etched using 2% Nital

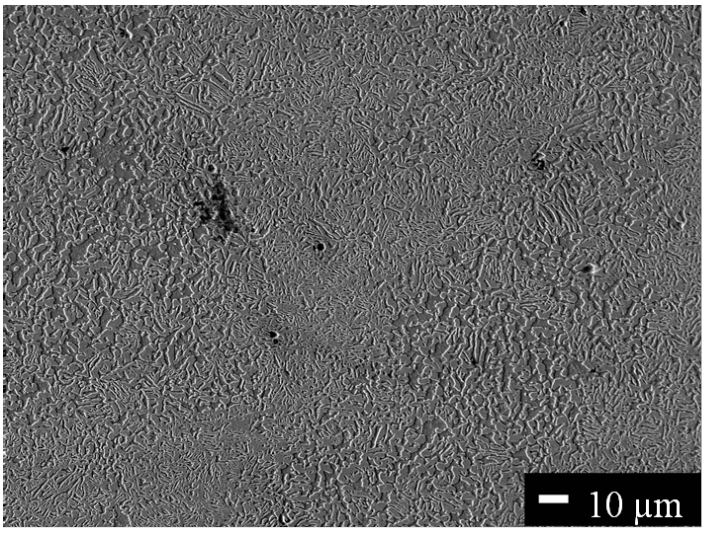

(b)

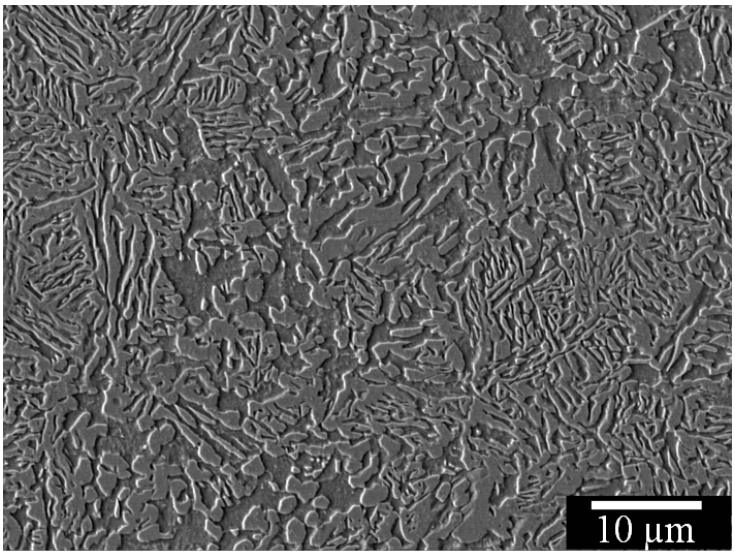

(c)

Figure 33. Continued

Such martensite (prior austenite) aggregation is probably due to the increase of Mn content which makes the as-cast material more difficult to homogenize. In other words, the initial processing (i.e. ECAP at 950°C) is insufficient to homogenize the microstructure. Figure 34 shows the microstructure after initial processing (i.e. ECAP at 950°C, route 2C) for the new alloy. A mixture of ferrite (black), pearlite (bright lamellars) and martensite/austenite islands (bright) can be observed, as indicated by the arrows. The aggregation of pearlite/martensite/austenite phases is also found, which is similar as that in Figure 33. Thus, the aggregation of martensite (prior austenite) after IA treatment is indeed due to the inhomogenity after initial processing. Modification of the initial processing is required.

The microstructure inhomogenity is known to be undesired to the mechanical properties. Thus an additional solutionizing heat treatment was performed at 1000°C for 1hr followed by water quenching after high temperature ECAP. Figure 35 shows the as quenched microstructure which Martensite is the dominating phase. No clusters can be observed after the additional treatment. Thus, it is believed that the additional heat treatment is sufficient to homogenize the microstructure.

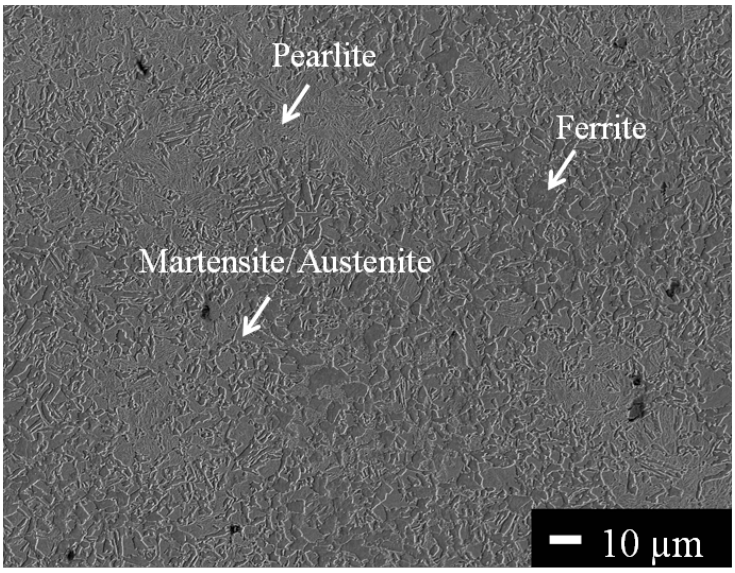

Figure 34. Scanning electron microscopy image of Fe-2.65Mn-0.95Si-0.32C after initial processing at 950°C, route 2C

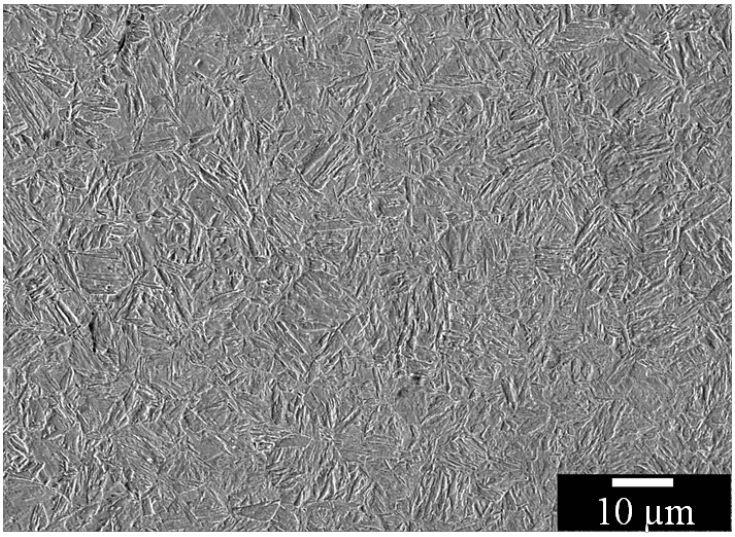

Figure 35. Scanning electron microscopy image of Fe-2.65Mn-0.95Si-0.32C after initial processing at 950°C, route 2C, and an additional heat treatment at 1000°C for 1hr followed by water quenching

Figure 36 summarized the volume fraction of ferrite as a function of different IA conditions after the previous homogenization (i.e. 1000°C 1hr). With same time for IA (i.e. 30min), the volume fraction of ferrite reaches maximum at 700°C. At IA=700°C, the ferrite content decreases as the time holding is longer (from 5min to 30min). Comparing to the results without homogenization in Figure 32, the volume fraction of ferrite increases for same IA conditions and is closer to the thermodynamic predictions. Cememtite appears after 680°C for 30min treatment, as predicted by the thermodynamic calculation. At 700°C, cememtite dissolves when heat treated for longer than 5 min, probably because of the slow heating rate in the furnace. Since maximizing ferrite and avoiding cementite is the goal, the optimized IA condition is selected to be 700°C 10min.

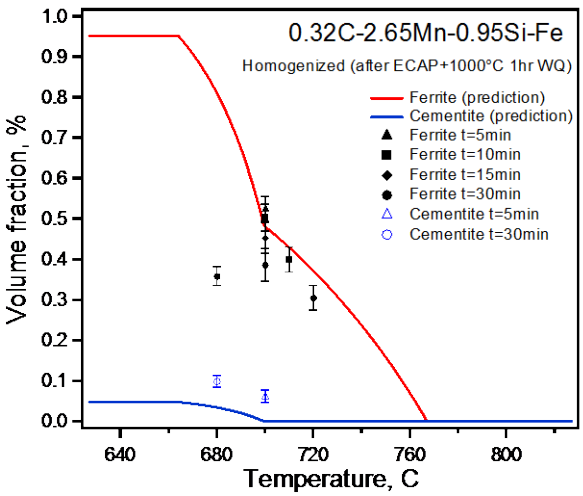

Figure 36. Calculated volume fraction of ferrite and cementite as a function of temperature (solid lines) and the experimentally determined volume fractions of ferrite (markers) after the additional homogenization heat treatment at 1000°C for 1hr

7.3 Design of Bainitic Isothermal Transformation

Analogy to the previous alloy, the heat treatment parameter for BIT was determined based on the criterion of suppressing martensite formation. Figure 37 shows the calculated thermodynamic phase diagram of the alloy for BIT. M_s temperature and T_0 curve were calculated as a function of carbon in retained austenite. Compared with the previous alloy (Figure 24), the increase in Mn content shifts the M_s temperature to lower level as expect, while the position of T_0 curve only have a slight change. As indicated by the vertical dashed line, the initial carbon content in austenite before BIT (after IA) is estimated to be around 0.6%, considering that the optimized parameter determined in the previous section is applied for IA. With this carbon content, the temperature range of suppressing martensite formation before BIT is from about 250°C to 460°C, as marked by the double-side arrow. On the other hand, the maximum BIT temperature to suppress martensite formation at room temperature after BIT treatment is about 280°C (also marked by the arrow). The intersecting temperature range (250°C to 280°C) can be obtained which should theoretically suppress the martensite formation (indicated in the Figure). This finding indicates that the optimization of chemical composition is indeed effective to suppress martensite, since such temperature window does not exist for the previous alloy (0.3C-1.5Mn-1.5Si-Fe).

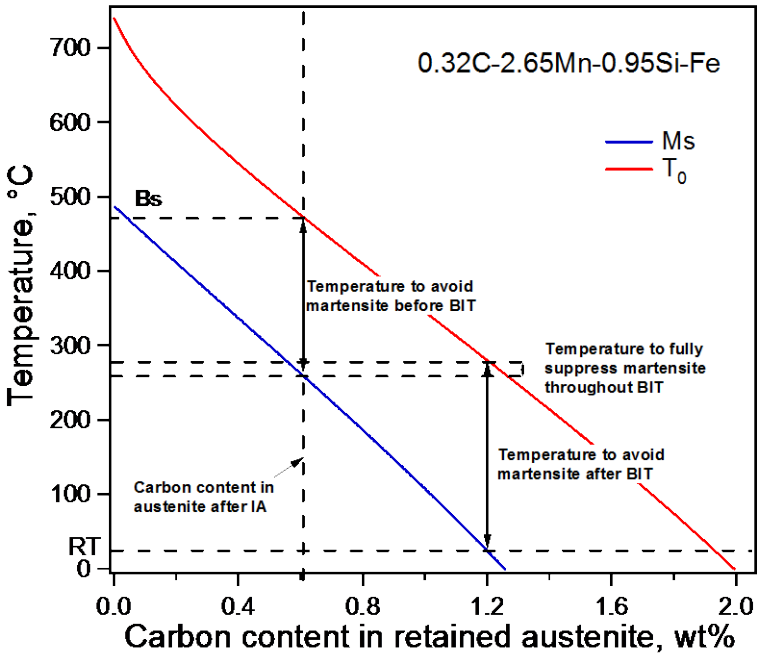

Figure 37. Calculated thermodynamic phase diagram for BIT heat treatment of 0.32C-2.65Mn-0.95Si-Fe alloy

Experiments were performed to validate the prediction from thermodynamic calculations. The samples after IA (treated at 700°C for 10 min) were further quenched in molten salt at 275°C and held for time varying from 10 min to 5 days. The phase constitutions were calculated using the same method as in previous chapters and the results are summarized in Table 7. Unexpectedly, martensite still exists for all time period. The volume fraction of martensite first decreases from 31.6% (10 min case) to 14.5% (70 min) and bounces back to about 20~26% after heat treated for 1-5 days.

On the contrary, the volume fraction of retained austenite first increases to about 20% and then drops to 10% for BIT longer than 1 day. The thermal induced martensite here can form either before or after the BIT. The initial increase of the volume fraction of retained austenite, and decrease in the volume fraction of martensite (till BIT=70 min) indicates that at least part of the martensite is formed after BIT due to the interruption of bainitic transformation. Moreover, the volume fractions of retained austenite drop after BIT for longer than 70 min, which indicates that 70 min should be sufficient for the completion of bainitic transformation. Furthermore, since the carbon content in retained austenite was determined to be around 1.3 wt% after BIT for 70 min, theoretically no martensite form after BIT in this case (refer to Figure 36). In other words, the measured martenite in condition 4 (BIT=70min case) should form before BIT in this case, which indicates that the thermodynamic prediction of M_s temperature for this alloy is not accurate enough.

To find out the real M_s temperature after the designed IA treatment, the stepped BIT method which was introduced in the previous chapter was applied. In this case, the second BIT condition is set at 275°C for 70 min to suppress martensite formation after BIT, whereas the first BIT temperature is raised to 325°C and 350°C (condition 7 and 8, respectively). About 10% martensite is found in the 325°C case and only negligible amount of martensite is found in the 350°C case (3.6%), which indicates that the real Ms temperature after IA should be in the range between 325°C and 350°C. Since a single BIT at 350°C could not fully suppress the martensite formation as indicated in condition 9 due to the insufficient carbon enrichment in austenite through BIT, the BIT

temperature is further adjusted down to 340°C (condition 10). Less than 5% is calculated based on the obtained microstructure in this case and the martensite free structure was successfully obtained after BIT at 340°C and 20 min.

Table 7. Calculated phase constitutions after different heat treatment conditions for 0.32C-2.65Mn-0.95Si-Fe

Condition	IA	BIT	Volume Fraction			
			Ferrite	Bainitic ferrite	Martensite	Retained Austenite (RA)
1	700°C 10min	275°C 10min	50.3%	6.0%	31.6%	12.1%
2	700°C 10min	275°C 15min	50.3%	6.7%	26.3%	16.7%
3	700°C 10min	275°C 20min	50.3%	7.2%	20.7%	21.8%
4	700°C 10min	275°C 70min	50.3%	14.3%	14.5%	21.0%
5	700°C 10min	275°C 1day	50.3%	17.3%	21.6%	10.8%
6	700°C 10min	275°C 5days	50.3%	12.3%	26.6%	10.8%
7	700°C 10min	325°C 25min+275°C 70min	50.3%	24.2%	10.2%	14.9%
8	700°C 10min	350°C 16min+275°C 70min	50.3%	27.7%	3.6%	18.4%
9	700°C 10min	350°C 16min	50.3%	27.9%	9.2%	12.6%
10	700°C 10min	340°C 20min	50.3%	27.8%	3.8%	18.1%

7.4 Resulting Mechanical Response

Figure 37 shows the some mechanical behaviors of the alloy before and after the microstructure design. The red curve is the performance after initial high temperature ECAE (950°C 2 passes with route C). The blue one represents for the martensite free

microstructure after heat treated with designed parameters (condition 10 in Table 7). Obviously, the multiphase microstructure after two-step heat treatment provides a much more enhanced ductility (~24%) than the initial ferrite-pearlite microstructure (~8%) without the ultimate tensile strength is not sacrificed.

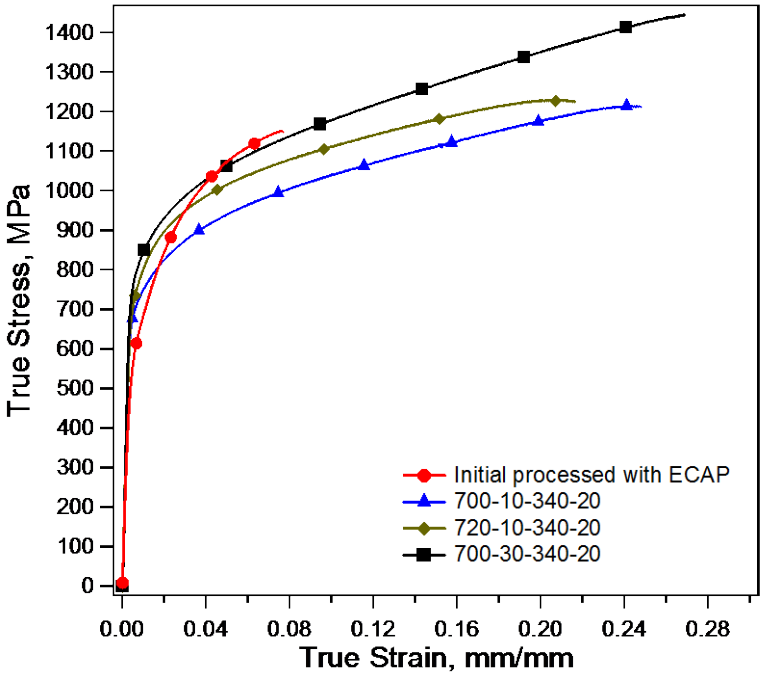

Figure 38. Mechanical performance of Fe-2.65Mn-0.95Si-0.32C after selected thermo-mechanical treatments

To emphasize the positive effect on the ductility with martensite free structure, two other heat treatment are performed in which the ferrite content (soft phase) are

lower. The mechanical performances of these conditions are also shown in Figure 37 (the yellow and the black curve). Both the yellow one (IA: 720°C 10min, BIT: 340°C 20 min) and the black one (IA: 700°C 30min, BIT: 340°C 20 min) contain less ferrite (~10% less, summarized in Table 8), but more bainitic ferrite than the blue one (IA: 700°C 10min, BIT: 340°C 20 min). At the same time, the volume fractions of retained austenite for the three cases are close to each other. The black one contains a slightly more retained austenite (about 1%) than the other two conditions. All the three cases contain negligible amount of martensite and the achieved ductility are all consistently good and better than the level reached from the previous alloy (Fe-1.5Mn-1.5Si-0.3C) in which martensite is unavoidable.

Table 8. Comparison of microstructure and mechanical performance of two selected conditions of 0.32C-2.65Mn-0.95Si-Fe

IA	BIT	Volume Fraction					True Uniform Strain, %	True Tensile strength, MPa	Yield stress, MPa
		Ferrite	Bainitic ferrite	Martensite	Retained Austenite (RA)	C/V_A			
700°C 10min	340°C 20min	50.3±3%	27.8%	3.8%	18.1±2%	7.4	23.6±1.1	1218±8	718±13
700°C 30min	340°C 20min	40±3.8%	41.3%	~0	18.7±3.5%	7.2	26.3±0.7	1400±53	765±48
720°C 10min	340°C 20min	42.4±0.6%	40.2%	~0	17.4±1.3%	7.9	19.7±1.3	1179±38	709±41

One question remained from the previous work in Chapter IV is whether the volume fraction of ferrite or retained austenite is more influential to the ductility of the multiphase TRIP-assisted steels. In this work, some hints could be found based on the results from Table 8. In the absence of martensite, ferrite is as influential as retained austenite. By substitute ferrite with bainitic ferrite (mostly), the ductility can either increase (case 2 in Table 8) or decrease (case 3). On the other hand, only small amount of increase in retained austenite results in a clear improvement in the ductility. In addition, the proposed C/V_A ratio is also valid with the current results. The smallest C/V_A ratio corresponds to the best ductility (~26%) among the three cases. However, it needs to be note that these findings are not very conclusive as the variation of the austenite volume fraction is too large as compared to the difference between different cases. Some other reasons might also exist which requires further experimental examinations.

CHAPTER VIII

MICROSTRUCTURE-BASED MODELING OF THE MECHANICAL BEHAVIOR OF LOW ALLOY TRIP-ASSISTED STEELS

8.1 Introduction

In the previous chapters, we have revealed the phase constitution effect on the room temperature mechanical behavior of the multiphase TRIP-assisted steels, proposed microstructure design criteria to optimize the strength and ductility of a model material, and modified the microstructure based on the designed criteria through both thermo-mechanical processing and alloying addition. With the enormous data generated on the alloy investigated here, one question naturally raised is whether a modeling framework can be developed to predict the mechanical behavior of these multiphase materials, such that the multiphase structure and heat treatment parameters could be designed for a specific requirement of mechanical behavior without significant experimental work. To answer this question, the modeling of the stress-strain response will be attempted in this chapter through a simple modeling framework. Two different low allow TRIP steels (Fe-1.42Mn-1.56Si-0.32C and Fe-2.65Mn-0.95Si-0.32C) will be utilized to validate the model. The goal here is not to develop a very detailed model by considering all the details in the microstructure capturing all the microstructure interactions in the multiphase microstructure, but to come up with reasonably accurate, predictive semi-empirical constitutive relations and models such that the main trend in the role of different phase constitutions on the strength-ductility combination can be predicted in a reasonable accuracy.

The modeling of stress-strain behavior of multiphase steels has been ongoing for over hundred years. Yet the most widely used method is perhaps still semi-empirical based, such as Holloman type models [169]. The modeling of the stress-strain relations in TRIP-assisted steels has been performed using either analytical or numerical methods using classical plasticity or crystal plasticity theory [117-120]. Here, a microstructure-based semi empirical model will be presented which is based on the well-recognized Mecking-Kocks model (for non-transforming phases) and the Olson-Cohen model (for stress/strain-induced martensitic transformation). Experimental determined microstructural features of the individual phases (i.e. grain size, volume fractions, composition) will be utilized as the inputs to the model.

8.2 Description of the Model

In the present work, the macroscopic stress-strain relation of the multiphase microstructure is established by mixing the mechanical performances of individual phases in the microstructure. Figure 38 shows the general framework of the present model. The rule of mixtures is applied for stress,

$$\sigma_{macro} = \sigma_f V_f + \sigma_b V_b + \sigma_A V_A + \sigma_M V_M \quad (4)$$

$$V_f + V_b + V_A + V_M = 1 \quad (5)$$

Where σ_f, ε_f, V_f, σ_b, ε_b, V_b, σ_A, ε_A, V_A, σ_M, ε_M, V_M refer to the flow stress, strain and volume fractions of ferrite (f), bainite (b), blocky retained austenite (A) and thermally induced martensite (M) after the thermal processing (e.g. the conventional two-step heat

treatment). Note that the calculated volume fraction of retained austenite from X-ray is further classified into two parts: blocky retained austenite and thin filmed austenite. The V_A in equations 4-5 refers to the blocky retained austenite which shows transformation during plastic deformation. On the other hand, the thin film austenite is regarded as part of bainite (in between the bainitic ferrite), which is assumed not transforming during deformation since the thickness of the austenite films are usually very small (e.g. sub micron size) [41].

In addition, an Iso-Work assumption [117, 118] has been utilized to describe the strain partitioning among the different phases during plastic deformation, in which

$$\sigma_f d\varepsilon_f = \sigma_b d\varepsilon_b = \sigma_A d\varepsilon_A = \sigma_M d\varepsilon_M \tag{6}$$

Considering the energy conservation of the system,

$$\sigma_{macro} d\varepsilon_{macro} = V_f \sigma_f d\varepsilon_f + V_b \sigma_b d\varepsilon_b + V_A \sigma_A d\varepsilon_A + V_M \sigma_M d\varepsilon_M \tag{7}$$

Placing equations 5 and 6 in equation 7, it is found,

$$\sigma_{macro} d\varepsilon_{macro} = \sigma_f d\varepsilon_f = \sigma_b d\varepsilon_b = \sigma_A d\varepsilon_A = \sigma_M d\varepsilon_M \tag{8}$$

In the next section, the details of the model for each phase will be introduced.

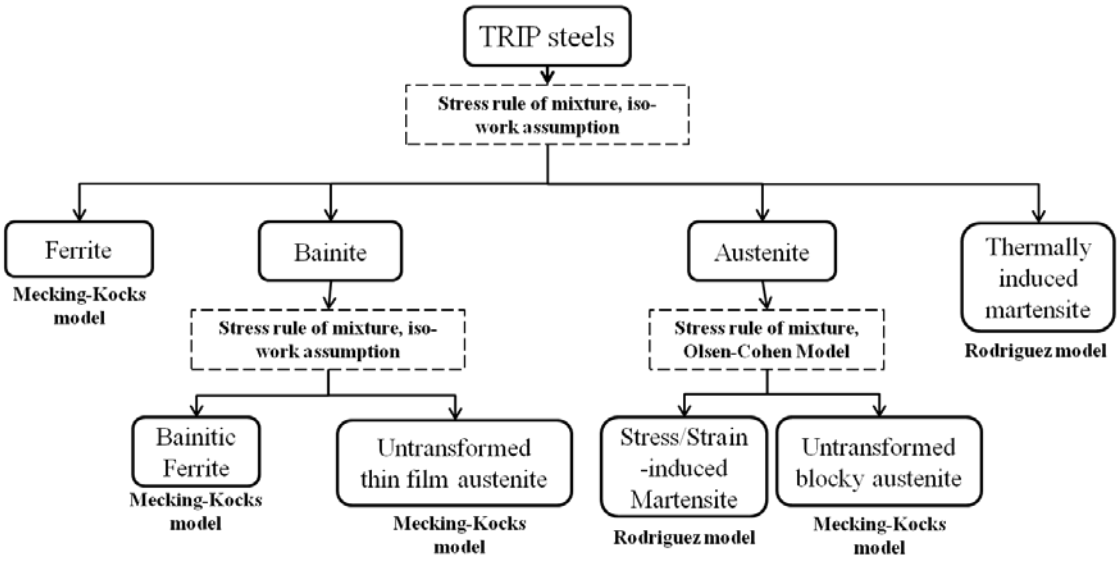

Figure 39. The framework of the present model to simulate the stress-strain behavior of low alloy TRIP-assisted steels with multiphase structures

8.2.1The Modeling of Ferrite Phase

According to Mecking and Kocks [125], the shear stress is usually a function of dislocation density, strain rate and temperature. In the present work, we are only predicting the mechanical performance under quasi-static conditions and at ambient temperature. Consequently, the problem is simplified to be rate and temperature independent. Then, according to the Mecking-Kocks theory [125, 126], the flow stress of a polycrystalline metal can be expressed as,

$$\sigma = \sigma_0 + \alpha MGb\sqrt{\rho} \tag{9}$$

where σ_0 is the stress component due to the lattice resistance, solution hardening and grain size effect. α is a constant of order unity, G is the shear modulus, M is the Taylor

factor, b is Burgers vector and ρ is the dislocation density. The σ_0 can be further determined using the Hall-Patch relation in which,

$$\sigma_0 = \sigma_{0'} + \frac{k}{\sqrt{d}} \tag{10}$$

where k is a materials constant and d is the grain size. $\sigma_{0'}$ describes the effect of lattice resistance and solution hardening, which can be estimated as [170, 171],

$$\sigma_{0'} = \sigma_{Fe} + (77.8 + 0.8 \times Mn\ (wt\%) + 0.6 \times Si(wt\%)) \text{ for BCC phase} \tag{11}$$

$$\text{or} \quad \sigma_{0'} = \sigma_{Fe} + 15.4 \times (4.4 + 23 \times C(wt\%) + 1.3 \times Si(wt\%)) \text{ for FCC phase} \tag{12}$$

where σ_{Fe} is the yield stress of pure iron and equals to 100 MPa.

The evolution of dislocation density as a function of plastic strain can be expressed in two parts [125, 172],

$$\frac{d\rho}{d\varepsilon} = (\frac{d\rho}{d\varepsilon})_{increase} + (\frac{d\rho}{d\varepsilon})_{recover} \tag{13}$$

where the first term in the right hand side is the accumulated dislocation due to plastic deformation and the second term represents dislocation annihilation. The accumulated dislocation density can be estimated using [117, 118, 125],

$$(\frac{d\rho}{d\varepsilon})_{increase} = \sum_i \frac{1}{\theta_i b} \tag{14}$$

where θ is the average mean free path of dislocations. If the glide is the main dislocation activity, equation 14 can further be expressed as,

$$\sum \frac{1}{\theta b} = \frac{1}{b}(\frac{1}{d} + a\sqrt{\rho}) \tag{15}$$

where a is a materials constant. The first term considers the effect of grain boundaries on the average mean free path of dislocation and the second term includes the effect of the distances of dislocations [118].

The recovered dislocation density during plastic deformation can be simplified as,

$$(\frac{d\rho}{d\varepsilon})_{recover} = -h\rho \tag{16}$$

where h is a constant for quasi-static deformation at constant temperatures. Reorganizing equations 13 through 16, the following can be obtained to describe the relation between dislocation density and flow strain,

$$\frac{d\rho}{Md\varepsilon} = \frac{1}{db} + \frac{a}{b}\sqrt{\rho} - h\rho \tag{17}$$

The Taylor factor is added here to convert the crystal shear strain level to the direction of applied stress. Through equations 9-11 and 17, the constitutive equation of ferrite can be established and applied to simulate the flow stress-strain behavior.

8.2.2 Modeling of Bainite Phase

Bainite is treated as a composite consisting of bainitic ferrite and thin film austenite. Stress rule of mixture is applied together with the iso-work assumption mentioned above (equation 5-7). Assuming the austenite does not transform during plastic deformation, the flow stress-strain relations for bainitic ferrite and thin film austenite can be estimated using the same method as the one of ferrite. Consider both bainitic ferrite and thin film austenite possess the lath morphology, equation 10 is modified according to Bhadeshia *et al* [173] for the two components due to the small thickness of the plate (in the order of tens nanometers),

$$\sigma_0 = \sigma_0' + \frac{k}{d} \tag{18}$$

where d is the thickness of individual bainitic ferrite or thin film austenite, and k is a materials constant. σ_0' for bainitic ferrite and thin film austenite could be calculated using equation 11 and 12, respectively.

8.2.3 Modeling of Blocky Austenite Phase

The blocky austenite exhibits strain-induced martensitic transformation. The initial flow stress of blocky austenite is determined using equations 10 and 12. As the material is further deformed plastically, the total flow stress is estimated by the mixture of strain-induced martensite and untransformed austenite, using the Gladman type equation [174],

$$\sigma_A = \sigma_\gamma(1 - f_\alpha^2) + \sigma_\alpha f_\alpha^2 \tag{19}$$

where σ_γ and σ_α are the flow stresses of the untransformed blocky austenite and strain-induced martensite, respectively. f_α is the volume fraction of strain induced martensite.

The flow stress of untransformed blocky austenite can be calculated using equations 9, 10, 12 and 17, while the flow stress of strain induced martensite can be found through the formula from Rodriguez *et al* [170],

$$\sigma = \sigma_0 + \alpha MG\sqrt{b}\sqrt{\frac{1-\exp(-Mh\varepsilon)}{hd}} \tag{20}$$

where d is the grain size of martensite and h is the materials constant same as in equation 16. The σ_0 of martensite here can further be expressed referring to Krauss [175], as:

$$\sigma_0(MPa) = 413 + 1.72 \times 10^3 \times (wt\%\ C)^{0.5} \quad (21)$$

Due to the martensitic transformation, the grain size of both blocky austenite and strain induced martensite should change as the phase transformation is ongoing, which needs to be included when using equations 9, 10, 12 and 17 for the blocky austenite and equation 20 for martensite. Assuming both the blocky austenite and the strain induced martensite are spherical and the total volume of the two phases is conservative, the grain sizes of the blocky austenite and strain induced martensite can be estimated as follows, respectively,

$$d_\gamma = d_{initial}\sqrt[3]{1 - f_\alpha} \quad (22)$$

$$d_\alpha = d_{initial}\sqrt[3]{f_\alpha} \quad (23)$$

where $d_{initial}$ is the initial grain size of the blocky retained austenite.

The volume fraction of the strain-induced martensite is evaluated using the formula by Olson and Cohen [7, 122],

$$f_\alpha = 1 - \exp(-\beta[1 - \exp(-\theta\varepsilon)]^2) \quad (24)$$

where β and θ are material constants and depend on the chemical composition of the alloy. A detailed calculation of the two constant can be found as [122]:

$$\beta = A_2^\beta + \frac{A_1^\beta - A_2^\beta}{1+\exp(\frac{T-T^\beta}{\Delta T^\beta})} \quad (25)$$

$$\theta = A_2^\theta + \frac{A_1^\theta - A_2^\theta}{1+\exp(\frac{T-T^\theta}{\Delta T^\theta})} \quad (26)$$

where T is the temperature of deformation. A_1^{β}, A_2^{β}, A_1^{θ}, T^{θ}, and ΔT^{θ} can be calculated according to the empirical relations [122] providing the chemical composition of the retained austenite, and the rest are fitting parameters as shown in Table 9.

Table 9. Empirical relations and fitting parameters for the constants in Olson-Cohen model (equation 24)

β	A_1^{β}	6.1+5×C(wt%)+11.1×Mn(wt%)+8.8×Si(wt%)-12.6×Al(wt%)
	A_2^{β}	-0.9+1.6×C(wt%)-5.8×Mn(wt%)+13.7×Si(wt%)+5.5×Al(wt%)
	T^{β}	16
	ΔT^{β}	10
θ	A_1^{θ}	0.47+0.03×C(wt%)- 0.02×Mn(wt%)+1.33×Si(wt%)+0.54×Al(wt%)
	A_2^{θ}	0.5
	T^{θ}	38.3+3×C(wt%)+113.1×Mn(wt%)-127.7×Si(wt%)-99.5×Al(wt%)
	ΔT^{θ}	-1.2+4.4×C(wt%)-9.8×Mn(wt%)+28.1×Si(wt%)+8.7×Al(wt%)

8.2.4 Modeling of Thermally Induced Martensite

For microstructures containing thermally induced martensite, the flow behavior of the martensite phase is calculated using equation 20. The grain size of the martensite is measured experimentally and considered as a constant here.

8.3 The Implementation of the Modeling Framework

Figure 40 is the flow chart showing the implementation of the present model. First, the experimental characterized microstructural parameters (i.e. grain size, volume fractions) and chemical compositions of individual phase are utilized as inputs, together with some material constants. The initial flow stress of each phase can then be calculated with equations 10-12, 20-21 and the initial macro flow stress can further be estimated by the stress rule of mixtures (i.e. equation 7).

To continue the simulation, an arbitrary incremental macro strain (e.g. 0.01%) is applied and the accumulated macro strain is recorded (bold in the Figure). Afterwards, the incremental macro strain (e.g. 0.01%) will be decomposed to calculate the strain for each phase according to the isowork condition (i.e. equation 8). Provided the incremental strain for each phase, the flow stresses of these phases can then be calculated using the Mecking-Kocks model (i.e. equations 9 and 17 for ferrite, bainite and untransformed austenite), Olson-Cohen model and Rodriguez model (i.e. equations 20 and 24 for strain-induced martensite and thermally induced martensite). After that, the macro flow stress can be evaluated by the flow stress of each phase through stress rule of mixtures. This value is recorded as the correspondent macro stress at the accumulated macro strain level (bold in the Figure). The same procedures are repeated to simulate the evolution of stress-strain behavior of the material.

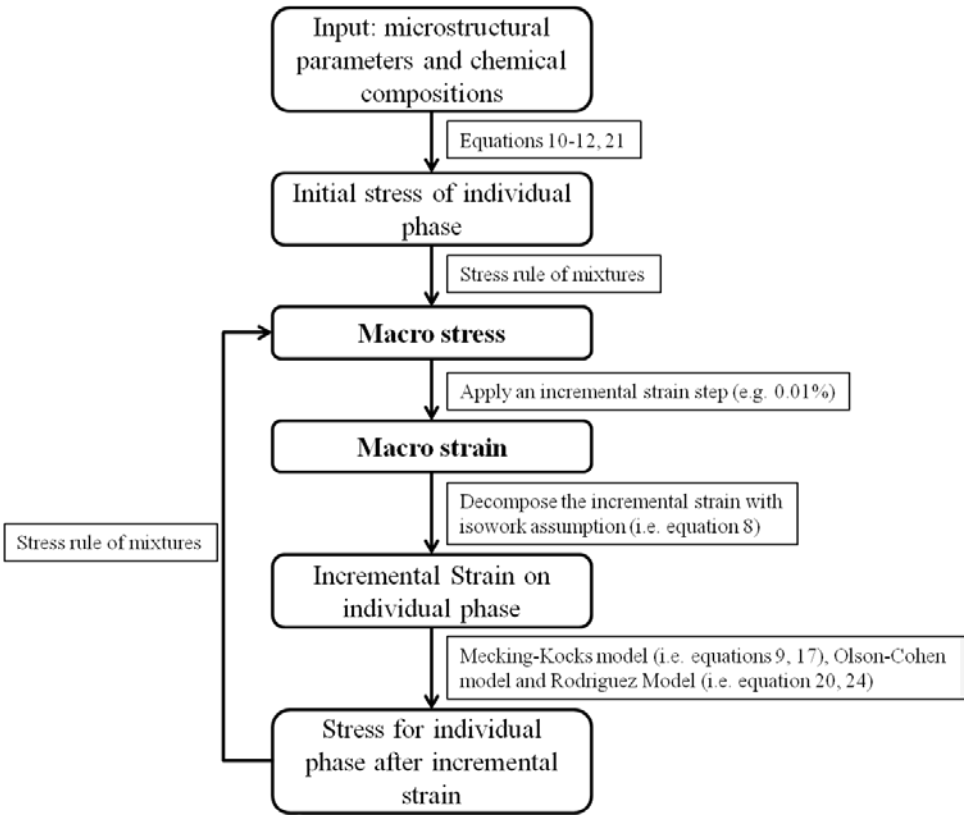

Figure 40. A schematic flow chart showing the implementation of present model framework

8.4 Result and Discussion

The model described in the previous section has been applied on TRIP-assisted steels with two different compositions. According to the experimental results in the previous chapters, one composition (Fe-2.65Mn-0.95Si-0.32C) can be make to reach as martensite free condition, while in the other one (Fe-1.42Mn-1.56Si-0.32C), we cannot avoid martensite. The material constants and fitting parameters in the model are listed in

Tables 10 and 11. To simplify the model, the Taylor factor is selected to be 3 for all phases assuming the texture is random or weak. The shear modulus for FCC phase is 72000 GPa and 78500 GPa for BCC phase, referring to [118]. The Burgers vectors are selected to be $2.48\times10^{-10}m^{-2}$ (α-Fe) for BCC phase and $2.48\times10^{-10}m^{-2}$ (γ-Fe) for FCC phase. The initial dislocation densities and α value of these phases are determined referring to [118, 176]. The constants for the Olson-Cohen model (β, θ in equation 24) are calculated using the relations in Table 9, based on the chemical composition of retained austenite which is experimentally determined. The k value (material constant in Hall-Patch relation) for ferrite and blocky austenite is selected to be 0.6 (pure Fe), while the k value for bainitic ferrite and thin film austenite is 115 referring to [173].

The fitting parameters (in Table 10) of ferrite, bainite and blocky austenite for both alloys in the present study are obtained by fitting one experimental result (i.e. the Fe-2.65Mn-0.95Si-0.32C after 700°C 10min-340°C 20min heat treatment). The microstructural inputs required in the model are listed in Table 12. The grain sizes of the phases are determined using SEM. The volume fractions are calculated by the same method as introduced in Chapter 3. Room temperature (i.e. 25°C) is assumed for the test. σ' in equation 10 for each phase is calculated based on the chemical composition of the phase. The carbon contents of ferrite and bainitic ferrite are assumed to be negligible while that in austenite and strain-induced martensite are assumed to be the same (assuming the transformation is diffusionless) and are measured using XRD. The Mn and Si contents for each phase are selected to be the same. No alloying partition is considered due to the relative short holding time during IA.

For the alloy in which thermally induced martensite cannot be fully suppressed, the fitting parameters of thermally induced martensite (in Table 10) are further obtained by fitting another experimental result of the Fe-1.42Mn-1.56Si-0.32C alloy after 772°C 2hr-340°C 15min heat treatment. The microstructural inputs for that case are obtained using the same method as mentioned before and listed in Table 13. Here, the thermally induced martensite is assumed to form before BIT heat treatment (i.e. quenching from IA temperature to BIT temperature), since the measured carbon content in retained austenite is in most scenario sufficient to stabilize austenite at room temperature according to the thermodynamic calculation. Thus, the carbon content of the thermally induced martensite should be the same as that in austenite after IA treatment, which can be calculated as following, considering the mass conservation of carbon:

$$C_{thermally\ induced\ martensite}(wt\%) = \frac{C_{total}(wt\%)}{V_{A'}} \quad (27)$$

where C_{total} is the carbon content measured in the as-receive material and $V_{A'}$ is the volume fraction of austenite after IA treatment. The carbon content in ferrite is again assumed to be negligible.

Table 10. Material constants and fitting parameters used in the present model

		Ferrite	Bainite		Bulky austenite		Thermally induced martensite
			Bainitic ferrite	Thin film austenite	Strain-induced Martensite	Austenite	
Material constants	Taylor Factor	3.00					
	Shear Modulus (GPa)	78500		72000	78500	72000	78500
	Burgers Vector (10^{-10}m)	2.48	2.48	2.58	2.48	2.58	2.48
	Initial dislocation density (m^{-2})	3×10^{12}	10^{13}	10^{12}		10^{12}	
	α	0.4					
	β	See to Table 11					
	θ	See to Table 11					
	k	0.6	115	115		0.6	
Fitting parameters	a	0.015	0.012	0	0	0	0
	h	12	10	0.01	0.01	0.01	3

Table 11. Calculated constants for the Olson-Cohen model

Chemical composition of alloy	Heat treatment		β	θ
	IA	BIT		
Fe-2.65Mn-0.95Si-0.32C	700°C 10min	340°C 20min	13.44	1.71
	700°C 30min	340°C 20min	13.85	1.72
Fe-1.42Mn-1.56Si-0.32C	772°C 2hr	340°C 15min	21.87	1.20
	780°C 2hr	340°C 15min	22.68	1.23
	810°C 2hr	340°C 15min	22.86	1.24

Table 12. Microstructural inputs for the model from the Fe-2.65Mn-0.95Si-0.32C alloy after 700°C 10min-340°C 20min heat treatment

700°C 10min 340°C 20min		Ferrite	Bainite		Bulky austenite	
			Bainitic ferrite	Thin film austenite	Strain-induced Martensite	Austenite
Grain size/lath size (μm)		3.50	0.60	0.30		1.40
Volume fractions		0.50	0.32	0.03	0	0.15
Testing temperature (°C)		25				
σ' (MPa)		179	179	608		608
Chemical composition (wt%)	C	0	0	1.19	1.19	1.19
	Mn	2.65				
	Si	0.95				

Table 13. Microstructural inputs for the model from Fe-1.42Mn-1.56Si-0.32C alloy after 772°C 2hr-340°C 15 min heat treatment

772°C 2hr 340°C 15min		Ferrite	Bainite		Bulky austenite		Thermal induced martensite
			Bainitic ferrite	Thin film austenite	Strain-induced Martensite	Austenite	
Grain size/lath size (μm)		8.00	0.42	0.20		3.00	3.00
Volume fractions		0.41	0.29	0.07	0	0.05	0.17
Testing temperature (°C)		25					
σ' (MPa)		179	179	595		595	
Chemical compositions (wt%)	C	0	0	1.12	1.12	1.12	0.54
	Mn	1.42					
	Si	1.56					

Figure 41 shows the comparisons between the experimental results (solid lines) and the model simulation (dashed lines) with fitting parameters for the two studied alloys. For the non-thermally induced martensite alloy (Fe-2.65Mn-0.95Si-0.32C), the simulation works perfectly to the yield stress and the early part of hardening (up to about 12%). The simulation deviates a little from the experimental results at higher strain level (>12%). One possible reason for the deviation is that the strain hardening due to the strain-induced martensitic transformation is not modeled very well. More specifically, the assumption of round strain-induced martensite (equation 23) might underestimate the size of martensite and thus the strength of them.

For the thermally induced martensite alloy (Fe-1.42Mn-1.56Si-0.32C), the shape of the experimental result can be well captured. The overall strength is overestimated by the simulation. The reason for that might come from the selection of Burgers vector (equation 9). In this study, same Burgers vectors are assumed for the two alloys to simplify the model, which could bring the offset observed here. In addition, it can also be seen that, at high strain level (>8%), the strain hardening rate deviates from the experimental results, similar as the in the previous case, which confirms the underestimation of strain hardening with the present model.

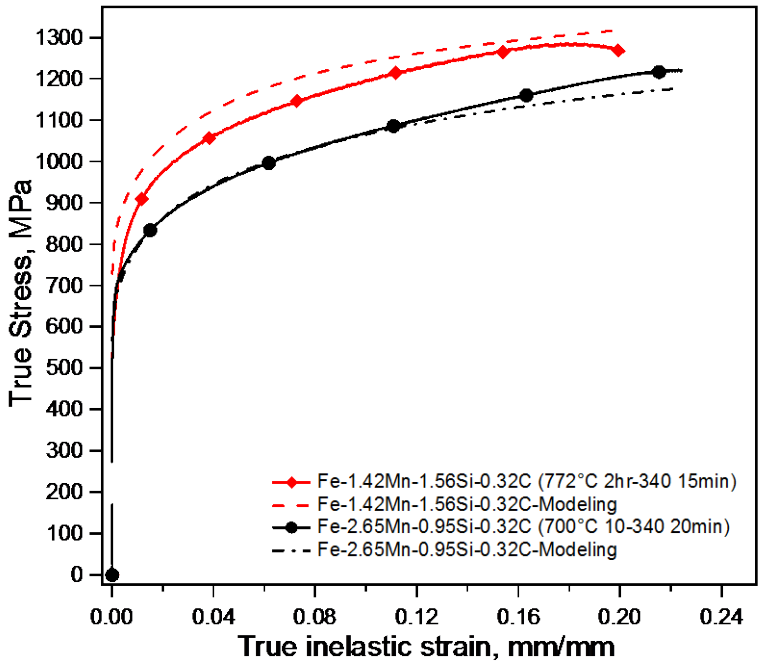

Figure 41. The experimental results (solid lines) and the model simulations (dashed lines) using the proposed microstructure model for the room temperature true stress-true inelastic strain response of Fe-1.42Mn-1.56Si-0.32C after 772°C 2hr-340°C 15min heat treatment and Fe-2.65Mn-0.95Si-0.32C after 700°C 10min-340°C 20min heat treatment

In order to examine the predictive capability of the present model, another microstructure is selected for the Fe-2.65Mn-0.95Si-0.32C alloy after 700°C 30min-340°C 20min, and two different microstructures are selected for the Fe-1.42Mn-1.56Si-0.32C alloy (i.e. after 780°C 2hr-340°C 15min and 810°C 2hr-340°C 15min). Same material constants and fitting parameters are applied (Table 10 and 11). The microstructural inputs are summarized in Table 14-16. The comparisons between experiments and modeling are shown in Figure 42 and 43.

For all the simulated conditions, the model provides reasonable predictions for both materials. This indicates that the current model is able to reasonably capture the effects of microstructural features (i.e. grain size, volume fractions of the phases and chemical compositions) on the macroscopic plastic behavior of the studied low alloy multiphase steels. The stress rule of mixtures and iso-work assumptions appear to work well on this 'composite' material. More importantly, the current model is able to predict the responses of various microstructures with the same sets of fitting parameters, which is rarely seen in the literature for modeling the same type of steels.

Table 14. Microstructural inputs for the model from Fe-2.65Mn-0.95Si-0.32C alloy after 700°C 30min-340°C 20 min heat treatment

700°C 30min-340°C 20 min		Ferrite	Bainite		Bulky austenite	
			Bainitic ferrite	Thin film austenite	Martensite	Austenite
Grain size/lath size (μm)		5.00	0.60	0.30		1.40
Volume fractions		0.50	0.32	0.03		0.15
Testing temperature (°C)		25				
σ'		179	179	665		665
Chemical compositions (wt%)	C	~0	~0	1.19	1.19	1.19
	Mn	2.65				
	Si	0.95				

Table 15. Microstructural inputs for the model from Fe-1.42Mn-1.56Si-0.32C alloy after 780°C 2hr-340°C 15 min heat treatment

780°C 2hr 340°C 15 min		Ferrite	Bainite		Bulky austenite		Thermal induced martensite
			Bainitic ferrite	Thin film austenite	Martensite	Austenite	
Grain size/lath size (μm)		6.00	0.42	0.20		2.10	2.10
Volume fractions		0.29	0.29	0.09		0.04	0.28
Testing temperature (°C)		25					
σ' (MPa)		179	179	705		705	
Chemical compositions (wt%)	C	0	0	1.43	1.43	1.43	0.45
	Mn	1.42					
	Si	1.56					

Table 16. Microstructural inputs for the model from Fe-1.42Mn-1.56Si-0.32C alloy after 810°C 2hr-340°C 15 min heat treatment

810°C 2hr 340°C min		Ferrite	Bainite		Bulky austenite		Thermal induced martensite
			Bainitic ferrite	Thin film austenite	Martensite	Austenite	
Grain size/lath size (μm)		2.70	0.42	0.20		1.50	1.50
Volume fractions		0.15	0.36	0.05		0.02	0.42
Testing temperature (°C)		25					
σ' (MPa)		179	179	730		730	
Chemical compositions (wt%)	C	0	0	1.5	1.5	1.5	0.38
	Mn	1.42					
	Si	1.56					

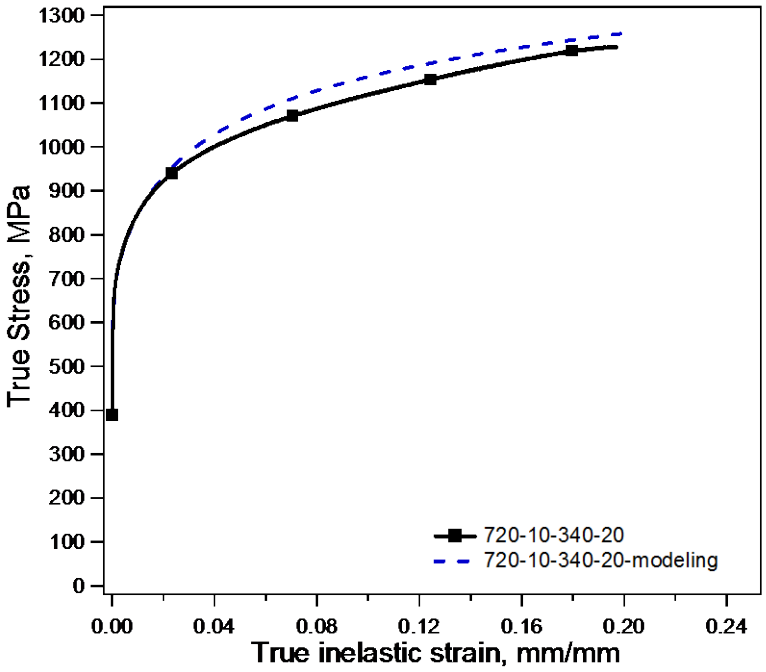

Figure 42. The experimental result (solid line) and the model simulation (dashed line) using the proposed microstructure model for the room temperature true stress-true inelastic strain response of Fe-2.65Mn-0.95Si-0.32C after 700°C 30min-340°C 20min heat treatment

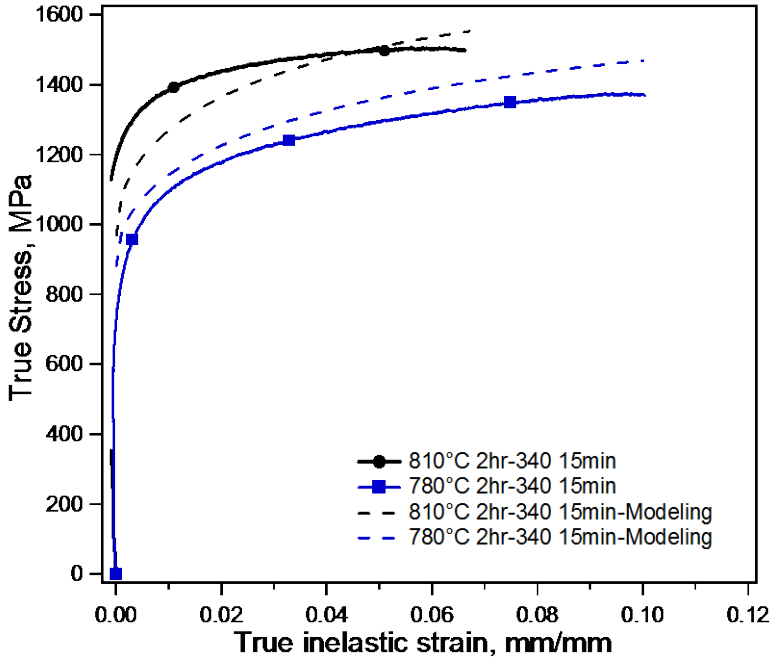

Figure 43. The experimental results (solid lines) and the model simulations (dashed lines) using the proposed microstructure model for the room temperature true stress-true inelastic strain response of Fe-1.42Mn-1.56Si-0.32C after 780°C 2hr-340°C 15min and 810°C 2hr-340°C 15min heat treatments

To further reveal the strain partitioning in each phase during plastic deformation, the simulated stress-strain behaviors of the individual phases and the mixture are presented in Figure 44 till the end of uniform deformation of the mixture for the alloy Fe-2.65Mn-0.95Si-0.32C after the heat treatment at 700°C for 10min+340°C for 20min. As expected, the ferrite is the softest phase and deforms more severe than the bainite and the blocky austenite when the mixture starts to neck at 22% strain. The strain hardening of the multiphase steel appears to be the result of blocky austenite due to the strain-induced martensitic transformation. It can be noticed that two inflection points are

present for the blocky austenite curve, as marked in the Figure. According to the Olson-Cohen model (equation 24), the correspondent strain levels (about 0.4% and 8%, respectively) of the two points could be interpreted as the initiation and termination of the strain-induced martensitic transformation.

The strain partitioning of the individual phases shown in Figure 44 can also provide another view on evaluating the ductility of the multiphase TRIP-assisted steels. As mentioned before, the ferrite is the softest phase and deforms the most among the three phases in the microstructure, which, on the other hand, also means that the plastic instability probably starts first in ferrite. Figure 45 validates this argument. The plastic instability criterion (i.e. $d\sigma/d\varepsilon=\sigma$) is first fulfilled in the ferrite (indicated by arrow in the Figure). Bainite almost fulfills the instability criterion when the mixture starts necking, whereas the blocky austenite is still away from fulfilling the criterion. These results indicate that ferrite is the phase which limits the further improvement of ductility.

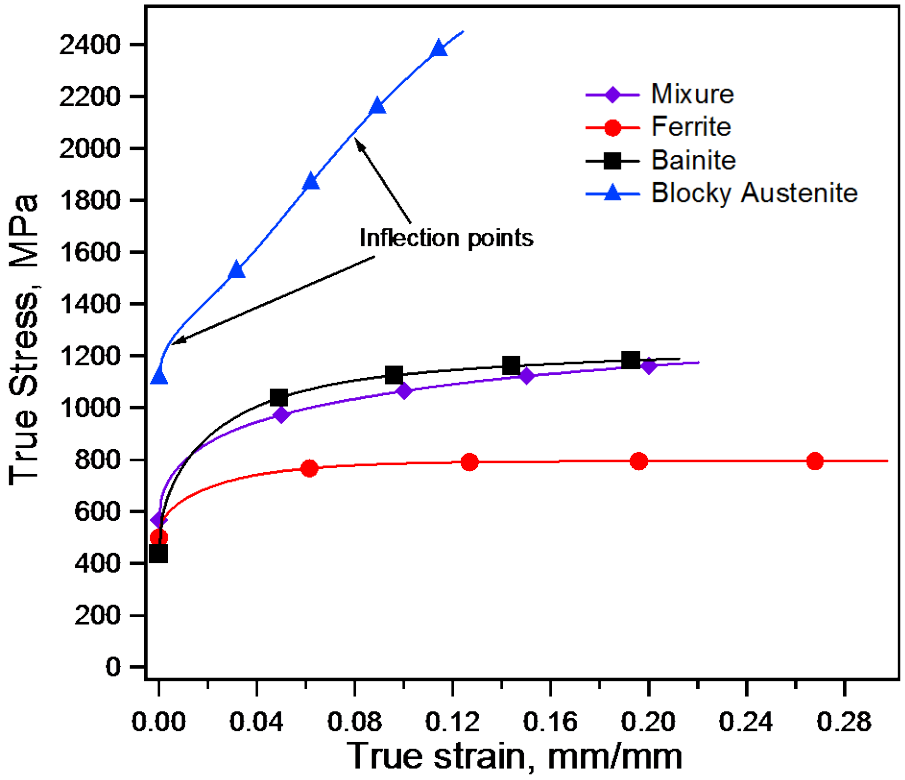

Figure 44. The simulated stress-strain behavior of the individual phases and the mixture (till the end of the uniform deformation regime) for Fe-2.65Mn-0.95Si-0.32C after the heat treatment at 700°C for 10min+340°C for 20min. The experimental results for this particular case is shown in Figure 41

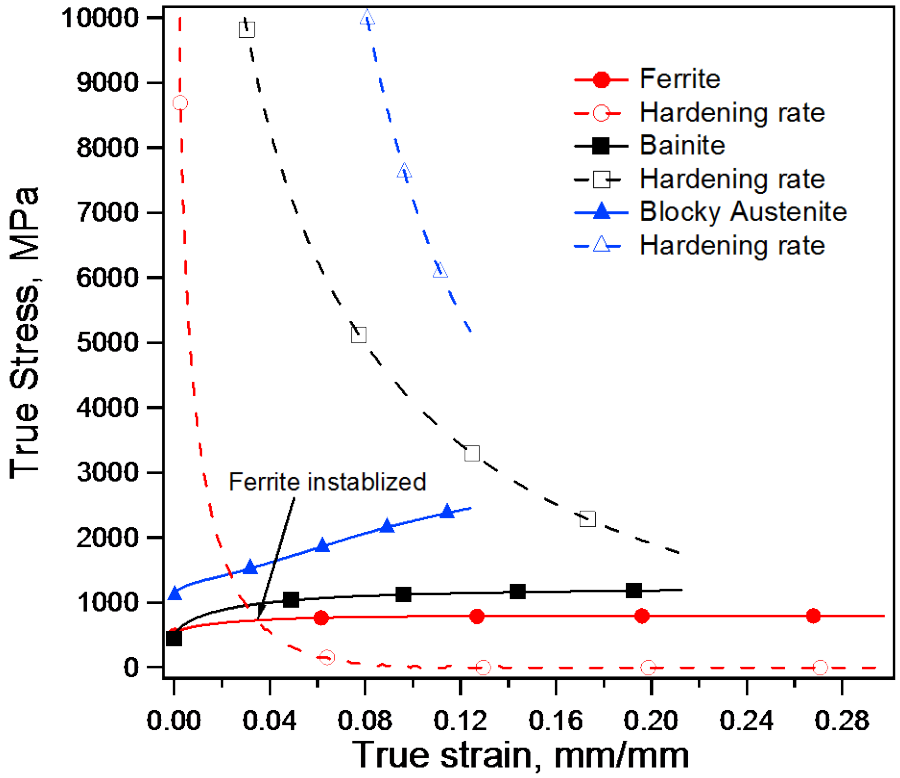

Figure 45. Simulated stress-strain behavior (solid curves) and hardening rate (dashed curves) of the individual phases (till the end of experimentally determined uniform deformation) for Fe-2.65Mn-0.95Si-0.32C after the heat treatment at 700°C for 10min+340°C for 20min

The present model, as shown previously, could effectively capture the relation between microstructure and mechanical response. For the next step, some microstructure inputs in the model, such as the volume fractions of the individual phases and the carbon content in retained austenite, would be predicted using the thermodynamic and kinetic models by our previous work [136]. By doing this, it is one step closer to reveal and capture the general relations among thermo-processing, microstructure and mechanical

property of the multiphase TRIP-assisted steels. Through a multi-objective optimization approach/model, it would be then feasible to know the phase fractions, or even the required heat treatment, for a specific stress-strain response providing the chemical composition of the alloy without experiments, or vice versa.

CHAPTER IX

CONCLUSIONS AND FUTURE WORK

In this dissertation, the structure-property relation of the multiphase low alloy steels has been characterized and optimized on two model compositions. The effects of phase constitution on the strength and ductility have been revealed. Following that, hypothesis of maximizing ferrite and retained austenite have been proposed to optimize the strength and ductility. Two different methods have been successfully utilized to further modify the microstructure in order to better fit the hypothesis: heat treatment modification and alloying addition. Finally, a microstructure-based model has been established to simulate the flow stress-strain evolution of the multiphase materials. According to the results so far, the major conclusions could be summarized as follows:

1. Martensite is the main phase which deteriorates the uniform strain regardless of other phases, which needs to be minimized or eliminated if ductility needs to be optimized.
2. As a simplified parameter, the C/V_A ratio of retained austenite is shown to be a better indicator of the uniform strain rather than carbon content or the volume fraction. A high C/V_A ratio indicates a poor uniform strain. However, the trend between the C/V_A ratio and uniform strain is a second order one when martensite exists in the microstructure and not as strong as that of martensite volume fraction.
3. The C/V_A ratio is also a good indicator of toughness. A small C/V_A ratio can lead to a combination of high strength and high ductility.

4. Although no definite conclusion could be drawn on whether ferrite or retained austenite is more beneficial for achieving high uniform strain, it is suggested that, replacing martensite with ferrite would be a more easy choice for better ductility, since the volume fraction of ferrite can be directly controlled by IA conditions.
5. A systematic microstructural design strategy has been proposed, carried out, and validated on a model low carbon, low-alloy TRIP-assisted steel through a computational and experimental methodology. Computational thermodynamics calculations have been utilized to determine the two-stage heat treatment conditions based on the proposed criteria of first maximizing ferrite and then retained austenite volume fractions. A remarkable improvement of about 500 MPa has been achieved accompanied with about 10% extra hardening as compared to the ferritic-pearlitic condition. The maximum true stress reached was about 1300 MPa with a uniform strain of around 22%.
6. A dual BIT heat treatment has been proposed and studied on a low carbon, low alloy TRIP-assisted steel. Martensite can be effectively suppressed, which provides more freedom for phase constitutional design.
7. Martensite formation can also be suppressed by alloying addition with Mn content. The martensite-free microstructure shows consistently better ductility than the martensite contained low alloy studied earlier.
8. The proposed microstructure based semi-empirical model can effectively predict the flow stress-strain behavior of various microstructures of two compositions without changing fitting parameters.

9. According to the microstructure-based model, ferrite is softest phase and also one of the limitations for the further improvement of ductility.

The future work will include the following:

1. Apply the C/V_A ratio, and the proposed design criterion to other low alloy TRIP-assisted steel to check the applicability.
2. Realizing the limitation for further improvement of ductility on the multiphase alloy, strengthening ferrite will be attempted to retard the occurrence of plastic instability of the material. Mechanical processing (e.g. ECAP, rolling) or alloy addition will be considered for the purpose.
3. Implant the thermodynamic and kinetic model to predict the volume fractions of the individual phases and the carbon content of the retained austenite, and combine the model with the present one, such that a rough computational mapping between thermo-processing, microstructure and mechanical response could be established.

REFERENCES

[1] Future Vehicle Steel report, 2012. URL: http://www.worldautosteel.org/projects/future-steel-vehicle/phase-2-results/.

[2] H.N. Han, C.S. Oh, G. Kim, O. Kwon, Mat Sci Eng A, 499 (2009) 462-468.

[3] V.F. Zackay, E.R. Parker, D. Fahr, R. Busch, ASM Trans Q, 60 (1967) 252.

[4] O. Matsumura, Y. Sakuma, H. Takechi, Scripta Metall, 21 (1987) 1301-1306.

[5] O. Matsumura, Y. Sakuma, H. Takechi, T Iron Steel I JPN, 27 (1987) 570-579.

[6] G.B. Olson, M. Cohen, J. Less-Common Met, 28 (1972) 107-118.

[7] G.B. Olson, M. Cohen, Metall Trans A, 6 (1975) 791-795.

[8] G.B. Olson, M. Cohen, Metall Trans A, 7 (1976) 1897-1904.

[9] H. Bhadeshia, Bainite in Steels, Second ed., Cambridge University Press, London, 2001.

[10] H. Bhadeshia, D.V. Edmonds, Acta Metall, 28 (1980) 1265-1273.

[11] J. Speer, D.K. Matlock, B.C. De Cooman, J.G. Schroth, Acta Mater, 51 (2003) 2611-2622.

[12] A.J. Clarke, J.G. Speer, M.K. Miller, R.E. Hackenberg, D.V. Edmonds, D.K. Matlock, F.C. Rizzo, K.D. Clarke, E. De Moor, Acta Mater, 56 (2008) 16-22.

[13] D.V. Edmonds, K. He, F.C. Rizzo, B.C. De Cooman, D.K. Matlock, J.G. Speer, Mat Sci Eng A, 438 (2006) 25-34.

[14] G.R. Speich, V.A. Demarest, R.L. Miller, Metall Trans A, 12 (1981) 1419-1428.

[15] J. Huang, W.J. Poole, M. Militzer, Metall Mater Trans A, 35A (2004) 3363-3375.

[16] X.D. Wang, B.X. Huang, Y.H. Rong, L. Wang, Mat Sci Eng A, 438 (2006) 300-305.

[17] X.D. Wang, B.X. Huang, L. Wang, Y.H. Rong, Metall Mater Trans A, 39A (2008) 1-7.

[18] V. Sista, P. Nash, S.S. Sahay, J Mater Sci, 42 (2007) 9112-9115.

[19] H. Bhadeshia, P Roy Soc A-Math Phy, 466 (2010) 3-18.

[20] X.D. Wang, N. Zhong, Y.H. Rong, T.Y. Hsu, L. Wang, J Mater Res, 24 (2009) 260-267.

[21] K. Zhang, M.H. Zhang, Z.H. Guo, N.L. Chen, Y.H. Rong, Mat Sci Eng A, 528 (2011) 8486-8491.

[22] N. Zhong, X.D. Wang, L. Wang, Y.H. Rong, Mat Sci Eng A, 506 (2009) 111-116.

[23] F. Hajiakbari, M. Nili-Ahmadabadi, B. Poorganji, T. Furuhara, Acta Mater, 58 (2010) 3073-3078.

[24] J.J. Wang, S. van der Zwaag, Metall Mater Trans A, 32 (2001) 1527-1539.

[25] C. Garcia-Mateo, F.G. Caballero, J. Chao, C. Capdevila, C.G. de Andres, J Mater Sci, 44 (2009) 4617-4624.

[26] S. Chatterjee, H.S. Wang, J.R. Yang, H. Bhadeshia, Mater Sci Tech Ser, 22 (2006) 641-644.

[27] A.S. Podder, H. Bhadeshia, Mat Sci Eng A, 527 (2010) 2121-2128.

[28] N.H. van Dijk, A.M. Butt, L. Zhao, J. Sietsma, S.E. Offerman, J.P. Wright, S. van der Zwaag, Acta Mater, 53 (2005) 5439-5447.

[29] S.J. Lee, S. Lee, B.C. De Cooman, Scripta Mater, 64 (2011) 649-652.

[30] K.W. Andrews, J Iron Steel I, 203 (1965) 721-727.

[31] C.Y. Kung, J.J. Rayment, Metall Trans A, 13 (1982) 328-331.

[32] J.J. Wang, P.J. van der Wolk, S. van der Zwaag, Mater T JIM, 41 (2000) 761-768.

[33] S. van der Zwaag, L. Zhao, S.O. Kruijver, J. Sietsma, ISIJ Int, 42 (2002) 1565-1570.

[34] M. Olasolo, P. Uranga, J.M. Rodriguez-Ibabe, B. Lopez, Mat Sci Eng A, 528 (2011) 2559-2569.

[35] D.W. Suh, S.J. Park, C.S. Oh, S.J. Kim, Scripta Mater, 57 (2007) 1097-1100.

[36] D.W. Suh, S.J. Park, H.N. Han, S.J. Kim, Metall Mater Trans A, 41A (2010) 3276-3281.

[37] Y. Sakuma, D.K. Matlock, G. Krauss, Metall Trans A, 23 (1992) 1221-1232.

[38] W. Shi, L. Li, C.X. Yang, R.Y. Fu, L. Wang, P. Wollants, Mat Sci Eng A, 429 (2006) 247-251.

[39] Y. Mi, Scripta Metall Mater, 32 (1995) 1313-1317.

[40] H.C. Chen, H. Era, M. Shimizu, Metall Trans A, 20 (1989) 437-445.

[41] E. Jimenez-Melero, N.H. van Dijk, L. Zhao, J. Sietsma, S.E. Offerman, J.P. Wright, S. van der Zwaag, Scripta Mater, 56 (2007) 421-424.

[42] E. Jimenez-Melero, N.H. van Dijk, L. Zhao, J. Sietsma, S.E. Offerman, J.P. Wright, S. van der Zwaag, Acta Mater, 55 (2007) 6713-6723.

[43] D.P. Koistinen, R.E. Marburger, Acta Metall, 7 (1959) 59-60.

[44] K. Tsuzaki, S. Fukasaku, Y. Tomota, T. Maki, Mater T JIM, 32 (1991) 222-228.

[45] P. Jacques, Q. Furnemont, A. Mertens, F. Delannay, Philos Mag A, 81 (2001) 1789-1812.

[46] K. Hase, C. Garcia-Mateo, H. Bhadeshia, Mat Sci Eng A, 438 (2006) 145-148.

[47] P.J. Jacques, E. Girault, A. Mertens, B. Verlinden, J. van Humbeeck, F. Delannay, ISIJ Int, 41 (2001) 1068-1074.

[48] H.K.D.H. Bhadeshia, D.V. Edmonds, Metall Trans A, 10 (1979) 895-907.

[49] C. Garcia-Mateo, F.G. Caballero, Mater Trans, 46 (2005) 1839-1846.

[50] H.L. Yi, K.Y. Lee, H. Bhadeshia, Mat Sci Eng A, 528 (2011) 5900-5903.

[51] S. Lee, K. Lee, B.C. De Cooman, Ultra Fine-grained 6wt% Manganese TRIP Steel, in: J.F. Nie, A. Morton (Eds.) Pricm 7, Pts 1-3, Trans Tech Publications Ltd, Stafa-Zurich, 2010, pp. 286-289.

[52] T. Heller, A. Nuss, Ironmak Steelmak, 32 (2005) 303-308.

[53] P.J. Jacques, Q. Furnemont, F. Lani, T. Pardoen, F. Delannay, Acta Mater, 55 (2007) 3681-3693.

[54] H.L. Yi, K.Y. Lee, H.K.D.H. Bhadeshia, P Roy Soc A-Math Phy, 467 (2011) 234-243.

[55] J. Shi, X.J. Sun, M.Q. Wang, W.J. Hui, H. Dong, W.Q. Cao, Scripta Mater, 63 (2010) 815-818.

[56] D.L. Liu, J.A. Zhang, Z.Y. Li, Processing, Properties and Microstructure of a 1.2%Al TRIP Steel, in: J.F. Nie, A. Morton (Eds.) Pricm 7, Pts 1-3, Trans Tech Publications Ltd, Stafa-Zurich, 2010, pp. 282-285.

[57] O. Matsumura, Y. Sakuma, H. Takechi, Tetsu To Hagane, 77 (1991) 1304-1311.

[58] E. Emadoddin, A. Akbarzadeh, G. Daneshi, Mater Charact, 57 (2006) 408-413.

[59] E. Emadoddin, A. Akbarzadeh, G. Daneshi, J Mater Process Tech, 203 (2008) 293-300.

[60] E. Emadoddin, A. Akbarzadeh, R. Petrov, L. Kestens, H. Pirgazi, J Appl Crystallogr, 44 (2011) 1190-1197.

[61] I.B. Timokhina, P.D. Hodgson, E.V. Pereloma, Metall Mater Trans A, 35A (2004) 2331-2341.

[62] E.V. Pereloma, I.B. Timokhina, K.F. Russell, M.K. Miller, Scripta Mater, 54 (2006) 471-476.

[63] G. Haidemenopoulos, K. Papadimitriou, Steel Res, 66 (1995) 433-438.

[64] P. Jacques, X. Cornet, P. Harlet, J. Ladriere, F. Delannay, Metall Mater Trans A, 29 (1998) 2383-2393.

[65] H.K.D.H. Bhadeshia, D.V. Edmonds, Acta Metall, 28 (1980) 1265-1273.

[66] D.V. Edmonds, R.C. Cochrane, Metall Trans A, 21 (1990) 1527-1540.

[67] G. Ghosh, G.B. Olson, Acta Metall. Mater., 42 (1994) 3361-3370.

[68] H.B. Chang, T. Zuyao, Acta Metall, 34 (1986) 333-338.

[69] F.G. Caballero, M.J. Santofimia, C. Garcia-Mateo, C.G. de Andres, Mater Trans, 45 (2004) 3272-3281.

[70] Z.B. Zhao, C. Liu, Y.X. Liu, D.O. Northwood, J Mater Sci, 36 (2001) 5045-5056.

[71] L.C. Chang, Metall Mater Trans A, 30 (1999) 909-916.

[72] E.S. Rowland, S.R. Lyle, T Am Soc Metal, 37 (1946) 27-47.

[73] R.A. Grange, H.M. Stewart, T Am I Min Met Eng, 167 (1946) 467-501.

[74] M. De Meyer, J. Mahieu, B.C. De Cooman, Mater Sci Tech Ser, 18 (2002) 1121-1132.

[75] M. Kundu, S. Ganguly, S. Datta, P.P. Chattopadhyay, Mater Manuf Process, 24 (2009) 169-173.

[76] T. Iung, M. Azuma, O. Bouaziz, M. Goune, A. Perlade, D. Quidort, A model for the prediction of microstructure and mechanical properties in cold rolled and annealed TRIP steels, in: T. Chandra, J.M. Torralba, T. Sakai (Eds.) Thermec'2003, Trans Tech Publications Ltd, Zurich-Uetikon, 2003, pp. 3849-3854.

[77] K. Asoo, Y. Tomota, S. Harjo, Y. Okitsu, ISIJ Int, 51 (2011) 145-150.

[78] R.Z. Valiev, T.G. Langdon, Prog Mater Sci, 51 (2006) 881-981.

[79] M. Haouaoui, K.T. Hartwig, E.A. Payzant, Acta Mater, 53 (2005) 801-810.

[80] I. Karaman, G. Yapici, Y. Chumlyakov, I. Kireeva, Materials Science and Engineering: A, 410 (2005) 243-247.

[81] B. Kockar, I. Karaman, J. Kim, Y. Chumlyakov, J. Sharp, C.J.M. Yu, Acta Mater, 56 (2008) 3630-3646.

[82] S. Ferrasse, V.M. Segal, F. Alford, Mat Sci Eng A, 372 (2004) 235-244.

[83] M. Haouaoui, I. Karaman, H. Maier, Acta Mater, 54 (2006) 5477-5488.

[84] S.Y. Li, A.A. Gazder, I.J. Beyerlein, E.V. Pereloma, C.H.J. Davies, Acta Mater, 54 (2006) 1087-1100.

[85] G.G. Yapici, I. Karaman, Z.P. Luo, Acta Mater, 54 (2006) 3755-3771.

[86] I. Karaman, A. Kulkarni, Z. Luo, Philos Mag, 85 (2005) 1729-1745.

[87] G. Purcek, I. Karaman, G.G. Yapici, M. Al-Maharbi, T. Kucukomeroglu, O. Saray, Int J Mater Res, 98 (2007) 332-338.

[88] N. Gao, M.J. Starink, M. Furukawa, Z. Horita, C. Xu, T.G. Langdon, Evolution of microstructure and precipitation in heat-treatable aluminium alloys during ECA pressing and subsequent heat treatment, in: Z. Horita (Ed.) Nanomaterials by Severe Plastic Deformation, Trans Tech Publications Ltd, Zurich-Uetikon, 2006, pp. 275-280.

[89] S.N. Mathaudhu, K.T. Hartwig, I. Karaman, J. Non-Cryst. Solids, 353 (2007) 185-193.

[90] C. Xu, Z.J. Horita, M. Furukawa, T.G. Langdon, J Mater Eng Perform, 13 (2004) 683-690.

[91] C. Xu, M. Furukawa, Z. Horita, T.G. Langdon, Acta Mater, 53 (2005) 749-758.

[92] G. Yapici, I. Karaman, Z. Luo, H. Rack, Scripta Mater, 49 (2003) 1021-1027.

[93] T. Niendorf, D. Canadinc, H.J. Maier, I. Karaman, S.G. Sutter, Int J Mater Res, 97 (2006) 1328-1336.

[94] O. Saray, G. Purcek, I. Karaman, T. Neindorf, H.J. Maier, Mat Sci Eng A, 528 (2011) 6573-6583.

[95] G.G. Yapici, I. Karaman, Z.P. Luo, Y. Chumlyakov, in: Y.T. Zhu, T.G. Langdon, R.Z. Valiev, S.L. Semiatin, D.H. Shin, T.C. Lowe (Eds.) Third International Symposium of Ultrafine Grained Materials, TMS Publications, Charlotte, NC, 2004, pp. 291-296.

[96] G. Purcek, O. Saray, I. Karaman, H.J. Maier, Metall Mater Trans A, 43A (2012) 1884-1894.

[97] N. Saito, M. Mabuchi, M. Nakanishi, I. Shigematsu, G. Yamauchi, M. Nakamura, J Mater Sci, 36 (2001) 3229-3232.

[98] Y. Fukuda, K. Oh-ishi, Z. Horita, T.G. Langdon, Acta Mater, 50 (2002) 1359-1368.

[99] D.H. Shin, B.C. Kim, Y.S. Kim, K.T. Park, Acta Mater, 48 (2000) 2247-2255.

[100] D.H. Shin, B.C. Kim, K.T. Park, W.Y. Choo, Acta Mater, 48 (2000) 3245-3252.

[101] D.H. Shin, I. Kim, J. Kim, K.T. Park, Acta Mater, 49 (2001) 1285-1292.

[102] K.T. Park, Y.K. Lee, D.H. Shin, ISIJ Int, 45 (2005) 750-755.

[103] T. Niendorf, D. Canadinc, H.J. Maier, I. Karaman, Metall Mater Trans A, 38A (2007) 1946-1955.

[104] T. Niendorf, D. Canadinc, H. Maier, I. Karaman, Int J Fatigue, 30 (2008) 426-436.

[105] T. Niendorf, H.J. Maier, D. Canadinc, I. Karaman, Key Eng Mat, 378 (2008) 39-52.

[106] T. Niendorf, D. Canadinc, H. Maier, I. Karaman, Metall Trans A, 38 (2007) 1946-1955.

[107] T.S. Wang, Z. Li, B. Zhang, X.J. Zhang, J.M. Deng, F.C. Zhang, Mat Sci Eng A, 527 2798-2801.

[108] H. Azizi-Alizamini, M. Militzer, W.J. Poole, Scripta Mater, 57 (2007) 1065-1068.

[109] G. Yapici, I. Karaman, Z. Luo, H. Maier, Y. Chumlyakov, J Mater Res, 19 (2004) 2268-2278.

[110] D.H. Shin, J.J. Park, S.Y. Chang, Y.K. Lee, K.T. Park, ISIJ Int, 42 (2002) 1490-1496.

[111] Y.I. Son, Y.K. Lee, K.T. Park, C.S. Lee, D.H. Shin, Acta Mater, 53 (2005) 3125-3134.

[112] F.M. Al-Abbasi, J.A. Nemes, Int J Mech Sci, 45 (2003) 1449-1465.

[113] M. Delince, Y. Brechet, J.D. Embury, M.G.D. Geers, P.J. Jacques, T. Pardoen, Acta Mater, 55 (2007) 2337-2350.

[114] T. Huper, S. Endo, N. Ishikawa, K. Osawa, ISIJ Int, 39 (1999) 288-294.

[115] M.H. Poech, Scripta Metall Mater, 27 (1992) 1027-1031.

[116] H.N. Han, C.G. Lee, C.S. Oh, T.H. Lee, S.J. Kim, Acta Mater, 52 (2004) 5203-5214.

[117] A. Perlade, O. Bouaziz, Q. Furnemont, Mat Sci Eng A, 356 (2003) 145-152.

[118] J. Bouquerel, K. Verbeken, B.C. de Cooman, Acta Mater, 54 (2006) 1443-1456.

[119] F. Roters, P. Eisenlohr, L. Hantcherli, D.D. Tjahjanto, T.R. Bieler, D. Raabe, Acta Mater, 58 (2010) 1152-1211.

[120] K.S. Choi, W.N. Liu, X. Sun, M.A. Khaleel, Acta Mater, 57 (2009) 2592-2604.

[121] R.G. Stringfellow, D.M. Parks, G.B. Olson, Acta Metall. Mater., 40 (1992) 1703-1716.

[122] L. Samek, E. De Moor, J. Penning, B.C. De Cooman, Metall Mater Trans A, 37A (2006) 109-124.

[123] M. Onyuna, H. Oettel, U. Martin, A. Weiss, Advanced Engineering Materials, 6 (2004) 529-535.

[124] N.C. Goel, S. Sangal, K. Tangri, Metall Trans A, 16 (1985) 2013-2021.

[125] H. Mecking, U. Kocks, Acta Metall, 29 (1981) 1865-1875.

[126] Y. Estrin, H. Mecking, Acta Metall, 32 (1984) 57-70.

[127] B.C. De Cooman, Curr Opin Soild St M, 8 (2004) 285-303.

[128] R. Kuziak, R. Kawalla, S. Waengler, Arch Civ Mech Eng, 8 (2008) 103-117.

[129] J. Kliber, G. Plestilova, O. Zacek, M. Soman, Effects of thermomechanical processing on microstructure and mechanical properties multiphase steels exhibiting a TRIP effect, in: T. Chandra, K. Tsuzaki, M. Militzer, C. Ravindran (Eds.) Thermec' 2006, Pts 1-5, Trans Tech Publications Ltd, Zurich-Uetikon, 2007, pp. 4357-4362.

[130] R.G. Davies, Metall Trans A, 9 (1978) 671-679.

[131] I. Tsukatani, S. Hashimoto, T. Inoue, ISIJ Int, 31 (1991) 992-1000.

[132] E. Girault, P. Jacques, P. Harlet, K. Mols, J. Van Humbeeck, E. Aernoudt, F. Delannay, Mater Charact, 40 (1998) 111-118.

[133] A. Takacs-Szabo, B. Vero, J. Solyom, Metallographic investigation of TRIP steels, in: J. Gyulai, P.J. Szabo (Eds.) Materials Science, Testing and Informatics III, Trans Tech Publications Ltd, Zurich-Uetikon, 2007, pp. 457-463.

[134] C.F. Jatczak, J.A. Larson, S.W. Shin, Retained Austenite and Its Measurements by X-Ray Diffraction, Society of Automotive Engineers, Inc, Warrendale, PA, 1980.

[135] P.J. Jacques, S. Allain, O. Bouaziz, A. De, A.F. Gourgues, B.M. Hance, Y. Houbaert, J. Huang, A. Iza-Mendia, S.E. Kruger, M. Radu, L. Samek, J. Speer, L. Zhao, S. van der Zwaag, Mater Sci Tech Ser, 25 (2009) 567-574.

[136] H. Bhadeshia, D.V. Edmonds, Metall Trans A, 10 (1979) 895-907.

[137] R. Zhu, S. Li, I. Karaman, R. Arroyave, T. Niendorf, H.J. Maier, Acta Mater, 60 (2012) 3022-3033.

[138] M. Sarwar, R. Priestner, J Mater Sci, 31 (1996) 2091-2095.

[139] K. Sugimoto, N. Usui, M. Kobayashi, S. Hashimoto, ISIJ Int, 32 (1992) 1311-1318.

[140] A.I. Katsamas, A.N. Vasilakos, G.N. Haidemenopoulos, Steel Res, 71 (2000) 351-356.

[141] X.L. Cai, A.J. Garrattreed, W.S. Owen, Metall Trans A, 16 (1985) 543-557.

[142] H.K.D.H. Bhadeshia, Met Sci, 15 (1981) 175-177.

[143] S. Chatterjee, H.K.D.H. Bhadeshia, Mater Sci Tech Ser, 23 (2007) 1101-1104.

[144] C. Garcia-Mateo, H.K.D.H. Bhadeshia, Mat Sci Eng A, 378 (2004) 289-292.

[145] D. Quidort, Y. Brechet, ISIJ Int, 42 (2002) 1010-1017.

[146] H.K.D.H. Bhadeshia, Met Sci, 16 (1982) 159-165.

[147] D. Quidort, Y. Brechet, Scripta Mater, 47 (2002) 151-156.

[148] D. Quidort, Y. Brechet, Acta Mater, 49 (2001) 4161-4170.

[149] H. Matsuda, H.K.D.H. Bhadeshia, P Roy Soc Lond A Mat, 460 (2004) 1707-1722.

[150] C.C. Tasan, J.P.M. Hoefnagels, M.G.D. Geers, Scripta Mater, 62 835-838.

[151] A. Marder, Metall Trans A, 13 (1982) 85-92.

[152] X. L. Cai, J. Feng, W. Owen, Metall Mater Trans A, 16 (1985) 1405-1415.

[153] W. Xu, D. Rivera, Iacute, P.E.J. Az-Del-Castillo, S. van der Zwaag, ISIJ Int, 45 (2005) 380-387.

[154] G. Papadimitriou, G. Fourlaris, J. Phys. IV France, 07 (1997) C5-131-C135-136.

[155] R. Zhu, S. Li, M. Song, I. Karaman, R. Arroyave, Mat Sci Eng A, in press (2012).

[156] H. Bhadeshia, Met Sci, 15 (1981) 175-177.

[157] H. Bhadeshia, Met Sci, 16 (1982) 159-165.

[158] J. Chen, H. Bhadeshia, S. Hasler, H. Roelofs, U. Ulrau, Complete Calculation of Steel Microstructure for Strong Alloys, in: NEW DEVELOPMENTS ON METALLURGY AND APPLICATIONS OF HIGH STRENGTH STEELS: BUENOS AIRES 2008, VOLS 1 AND 2, 2008, pp. 749-759.

[159] H.Bhadeshia., R.W.K. Honeycombe, Steels: Microstructure and Properties, Third ed., Elsevier Ltd, 2006.

[160] M.I. Khan, M.L. Kuntz, Y. Zhou, Sci Technol Weld Joi, 13 (2008) 294-304.

[161] H.W. Luo, L. Zhao, S.O. Kruijver, J. Sietsma, S. van der Zwaag, ISIJ Int, 43 (2003) 1219-1227.

[162] S. Suzuki, K. Abiko, H. Kimura, Scripta Metall, 15 (1981) 1139-1143.

[163] H.J. Grabke, R. Moller, H. Erhart, S.S. Brenner, Surface and Interface Analysis, 10 (1987) 202-209.

[164] T. Bhattacharyya, S.B. Singh, S. Das, A. Haldar, D. Bhattacharjee, Mat Sci Eng A, 528 (2011) 2394-2400.

[165] J. Shi, X.J. Sun, M.Q. Wang, W.J. Hui, H. Dong, W.Q. Cao, Scripta Mater, 63 (2009) 815-818.

[166] S. Lee, S.J. Lee, B.C. De Cooman, Acta Mater, 59 (2011) 7546-7553.

[167] E. De Moor, J.G. Speer, D.K. Matlock, J.H. Kwak, S.B. Lee, Steel Res Int, 83 (2012) 322-327.

[168] P.J. Gibbs, E. De Moor, M.J. Merwin, B. Clausen, J.G. Speer, D.K. Matlock, Metall Mater Trans A, 42A (2011) 3691-3702.

[169] Marc Myers, K. Chawla, Mechanical Behavior of Materials, Second ed., Cambridge University Press, 2008.

[170] R. Rodriguez, I. Gutierrez, Unified formulation to predict the tensile curves of steels with different microstructures, in: T. Chandra, J.M. Torralba, T. Sakai (Eds.) Thermec'2003, Pts 1-5, Trans Tech Publications Ltd, Zurich-Uetikon, 2003, pp. 4525-4530.

[171] S.B. Singh, H. Bhadeshia, Mat Sci Eng A, 245 (1998) 72-79.

[172] F.B. Prinz, A.S. Argon, Acta Metall, 32 (1984) 1021-1028.

[173] C.H. Young, H. Bhadeshia, Mater Sci Tech Ser, 10 (1994) 209-214.

[174] T. Gladman, I.D. McIvor, Pickerin.Fb, J Iron Steel I, 210 (1972) 916-&.

[175] G. Krauss, Mat Sci Eng A, 273 (1999) 40-57.

[176] A. Yoshie, T. Fujita, M. Fujioka, K. Okamoto, H. Morikawa, H. Mabuchi, ISIJ Int, 36 (1996) 444-450.